Chemical Science

Accepted Manuscript

This article can be cited before page numbers have been issued, to do this please use: S. Park, J. B. Park, J. M. Ha, H. S. S. Kim, M. H. Song and H. Y. Woo, *Chem. Sci.*, 2026, DOI: 10.1039/D5SC10164F.

ROYAL SOCIETY OF CHEMISTRY

rsc.li/chemical-science

View Article Online
DOI: 10.1039/D5SC10164F

From Perovskite Top Interfaces to Metal Contacts: Stability-Driven Design for Tandem-Compatible Inverted Solar Cells

Sangmi Park †[a], Jong Bin Park †[b], Jung Min Ha [b], Hye Seung Kim [a], Myoung Hoon Song *[a], Han Young Woo *[b]

[a] S. Park, H. S. Kim, Prof. M. H. Song
Department of Materials Science and Engineering, Ulsan National Institute of Science and Technology (UNIST), UNIST-gil 50, Ulsan, 44919, Republic of Korea.
*E-mail: mhsong@unist.ac.kr

[b] J. B. Park, J. M. Ha, Prof. H. Y. Woo
Department of Chemistry, Korea University, Seoul 02841, Republic of Korea.
*E-mail: hywoo@korea.ac.kr

Keywords: perovskite solar cells, inverted structure, interlayer, tandem solar cell, electron transporting layer, stability

† These authors contributed equally to this work

Electronic Supplementary Information (ESI) available: See DOI: xx.xxxx/xxxxxxxxxx

Abstract

Inverted perovskite solar cells (PeSCs) have attracted growing attention due to their low-temperature processability, reduced hysteresis, and strong compatibility with flexible and tandem device architectures, and have now surpassed conventional devices in terms of both power conversion efficiency and operational stability. Despite these advantages, their long-term operational stability remains critically constrained by the upper device stack, spanning from the perovskite surface through the electron-transporting layer (ETL) to the metal cathode. This review systematically analyzes the dominant origins of instability at these top interfaces in inverted PeSCs and organizes recent progress into three key design directions: (i) perovskite/ETL interface engineering using organic and inorganic modifiers, low-dimensional perovskite capping layers, and thermally conductive interlayers; (ii) C_{60} replacements or non-

fullerene ETLs that integrate defect passivation, interfacial dipole tuning, ion management, and aggregation-resistant morphologies; and (iii) ETL/cathode interlayers that regulate band bending, suppress interfacial recombination, and block volatile halide migration. Finally, the outlook section discusses emerging opportunities and remaining challenges in further optimizing ETLs and top interlayers, with particular emphasis on advancing the operational stability and commercial viability of inverted PeSCs and their integration into high-performance tandem solar cells.

1. Introduction

Over the past decade, perovskite solar cells (PeSCs) have exhibited a steep increase in power conversion efficiency (PCE), reaching approximately 27.0% for single-junction devices, thereby establishing PeSCs as one of the most promising next-generation photovoltaic technologies.[1-5] Early efficiency gains were primarily driven by the conventional n-*i*-p architecture; however, the inverted p-*i*-n configuration has rapidly matured and, in many cases, surpassed n-*i*-p devices in both efficiency and operational stability (**Table 1**). As a result, inverted PeSCs have attracted growing attention due to their low temperature processability, reduced hysteresis, and strong compatibility with flexible and tandem device architectures.

The operating principle of PeSCs begins with photon absorption in the perovskite layer, generating electron–hole pairs. Owing to the low exciton binding energy of perovskites, these photogenerated species readily dissociate into free carriers at room temperature. The built-in electric field and interfacial energy-level offsets then drive carrier transport, with electrons selectively extracted across the perovskite/electron-transporting layer (ETL) interface to the cathode, and holes transported through the hole-transporting layer (HTL) toward the anode. The overall PCE is therefore governed by the balance between charge generation, transport, recombination, and extraction. In particular, interfacial nonradiative recombination, defect-assisted trap states, ion migration, and chemical reactions at selective contacts critically affect

View Article Online
DOI: 10.1039/D5SC10164F

both efficiency and operational stability. These considerations underscore the central role of interface engineering in optimizing PeSC performance and durability.

A pivotal factor enabling this progress has been the successful implementation of hole-selective self-assembled monolayers (SAMs) at the bottom electrode/perovskite interface.[6-8] SAMs allow precise work function (WF) tuning while minimizing parasitic absorption and simultaneously improving interfacial passivation and charge extraction. These advantages have translated into higher device efficiencies, improved reproducibility, and enhanced stability. Accordingly, extensive SAM-focused studies and reviews have firmly established buried bottom-interface engineering as a cornerstone of high-performance inverted PeSCs.[9–13]

In contrast, despite the substantial advances at the bottom interface, the long-term operational stability of inverted PeSCs is increasingly dictated by processes occurring at the upper device stack, comprising the perovskite top surface, the ETL, and the metal cathode. Recent studies on upper-interface engineering have shown that surface defects,[14-16] interfacial chemical reactions,[17-19] and suboptimal energy-level alignment[20-24] at these junctions can accelerate nonradiative recombination and trigger degradation pathways such as ion migration and electrode corrosion. In addition, commonly used fullerene-based ETLs, including C_{60} and phenyl-C_{61}-butyric acid methyl ester ($PC_{61}BM$), often suffer from thermal and morphological instabilities, which further amplify interfacial degradation under prolonged operational stress.[25-27] These insights highlight that stability-driven device design must extend beyond bottom-interface optimization to encompass comprehensive control over the perovskite top surface and upper-contact architecture.

In this review, we classify the stability bottlenecks at the upper interfaces of inverted PeSCs into key aspects of perovskite surface defects, energy-level misalignment, inefficient heat dissipation, and the intrinsic instability of ETLs. Correspondingly, we discuss stabilization strategies for the upper device stack across three hierarchical levels: (i) perovskite/ETL interface engineering, (ii) the development of C_{60}-alternative ETLs, and (iii) ETL/cathode

View Article Online
DOI: 10.1039/D5SC10164F

interface design (**Fig. 1**). Finally, we outline future directions toward reliable perovskite photovoltaics, encompassing both single-junction and tandem device architectures. Collectively, this review bridges fundamental interfacial understanding with practical design guidelines for achieving long-term stable PeSCs.

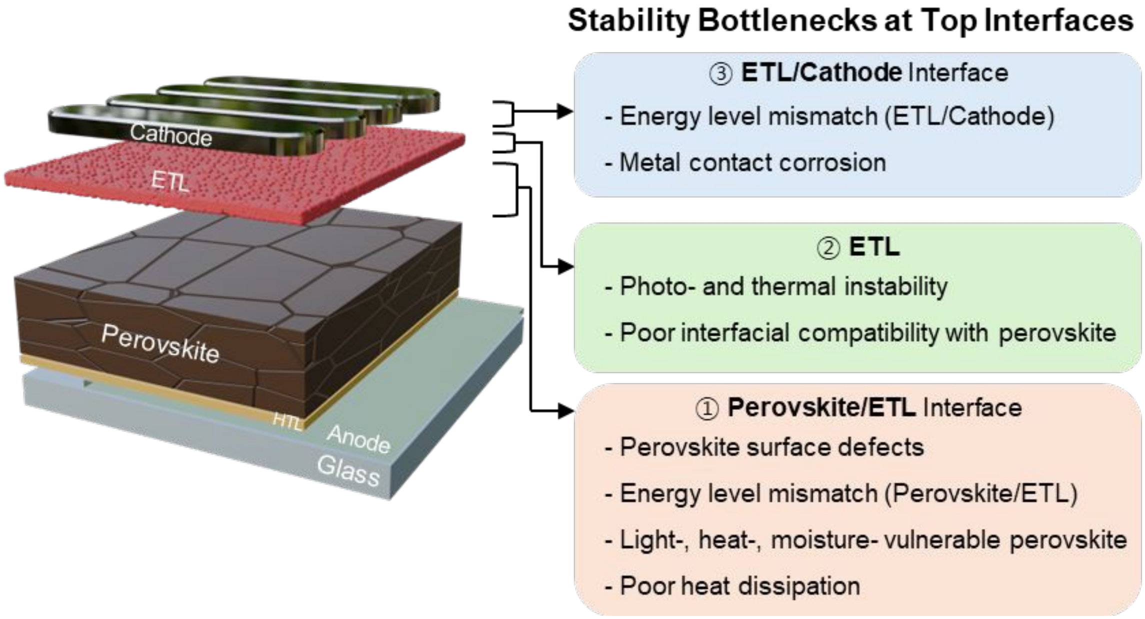

Fig. 1 Schematic of stability bottlenecks at the top interfaces in inverted PeSCs.

Table 1 Summary of the state-of-the-art photovoltaic performance of conventional (n-*i*-p) and inverted (p-*i*-n) PeSCs.

Structure	Device configuration	Cell area (cm^2)	PCE (%)	MPP tracking	Encapsulated	Ref
p-*i*-n	FTO/CbzNaph:JJ24/$Cs_{0.05}FA_{0.85}MA_{0.1}PbI_3$ /$EDAI_2$/C_{60}/SnO_X ALD/Ag	0.0712	26.92	T_{100}: 1,000 h (85 °C, 78-80 % RH)	O	8
p-*i*-n	ITO/NiOx/Me-4PACz/$Cs_{0.05}MA_{0.1}FA_{0.85}PbI_3$/ piperazinium diiodide/ $PC_{61}BM$ /BCP/Ag	0.05556	26.87	T_{96}: 2,500 h (65 °C, 40±5 % RH)	O	28
p-*i*-n	ITO/PhPAPy/$FA_{0.9}MA_{0.05}$Cs0.05PbI_3/3MTPAI/C_{60}/BCP/Ag	0.074	26.74	T_{95}: 2,000 h (65 °C, ambient humidity)	O	29
p-*i*-n	ITO/D4PA/$Cs_{0.05}FA_{0.85}MA_{0.1}PbI_3$/*p*-F-PEAI/$C_{60}$/BCP/Ag	0.0412	26.72	$T_{97.2}$: 2,500h (RT, ambient humidity)	O	30
p-*i*-n	ITO/PATPA+OMe-PhPACz/$FA_{0.85}MA_{0.1}Cs_{0.05}PbI_3$ / piperazinium diiodide/C_{60}/BCP/Cu	0.0715	26.21	T_{90}: 1,000h (N_2 atmosphere)	Not stated	31
p-*i*-n	FTO/NiO_X/Me-4PACz/ $Cs_{0.02}(FA_{0.98}MA_{0.02})_{0.98}Pb(I_{0.99}Br_{0.01})_3$/$PC_{61}BM$/BCP/Ag	0.09	26.17	T_{80}: 423h (85 °C, N_2 atmosphere)	X	32

View Article Online
DOI: 10.1039/D5SC10164F

p-*i*-n	ITO/Me-4PACz/$Cs_{0.05}FA_{0.9}MA_{0.05}PbI_3$/PCNI2-BTI/BCP/Ag	0.15	26.00	T_{80}: 1,280 h (RT, 60±10 % RH)	O	33
p-*i*-n	ITO/MPAcPA/$Cs_{0.04}(MA_{0.05}FA_{0.95})_{0.96}Pb(I_{0.95}Br_{0.05})_3$/SPS/$C_{60}$/BCP/Ag	0.0625	25.85	T_{95}: 1,000h (RT, N_2 atmosphere)	O	34
p-*i*-n	ITO/MPA-CPA/$Cs_{0.15}FA_{0.85}PbI_{2.8}Cl_{0.2}$/(PiEA)$PbI_4$ /$PC_{61}BM$/BCP/Ag	0.06	25.60	T_{93}: 1,000h (RT, N_2 atmosphere)	Not stated	35
n-*i*-p	FTO/SnO_2/ZnTPPS/$Cs_{0.05}FA_{0.95}PbI_3$/Spiro-OMeTAD/Au	0.0618	26.66	T_{90}: 1,537 h (Not stated)	O	36
n-*i*-p	ITO/SnO_2 (HS)/$FAPbI_3$/PEAI/Spiro-OMeTAD/Au	0.08	26.61	$T_{94.9\%}$: 1,800 h (Not stated)	Not stated	37
n-*i*-p	ITO/SnO_2/$FA_{0.94}Cs_{0.06}PbI_3$/CIS QD/Spiro-OMeTAD/Ag	0.0590	26.34	T_{80}: 2,000 h (25 ℃, N_2 atmosphere)	X	38
n-*i*-p	FTO/SnO_2/$AlCl_3$/$(FA_{0.83}MA_{0.06}Rb_{0.12})Pb(I_{0.94}Br_{0.06})_3$/PEAI/Spiro-OMeTAD/Au	0.102	26.29	T_{80}: 502 h (25 ℃, N_2 atmosphere)	X	39
n-*i*-p	FTO/SnO_2/$FAPbI_3$/MeO-PEAI/Spiro-OMeTAD/Au	0.093	26.20	T_{80}: 3,000 h (30–45 °C, 20–35% RH)	O	40
n-*i*-p	FTO/SnO_2/$FA_{0.95}MA_{0.05}Pb(I_{0.95}Br_{0.05})_3$ /MeS-HAI/Spiro-OMeTAD/Au	0.05	25.83	T_{98}: 400 h (30 ℃, N_2 atmosphere)	X	41
n-*i*-p	ITO/LC-modified SnO_2/$(FA_{0.70}Cs_{0.04}Rb_{0.02}MA_{0.25})Pb(I_{0.87}Br_{0.01}Cl_{0.12})_3$ /PEAI/Spiro-OMeTAD/Ag	0.10	25.30	$T_{90.17}$: 1,000 h (40±5 ℃, N_2 atmosphere)	X	42

*MPP: Maximum power point / RT: Room temperature

2. Stability issues on top layers of inverted PeSCs

2.1. Surface defects of perovskite

Metal–halide perovskites (MHPs) crystallize in the ABX_3 structure, where A is a monovalent cation (methylammonium (MA^+), formamidinium (FA^+), or cesium (Cs^+)), B is a divalent metal cation (Pb^{2+} or Sn^{2+}), and X is a halide anion (Cl^-, Br^-, or I^-). The A-site cations occupy the cavities of the lattice, while corner-sharing $[BX_6]^{4-}$ octahedra form the inorganic framework. Owing to their ionic bonding and mechanically soft lattice, MHP thin films inherently accommodate a high density of point defects, which are preferentially concentrated at surfaces and grain boundaries where structural rigidity is low.[43-45] These defects include vacancies (V_A, V_{Pb}, and V_X), interstitials (A_i, Pb_i, and X_i), and antisite defects (A_{Pb}, Pb_A, A_X, Pb_X, X_A, and X_{Pb}) (**Fig. 2a**).[46-47] MHPs are often described as defect-tolerant materials because many intrinsic

View Article Online
DOI: 10.1039/D5SC10164F

point defects introduce shallow electronic states near the band edges rather than deep mid-gap traps. Nevertheless, even shallow defects can substantially influence nonradiative recombination, ion migration, interfacial energetics, and long-term stability.[48-49] Under continuous illumination, electrical bias, or thermal stress, these initially benign defects may evolve into deep traps or activate defect-mediated processes such as ion migration and phase segregation.[50] Consequently, defect tolerance in terms of electronic structure does not directly translate into structural or operational stability, and defect formation and passivation remain central challenges in perovskite photovoltaics.

Importantly, shallow defects also play a pivotal role in the temporal evolution of degradation. Under-coordinated Pb^{2+} species, for example, act as nonradiative recombination centers that limit optoelectronic performance and can be irreversibly reduced to metallic Pb^0, thereby undermining chemical stability.[51-53] Iodide interstitials facilitate halide migration and can accelerate phase transitions, such as the cubic-to-hexagonal transformation, which compromise structural integrity.[54] Vacancies further exacerbate degradation by lowering migration barriers, enabling a continuous redistribution of ionic species.[55-56] Through these coupled processes, initial surface defects act as nucleation sites for a self-amplifying defect-generation cycle, progressively increasing trap density, enhancing Shockley–Read–Hall recombination, and driving gradual losses in open-circuit voltage (V_{OC}) and fill factor (FF), even when the initial device efficiency is high. Thermal and mechanical factors further intensify defect formation at the perovskite surface. High-temperature annealing promotes the evaporation of volatile MA^+/FA^+ cations and halide species, leaving PbI_2-rich regions and under-coordinated Pb^{2+} sites. In parallel, residual tensile strain arising from rapid solvent evaporation or thermal expansion mismatch lowers defect formation energies, rendering the lattice more susceptible to vacancy generation during subsequent operation.[57-59] As a result, defects in MHPs are not static imperfections but dynamic entities that continuously proliferate throughout the device lifetime.

View Article Online
DOI: 10.1039/D5SC10164F

The vulnerability of surface defects is further amplified by exposure to extrinsic environmental stimuli, particularly at the top surface of inverted PeSCs. Unlike the buried HTL /perovskite interface, the perovskite top surface is directly exposed to oxygen, moisture, and ambient contaminants during and after fabrication. Under illumination, photogenerated electrons can reduce adsorbed O_2 to superoxide (O_2^-), which is a highly reactive species (**Fig. 2b**).[17] O_2^- extracts protons from MA^+, forming methylamine and water, while parallel oxidation pathways generate I_2 or HI. The loss of A-site cations destabilizes the perovskite lattice, leading to decomposition into PbI_2 and the release of volatile iodine-containing species. Each decomposition step creates additional halide vacancies and under-coordinated Pb^{2+} sites, thereby feeding back into the intrinsic defect-generation cycle and accelerating long-term degradation. Moisture induces similarly detrimental pathways.[60] Water molecules penetrate to grain boundaries and form hydrated intermediates such as $MAPbI_3 \cdot H_2O$ and eventually $(MA)_4PbI_6 \cdot 2H_2O$. These hydrated phases distort the $[PbI_6]^{4-}$ octahedral framework, weaken A-site binding, and markedly increase ionic mobility. Beyond direct chemical decomposition, hydration significantly lowers the activation energy for halide migration, amplifying secondary defect formation and accelerating the loss of crystallinity.

Taken together, the top surface of inverted PeSCs represents the most vulnerable region where intrinsic defect dynamics and extrinsic degradation pathways converge. Surface defects initiate ionic redistribution, environmental species chemically destabilize the lattice, and illumination and electrical bias further reduce migration barriers. This synergistic interplay leads to a time-dependent expansion of defect populations and cumulative structural decomposition. Ultimately, these processes manifest as reduced carrier lifetimes, enhanced nonradiative recombination, and progressive deterioration of device efficiency and operational stability.

2.2. Energy level alignment between perovskite and ETL

Fullerene-based ETLs are widely employed in inverted PeSCs due to their high electron mobility and compatibility with low-temperature processing. Nevertheless, voltage losses and stability limitations in fullerene-contacted inverted PeSCs can originate from multiple interfacial factors, including (i) Fermi-level pinning induced by interfacial states that masks the intended band alignment,[61-62] (ii) trap-assisted recombination at the perovskite/ETL interface,[63-64] and (iii) bias-/illumination-activated interfacial reactions that generate new defect states over time.[65-66] In this section, we specifically focus on an alignment-driven instability pathway at the perovskite/ETL interface, where the energetic offset governs interfacial charge accumulation and the subsequent electrostatic and ionic responses during operation.

Common fullerene-based ETLs possess relatively deep lowest unoccupied molecular orbital (LUMO) levels (e.g., $PC_{61}BM$: −3.9 eV, $PC_{71}BM$: −4.2 eV, C_{60}: −4.1 eV, C_{70}: −4.0 eV, ICBA: −3.7 eV, and Bis-$PC_{60}BM$: −3.8 eV).[67–72] When the ETL LUMO lies substantially below the perovskite conduction band minimum (CBM), a large negative energetic offset (static energetic misalignment) is created, which facilitates electron transfer from the perovskite into the ETL. While such an offset is beneficial for efficient electron extraction, an excessively deep ETL LUMO can lead to pronounced electron accumulation within the ETL and at the perovskite/ETL interface, effectively causing the ETL to function as an electron reservoir.[73] The resulting negative charge density on the ETL side electrostatically attracts holes and positively charged ionic species (e.g., MA^+, FA^+, V_X^+) toward the perovskite side of the interface (**Fig. 2c**). This interfacial charge separation generates a strong local electric field and enhanced band bending, dynamically reshaping the interfacial energy landscape during device operation.[74]

In MHPs, the resulting interfacial electric field can induce time-dependent redistribution and accumulation of mobile ions; under operating illumination and/or applied bias, these ionic processes are further accelerated, making the interfacial electrostatics increasingly time-

View Article Online
DOI: 10.1039/D5SC10164F

dependent (dynamic electrostatics). As a consequence, electron selectivity at the contact is reduced, allowing holes to approach the ETL more readily and thereby enhancing interfacial nonradiative recombination near the junction. Consequently, the enhanced interfacial nonradiative recombination locally reduces the quasi-Fermi level splitting (QFLS) by narrowing the separation between the electron and hole quasi-Fermi levels, which manifests as quasi-Fermi level bending at the interface (**Fig. 2d**). The externally measured V_{OC} can thus be suppressed beyond what would be expected from the bulk QFLS, resulting in an increased QFLS–qV_{OC} mismatch (q: elementary charge).

Because ionic redistribution occurs on relatively slow timescales, the extent of charge accumulation, band bending, and contact selectivity evolves during operation. This dynamic behavior manifests macroscopically as time-dependent voltage and FF drifts, as well as exacerbated hysteresis. In this regime, inefficient extraction at the perovskite/ETL interface causes photogenerated carriers to accumulate near the junction, further increasing recombination losses and reinforcing the degradation of charge-extraction efficiency. Over extended operation, sustained ion accumulation at the interface can promote additional defect formation by facilitating halide-vacancy generation and ionic rearrangement. Ion-rich interfacial regions also increase chemical reactivity with metal electrodes, such as Ag, enabling interdiffusion and accelerating contact corrosion.[75-77] Moreover, in the presence of oxygen and moisture, the elevated interfacial charge and ion density lowers the activation barriers for electrochemical reactions, further amplifying interfacial degradation and long-term instability.

To experimentally substantiate these coupled electrostatic, ionic, and chemical degradation processes at the upper contact, complementary diagnostics that probe both nonradiative losses and operando interfacial evolution are essential. Absolute photoluminescence quantum yield (PLQY) measurements, together with the corresponding QFLS, provide a quantitative metric of radiative efficiency and enable direct comparison with the measured V_{OC} to assess the magnitude and origin of the QFLS–qV_{OC} mismatch.[63-64] Electroluminescence (EL) under forward bias further sensitizes contact-related nonradiative recombination and voltage losses.[78-79] In addition, transient photovoltage/photocurrent (TPV/TPC), impedance spectroscopy, transient photoluminescence (TRPL) can resolve the characteristic timescales of charge accumulation and ion redistribution that underpin time-dependent voltage/FF drifts and hysteresis.[64, 80-82] Finally, operando spectroscopy can directly track the evolution of interfacial energetics, chemical reactions, and ionic redistribution during operation.

2.3. Low thermal conductivity of perovskite

MHPs, owing to their predominantly ionic bonding, are inherently vulnerable to extrinsic stimuli such as moisture, oxygen, heat, and light. While advanced encapsulation technologies can effectively mitigate degradation induced by moisture and oxygen, thermal instability remains a fundamental challenge that cannot be fully addressed by encapsulation alone and instead requires improvements in the intrinsic stability of PeSCs. Under continuous 1-sun illumination, operating device temperatures typically reach 40–65 °C.[83] In addition, substantial internal heat is generated through carrier-related processes, including Joule heating, bulk and interfacial recombination, and the thermalization of high-energy photons.[84] Heat stress is therefore unavoidable during operation, making effective thermal management and intrinsic thermal robustness essential for long-term device stability.

Beyond their chemical sensitivity, perovskites suffer from intrinsically low thermal conductivity, which further aggravates thermal degradation. In these materials, heat transport is dominated by lattice vibrations (phonons) rather than free charge carriers.[85] However, a combination of structural and vibrational characteristics severely limits phonon-mediated heat transport, resulting in a lattice thermal conductivity typically below 1.0 W m^{-1} K^{-1} at room temperature (**Fig. 3a**). Inefficient phonon transport in perovskites can be attributed to three primary factors. First, their crystal lattices are mechanically soft and strongly anharmonic,

View Article Online
DOI: 10.1039/D5SC10164F

causing phonons to propagate slowly and undergo frequent phonon–phonon scattering.[86] This vibrational nonlinearity shortens phonon lifetimes and substantially reduces thermal conductivity. Second, the dominant heat-carrying phonon modes exhibit relatively flat dispersion relations and intrinsically short lifetimes, further suppressing heat transport. The presence of heavy elements such as Pb and I exacerbate these effects by increasing lattice distortion and phonon scattering.[87] Third, the high density of defects at surfaces and grain boundaries—including vacancies, dislocations, and dangling bonds—acts as additional phonon-scattering centers, reducing phonon mean free paths and further degrading thermal transport.[88-90]

As a result of this intrinsically poor heat dissipation, MHPs are prone to local heat accumulation under thermal stress, which activates a cascade of coupled degradation processes. Elevated temperatures promote the decomposition of perovskites into PbX_2 and volatile AX-derived species, leading to irreversible loss of the perovskite phase and a concomitant increase in defect density.[91-92] The soft and anharmonic lattice also facilitates thermally driven phase transitions, such as the transformation from the photoactive black α-phase to the non-perovskite yellow δ-phase in iodide-based compositions.[93-94] Simultaneously, higher temperatures significantly accelerate the migration of mobile ionic species, including halide anions and A-site cations, resulting in halide segregation and local compositional inhomogeneity.[18, 95-96] Thermally activated ion migration further intensifies interfacial reactions with charge-transport layers and metal electrodes, promoting the formation of interfacial defects and corrosion products that impede charge extraction and exacerbate performance loss. Collectively, these thermally induced processes underscore that inefficient heat dissipation is not merely a secondary issue but a central driver of structural, electronic, and interfacial instability in PeSCs. Consequently, engineering more efficient heat-dissipation pathways and thermally robust interfacial architectures has emerged as a critical strategy for achieving long-term thermal stability in perovskite solar cells.

View Article Online
DOI: 10.1039/D5SC10164F

2.4. Instability of ETL material

Fullerene-based ETLs, such as C_{60} and $PC_{61}BM$, are widely employed in inverted PeSCs owing to their high electron mobility and energetically favorable alignment with the perovskite CBM. However, their intrinsically nonpolar molecular nature results in poor interfacial compatibility with the highly polar perovskite surface, leading to weak interfacial adhesion and substantial interfacial recombination losses.[97-98] Although the introduction of polar functional groups has been explored to improve compatibility, such modifications are intrinsically limited in fullerene systems due to their rigid cage structure and synthetic constraints. This weak interfacial compatibility becomes particularly problematic in Si-perovskite tandem architectures, where additional contact layers are required. For example, delamination of tin oxide (SnO_2) deposited on $PC_{61}BM$ by atomic layer deposition (ALD) has been observed, originating from the intrinsically weak physisorption-dominated adhesion at the $PC_{61}BM/SnO_2$ interface (**Fig. 3b**).[99] Subsequent thermal processing and sputtering steps, such as indium zinc oxide (IZO) deposition, further exacerbate this issue by introducing mechanical and thermal stress, ultimately promoting stick–slip-type interfacial separation.

Beyond interfacial compatibility with adjacent contact layers, fullerene-based ETLs also suffer from intrinsic material instability under prolonged thermal and illumination stress. As shown in **Fig. 3c**, although C_{60} initially forms a uniform and fully covered layer on the perovskite surface, extended thermal aging induces severe molecular aggregation, resulting in incomplete surface coverage.[27] $PC_{61}BM$ exhibits similar behavior under continuous thermal annealing and light-soaking conditions, where pronounced aggregation and pinhole formation are observed in perovskite/$PC_{61}BM$ films.[100-101] This morphological instability arises from the weak perovskite-fullerene interactions and high surface energy of fullerene molecules, which promote self-aggregation during thermal aging. Consequently, incomplete coverage (often <80%) and aggregated morphologies lead to non-uniform interfacial contact, discontinuous electron-transport pathways, increased series resistance (>10 Ω·cm^2), and enhanced trap-assisted recombination, with carrier lifetimes reduced to tens of nanoseconds or less.[102-104] Importantly, repeated reports of morphological instability—stemming from limited solubility, poor film uniformity, and aggregation-induced degradation—persist despite extensive efforts to chemically modify fullerene derivatives.[105] This indicates that such instability is not confined to specific molecular structures but is instead an inherent limitation of fullerene-based ETLs. As a result, intrinsic morphological instability represents a major bottleneck for achieving long-term operational stability in inverted PeSCs.

Beyond morphological degradation, fullerene-based ETLs are vulnerable from chemical and photochemical stability perspectives. Even under oxygen-free (inert) conditions, photoexcited fullerenes can undergo photodimerization through cage–cage bonding (**Fig. 3d**), which alters charge-transport properties and modifies the trap-state distribution within the ETL. These changes can induce early-stage performance fluctuations, such as burn-in behavior, and contribute to long-term degradation.[106] Under simultaneous exposure to light and ambient oxygen, functionalized fullerenes such as PC$_{61}$BM undergo photo-oxidation, forming epoxide and carbonyl defects on the fullerene cage.[107-109] Notably, oxidation of less than 1% of the fullerene content has been reported to significantly reduce V_{OC}, short-circuit current density (J_{SC}), and FF by lowering electron mobility and introducing deep trap states, resulting in rapid efficiency loss.[110] Similar photo-oxidative degradation pathways have been widely observed across structurally related fullerene derivatives.[111] Taken together, the stability limitations of fullerene-based ETLs arise from the coupled effects of poor interfacial compatibility, intrinsic morphological instability, and susceptibility to both oxygen-free photoreactions and photo-oxidation under ambient conditions. These fundamental constraints underscore the need for alternative ETL design strategies that move beyond fullerene-based systems to achieve robust long-term stability in inverted PeSCs.

View Article Online
DOI: 10.1039/D5SC10164F

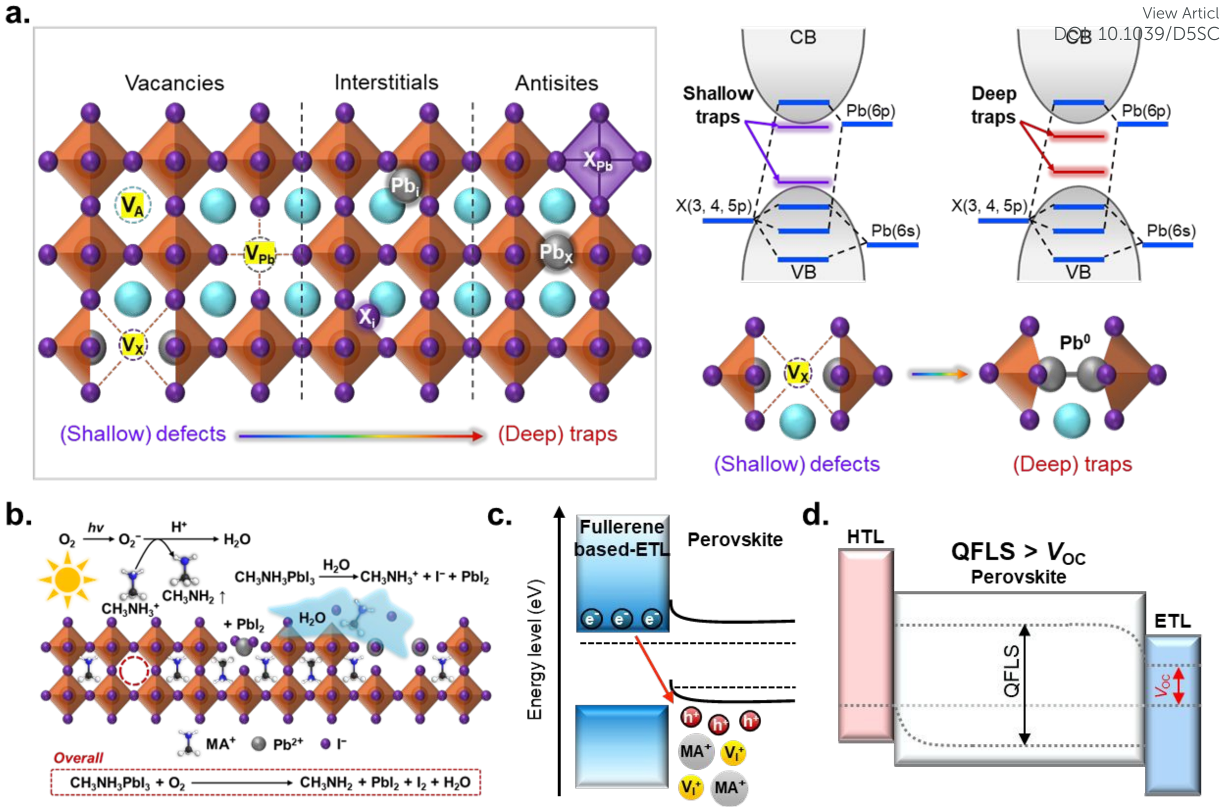

Fig. 2 (a) Schematic diagram of perovskite structure and point defects; V_A (cation vacancy), V_X (halide vacancy), V_{Pb} (lead vacancy), Pb_i (lead interstitial), Pb_X (lead antisite) defects. (b) Schematics of O_2 induced perovskite degradation steps. (c) Energy diagram at ETL/perovskite contact. (d) Schematic band diagrams illustrating QFLS–V_{OC} mismatch in PeSCs arising from interfacial energy-level misalignment.

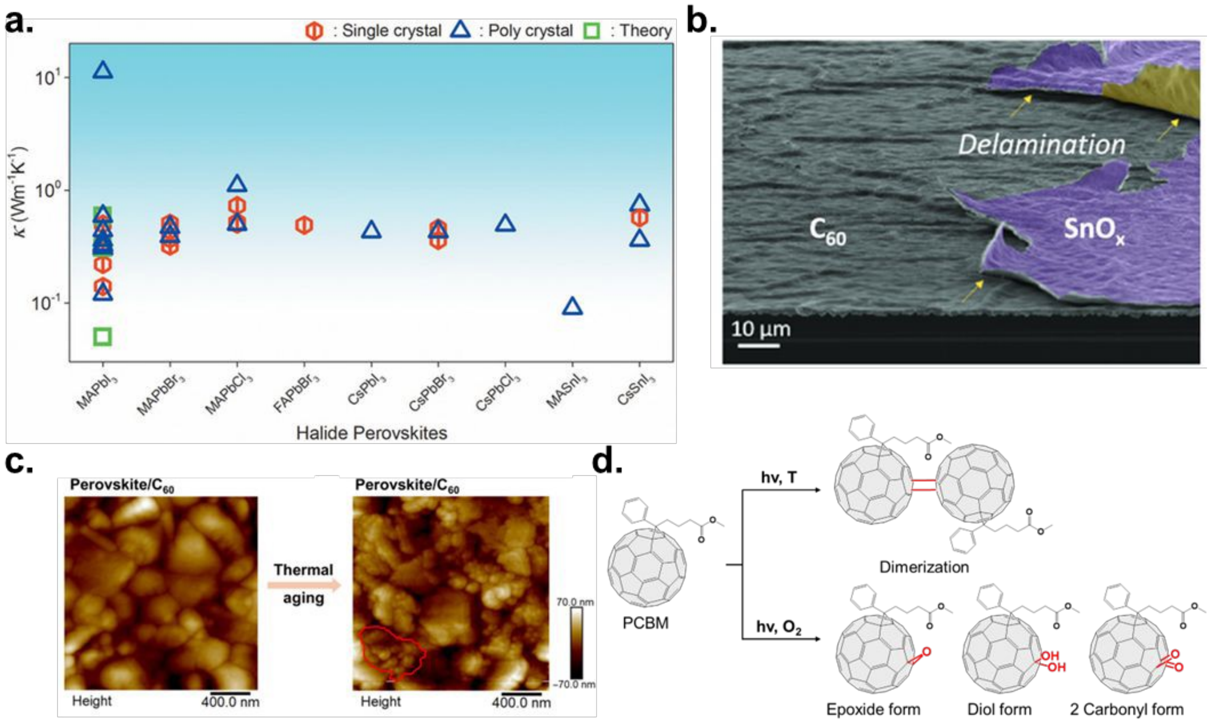

View Article Online
DOI: 10.1039/D5SC10164F

Fig. 3 (a) Room temperature experimental and theoretical κ of perovskites. Reproduced under the terms of the CC-BY Creative Commons Attribution 4.0 International license (https://creativecommons.org/licenses/by/4.0) from Ref.[85]. Copyright 2020, Wiley-VCH GmbH. (b) SEM image of delaminated SnO_x on C_{60} surface. Reproduced with permission from Ref.[99]. Copyright 2022, American Chemical Society. (c) Atomic force microscopy (AFM) topography images of perovskite film covered with C_{60}, before and after thermal aging. Reproduced under the terms of the CC-BY Creative Commons Attribution 4.0 International license (https://creativecommons.org/licenses/by/4.0) from Ref.[27]. Copyright 2024, The American Association for the Advancement of Science. (d) Schematic of fullerene ETL photoreactions: dimerization of $PC_{61}BM$ under light and thermal stress, and photo-oxidation of $PC_{61}BM$ under combined light and oxygen exposure.

3. Top layer engineering for inverted PeSCs

Numerous surface defects—vacancies, interstitials, and antisites—can trap charge carriers, promote ion migration, and induce local heating in perovskites. A widely employed strategy to neutralize these ionic trap sites is Lewis acid/base passivation, in which charged molecules or ionic additives provide electrostatic compensation.[112-114] In this framework, Lewis acids act as electron-pair acceptors, whereas Lewis bases donate electron density to under-coordinated species. Typical Lewis acids include cationic species and fluorinated aromatics; the strong electronegativity of fluorine withdraws electron density from the aromatic ring, generating partial positive character that can bind with halide anions and thereby mitigate halide-related interfacial defects. Lewis bases encompass N-, O-, S-, and P-donor groups (e.g., $–NH_2$, –CN, C–O, O=S=O, P=O), which coordinate with under-coordinated Pb^{2+} sites. Beyond defect passivation, the intrinsic dipole moments of these molecules—or appropriately engineered substituents—can modulate the interfacial vacuum level, enabling more favorable band alignment between the perovskite and adjacent ETLs. Consequently, functional molecules and ionic additives bearing these groups not only suppress surface defects but also contribute to energy-level alignment, protective capping-layer formation, and improved thermal dissipation.

The following section highlights representative organic and inorganic modifiers that leverage these functionalities to simultaneously control defects and optimize perovskite interfaces.

3.1. Perovskite/ETL interface engineering

3.1.1 Organic interlayers at the perovskite/ETL interface

Accordingly, bottlenecks at the top (perovskite/ETL) interface can be mitigated through an integrated molecular-design approach that employs nanometer-scale organic interlayers capable of simultaneously (i) suppressing defect- and ion-mediated recombination,[115] (ii) reconfiguring band alignment through molecular dipoles,[116] (iii) establishing stepwise energy alignment to block hole and accelerate electron extraction,[21] and (iv) enhancing device durability by introducing hydrophobicity, ion-trapping motifs.[117] Representative interlayer strategies include (i) charge-transfer–bridge fullerene layers that combine defect passivation with electron bridging, (ii) dipolar salts, (iii) functionalized fullerene electrolytes, and (iv) thin organic spacers that moderate direct C_{60} contact while maintaining efficient electron extraction.

In inverted devices with the structure indium tin oxide (ITO)/NiOx/SAM/ $FA_{0.9}Cs_{0.1}PbI_{2.9}Br_{0.1}$/interlayer/$PC_{61}BM$/ bathocuproine (BCP)/Ag (**Fig. 4a**), Mo et al. addressed this by introducing a phosphonic-acid–fullerene conjugate (CPPA).[118] The phosphonic acid group passivates perovskite surface defects, whereas the fullerene backbone forms a charge-transfer bridge to $PC_{61}BM$. This single molecule therefore unifies defect passivation, dipole-driven energy-level tuning, and electron bridging, collectively lowering interfacial recombination and accelerating extraction. As a result, both V_{OC} and FF increase relative to using a simple phosphonic-acid layer, and the champion PCE improves from ~22% to ~24–25% in $FA_{0.9}Cs_{0.1}PbI_{2.9}Br_{0.1}$ and $Cs_{0.05}(FA_{0.98}MA_{0.02})_{0.95}Pb(I_{0.98}Br_{0.02})_3$ absorbers respectively. Mechanistic characterization by density functional theory (DFT) reinforces this picture: **Fig. 4b** shows CPPA located precisely at the perovskite/ $PC_{61}BM$ contact to create a dedicated electron-transfer channel. Charge-density-difference ($\Delta\rho$) and electron-localization-

View Article Online
DOI: 10.1039/D5SC10164F

function (ELF) maps indicate multisite cooperative binding through O–Pb coordination and OH···I hydrogen bonding, accompanied by strengthened conjugation across the $PC_{61}BM$ – perovskite interface. Ultraviolet photoelectron spectroscopy (UPS) further reveals an upward shift of the Fermi level and conduction-band edge, evidencing a reduced electron-extraction barrier, which manifests electrically as decreased series resistance and increased shunt resistance (**Fig. 4c**). Stability improvements are equally notable, highlighting the synergistic effects of CPPA-enabled top-interface engineering.

A second notable example is a dipolar organic salt, piperazinium diiodide, introduced by Zheng et al. as a multifunctional surface modifier that concurrently alleviates deep traps and unfavorable band alignment.[22] Unlike conventional ammonium halides that readily induce low-dimensional phases, piperazinium diiodide predominantly remains in its molecular form on the surface, suppressing deprotonation reaction between A-site cations and the formation of deep-level defects (iodine interstitials) on the surface. X-ray photoelectron spectroscopy (XPS) analysis in **Fig. 4d** indicates that the control sample exhibits a peak assigned to deprotonated FA (C–N, ~399 eV), whereas no FA-related signal is detected for the piperazinium diiodide-treated film. Instead, a weak peak corresponding to piperazinium diiodide (C–N–C, ~402 eV) is observed. According to DFT calculations, the formation energy of iodine interstitials increases from 1.403 eV to 3.459 eV upon piperazinium diiodide adsorption, suggesting that piperazinium diiodide inhibits the formation of surface iodine interstitial defects (**Fig. 4e**). Depth-profiling UPS reveals a downward band bending in the piperazinium diiodide-treated perovskite, which facilitates electron extraction while suppressing hole backflow. This behavior is attributed to the positively charged $–NH_2^+$ moieties in piperazinium diiodide, which act as electron-withdrawing groups and draw electron density from interfacial Pb and I species, thereby establishing an interfacial dipole and an enhanced built-in electric field (**Fig. 4f**). These interfacial modifications translate directly into record photovoltaic performance. In devices with FTO/SAM/$Cs_{0.05}(FA_{0.98}MA_{0.02})_{0.95}PbI_3$/interlayer/$C_{60}$/BCP/Cu, a champion PCE of 26.15%

View Article Online
DOI: 10.1039/D5SC10164F

(certified 25.87%, quasi-steady-state 25.52%) is achieved with V_{OC} = 1.18 V and FF = 86.2%, while a 1.028 cm² device delivers 24.18%, demonstrating scalability. Stability is likewise exceptional, with unencapsulated devices retaining 94.2% of initial PCE after 1,000 h of maximum power point (MPP) tracking and 90.4% after 4,500 h at 85 °C.

To effectively mitigate traps and hysteresis at the top interface, it is essential to target both positively charged metal defects (under-coordinated Pb^{2+}/Sn^{2+}) and negatively charged defects (V_A^-, X_i^-). In inverted devices configured as FTO/NiOx/$MAPbI_3$/interlayer/$PC_{61}BM$/SnO_2/Ag, Wang et al. addressed this dual requirement by designing a halogen- and quaternary-ammonium–functionalized fullerene (C_{60}-DBI-R) can passivate both positively and negatively charged defects due to its ionic ammonium-salt motif, providing complementary charge sites at the perovskite interface (**Fig. 4g**).[119] DFT-derived electrostatic potential (ESP) maps show that the negative potential is concentrated on the counter halide in the ammonium-salt group, enabling strong electrostatic binding to under-coordinated metal-cation (Pb^{2+}) defects (**Fig. 4h**). Meanwhile, the cationic ammonium group ($-NR_xH_{4-x}^+$) can electrostatically stabilize negatively charged defect sites and halide-rich surface species, thereby realizing dual-channel defect passivation. This bidirectional repair of incomplete surface coordination suppresses ion migration and reduces trap density which can be identified from the XPS data on **Fig. 4i**. The Pb 4f and I 3d peak shifts after C_{60}-DBI-R treatment suggest interfacial electrostatic interactions between halide anions and undercoordinated Pb^{2+}, as well as between ammonium cations and I^-. As a result, surface traps and interfacial charge accumulation decrease, mitigating V_{OC} and FF losses and suppressing hysteresis. Performance trends are consistent with this mechanism. Across the halogen series, C_{60}-DBI-F/Cl/Br/I achieves PCEs of 20.31/20.70/19.93/19.44%, respectively, while the unmodified device remains at 18.58%.

In Sn–Pb narrow-bandgap (NBG) devices, the relatively larger conduction band offset at perovskite/C_{60} interface can lead to severe misalignment with the ETL. Moreover, surface Sn^{2+} oxidizes to Sn^{4+} upon exposure to air and moisture, inducing p-type doping and increasing the minority-carrier density at the perovskite/ETL interface. To address these issues, Maxwell et al. inserted a thin oleic acid (OA) interlayer between the perovskite and C_{60}, which serves as both a buffer and a passivation layer (**Fig. 4j**).[120] XPS shows that OA treatment slightly shifts the Sn $3d_{3/2}$ and Sn $3d_{5/2}$ peaks to lower binding energy, indicating carboxylic-acid coordination to surface Sn^{2+}, while simultaneously reducing the Sn^{4+} fraction (**Fig. 4k**). By suppressing the formation of Sn^{4+} sites, the OA interlayer strengthens surface n-type character and shifts the Fermi level upward by ~0.25 eV, thereby lowering the minority-carrier concentration at the C_{60} interface (**Fig. 4l**). As a result, OA modification of the NBG top interface enabled monolithic tandem solar cells (ITO/NiOx/Me-4PACz/$FA_{0.8}Cs_{0.2}Pb(I_{0.6}Br_{0.4})_3$/$C_{60}$/ALD-$SnO_x$/Au(1 nm)/PEDOT:PSS/ $Cs_{0.05}FA_{0.7}MA_{0.25}Pb_{0.5}Sn_{0.5}I_3$/$C_{60}$/ALD-$SnO_x$/Ag) with a PCE of 27.3% (certified 26.4%) and a V_{OC} of 2.21 V.

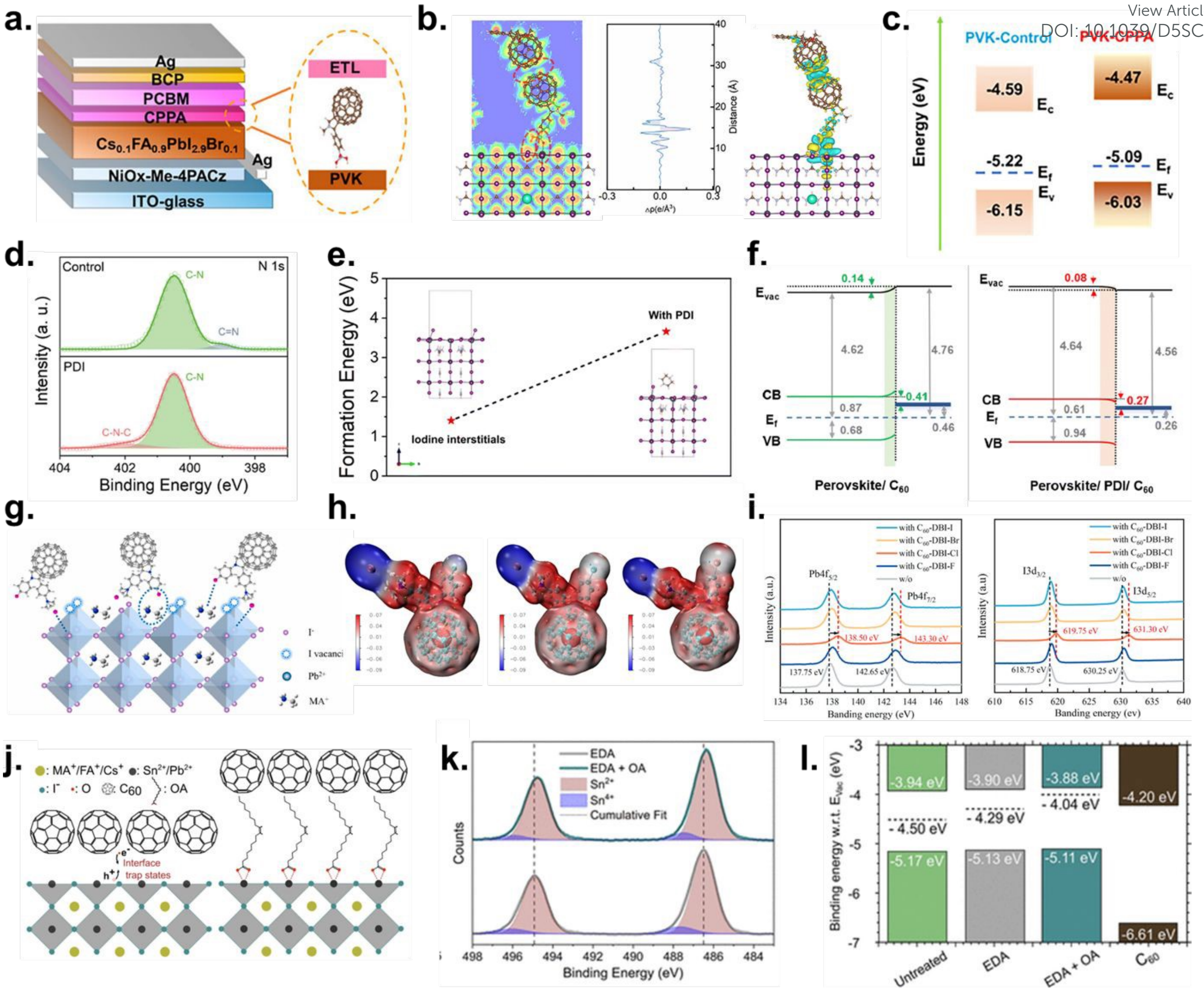

Fig. 4 (a) Device architecture and chemical structure of CPPA. (b) DFT Δρ maps for representative adsorption models on the perovskite surface, vertically integrated Δρ profiles, and the ELF of the CPPA/ $PC_{61}BM$ /perovskite stack. (c) Energy band diagram. Reproduced with permission from Ref.[118]. Copyright 2025, Wiley-VCH GmbH. (d) N 1s XPS spectra of control and piperazinium diiodide-treated perovskite films. (e) DFT formation energies of iodine-interstitial defects with and without piperazinium diiodide; model of piperazinium diiodide adsorption on PbI_2-terminated $FAPbI_3$(100). (f) Energy-level diagrams of perovskite/C_{60} and perovskite/piperazinium diiodide/C_{60} heterointerfaces, highlighting the reduced extraction barrier with piperazinium diiodide. Reproduced with permission from Ref.[22]. Copyright 2024, The Royal Society of Chemistry. (g) Schematic of the C_{60}-DBI-I/perovskite interaction. (h) ESP profiles of C_{60}-DBI-F, Br, I. (i) Pb 4f (left) and I 3d (right) XPS spectra of the perovskite films with/without C_{60}-DBI-R. Reproduced with permission from Ref.[119]. Copyright 2023, Elsevier Ltd. (j) Schematic of perovskite/C_{60} contact with and without OA-interlayer. (k) XPS spectra of Sn 3d core levels for perovskite films, without and with OA-post

View Article Online
DOI: 10.1039/D5SC10164F

treatment. (l) Band alignment diagrams. Reproduced with permission from Ref.[120]. Copyright 2024, American Chemical Society.

3.1.2. Inorganic interlayers at the perovskite/ETL interface

In contrast to organic molecular agents, inorganic interlayers have recently emerged as a robust and multifunctional strategy for stabilizing the perovskite/ETL interface.[64, 121-123] While organic modifiers are highly versatile—providing tunable dipoles and effective defect passivation—their thermal and environmental stability remains limited. Inorganic species such as metal oxide clusters, ultrathin oxides, and metal–fluoride or organometallic complexes offer stronger chemical bonding to surface cations, more effective suppression of ion migration, and greater resistance to moisture, oxygen, and heat. These attributes not only mitigate the chemical reactivity at the perovskite/C_{60} interface but also introduce intrinsic dielectric screening and favorable band-edge modulation, thereby addressing both electronic and stability bottlenecks. Importantly, many inorganic interlayers are compatible with industrially scalable processes including ALD and thermal evaporation, positioning them as promising candidates for tandem-ready device architectures.

Li et al. demonstrated that molecular tailorable titanium oxide clusters (CTOCs) serve as highly effective inorganic interlayers at the perovskite/ETL interface. CTOCs, constructed from Ti–O–Ti cage frameworks and functionalized with ligands (phenyl (CTOCPh), p-fluorophenyl (CTOCPh-F), and pentafluorophenyl (CTOCPh-5F)), provide atomic-level structural precision and establish strong quadrupole–dipole interactions with the adjacent C_{60} layer.[27] As depicted in **Fig. 5a**, the CTOC-series clusters exhibit a doughnut-like structure with an inner diameter of 0.83 nm, matching well with the size of a single C_{60} molecule to restrain the C_{60} movement under heating. The negatively polarized F-substituted phenyl groups on CTOC enable Pb-F bonds with the PbI_2-rich (100) termination of the perovskite, showing a strong binding between perovskite and clusters (**Fig. 5b**). By forming a lattice-matched cluster/perovskite interface, the interlayer alleviates the strain and lattice distortion that develop during aging. Moreover, the strong electronegativity of the fluoro group modulates the WFs which facilitates charge transfer between the perovskite and C_{60} (**Fig. 5c**). When incorporated into inverted PeSCs (ITO/CbzNaph/$FA_{0.80}MA_{0.14}Cs_{0.06}PbI_3$/CTOC derivatives/$C_{60}$/BCP/Ag), CTOCPh-5F yielded a champion PCE of 25.6% (V_{OC} = 1.18 V, FF = 84.90%), with excellent durability—retaining 98% of initial PCE after 1,500 h of MPP tracking and 93% after 1,000 h at 85 °C. These results highlight how inorganic molecular clusters can concurrently deliver defect passivation, quadrupole anchoring, and long-term operational stability.

Liu et al. further showed that inserting a ~1 nm ultrathin metal fluoride (MgF_x) layer by thermal evaporation at the perovskite/C_{60} interface effectively prevents direct fullerene–perovskite contact, thereby reducing interfacial nonradiative recombination and lowering mid-gap defect states.[124] UPS and low-energy inverse photoemission spectroscopy (LE-IPES) measurements reveal favorable downward band bending upon MgF_X insertion, with the perovskite CBM shifting closer to the Fermi level and aligning more optimally with the C_{60} LUMO (**Fig. 5d**). This effect is attributed to an interfacial dipole generated by sub-stoichiometric MgF_X ($x \approx 1.0 \pm 0.2$), which lowers the local work WF and drives electrons toward C_{60} (**Fig. 5e**). The ultrathin MgF_x layer still allows efficient electron tunneling, maintaining selective contact functionality. Implementing this modification in monolithic Si-perovskite tandems (Si bottom cell/2PACz/$Cs_{0.05}FA_{0.8}MA_{0.15}Pb(I_{0.755}Br_{0.255})_3$/metal fluoride/$C_{60}$/$SnO_2$/IZO/Ag/$MgF_X$) yielded a certified stabilized PCE of 29.3%, with a V_{OC} of 1.92 V and FF of 80.70%. Damp-heat testing (85 °C, 85% RH) demonstrated >95% retention after 1,000 h, underscoring the dual performance–stability advantages of inorganic fluoride layers.

Artuk et al. advanced this strategy by introducing an ALD-grown aluminum oxide (AlO_X) layer as a universal inorganic interlayer for the perovskite/C_{60} interface.[125] Unlike hygroscopic alkali fluorides (NaF, LiF, MgF_X), ALD-AlO_X produces an ultrathin (~1.4 nm), conformal crystalline layer that chemically interacts with surface Pb–halide species. XPS analysis shows that AlO_X and its precursor (trimethylaluminum, TMA) react with residual PbI_3^- and Pb^0, oxidizing Pb^0 to Pb^{2+} and eliminating shallow donor-like states that contribute to nonradiative loss (**Fig. 5f**). This process reduces the n-type surface character, evidenced by a 0.2 eV upward shift in the valence band maximum (VBM) and an increased WF, producing more balanced band alignment and reduced majority-carrier offsets at the perovskite/C_{60} junction (**Fig. 5g, h**). When the dense AlO_X layer applied to monolithic Si-perovskite tandems (Si bottom cell/ITO/Me-4PACz/SiO_x-NP/$Cs_{0.05}(FA_{0.9}MA_{0.1})_{0.95}Pb(I_{0.8}Br_{0.2})_3$/ALD-$AlO_X$/$C_{60}$/$SnO_X$/IZO/Ag/LiF), a certified efficiency of 29.9% was achieved with a V_{OC} exceeding 1.92 V. The operational stability tests were conducted for 140 h, after which the champion AlO_X device retained 94.5% of its initial efficiency, whereas the device without AlO_X retained only 70%.

Taken together, the studies discussed above highlight several practical design strategies for organic and inorganic modifiers that enable high-performance and durable perovskite/ETL contacts. The most effective interlayers are multifunctional, simultaneously (i) passivating defect- and ion-mediated nonradiative recombination pathways, (ii) tuning band alignment through interfacial dipoles or band bending, and (iii) maintaining—or even enhancing—efficient interfacial charge transfer rather than acting as an insulating barrier. Organic modifiers offer exceptional tunability in terms of dipole moments, binding motifs, and hydrophobicity; however, their thermal and environmental robustness can be limited. In contrast, inorganic interlayers generally provide stronger interfacial bonding, more effective suppression of ion migration, and improved tolerance to heat and moisture, often with superior process compatibility for tandem architectures and scalable deposition techniques such as ALD or thermal evaporation. From a manufacturability perspective, a critical requirement is achieving nanometer-scale interlayers with conformal, pinhole-free coverage. Such layers must preserve selective contact behavior while minimizing local recombination sites. Encouragingly, several

View Article Online
DOI: 10.1039/D5SC10164F

approaches have already demonstrated both large-area scalability and long-term operational stability, suggesting that these emerging design principles can directly inform device architectures that are not only highly efficient at the laboratory scale but also viable for industrial manufacturing.

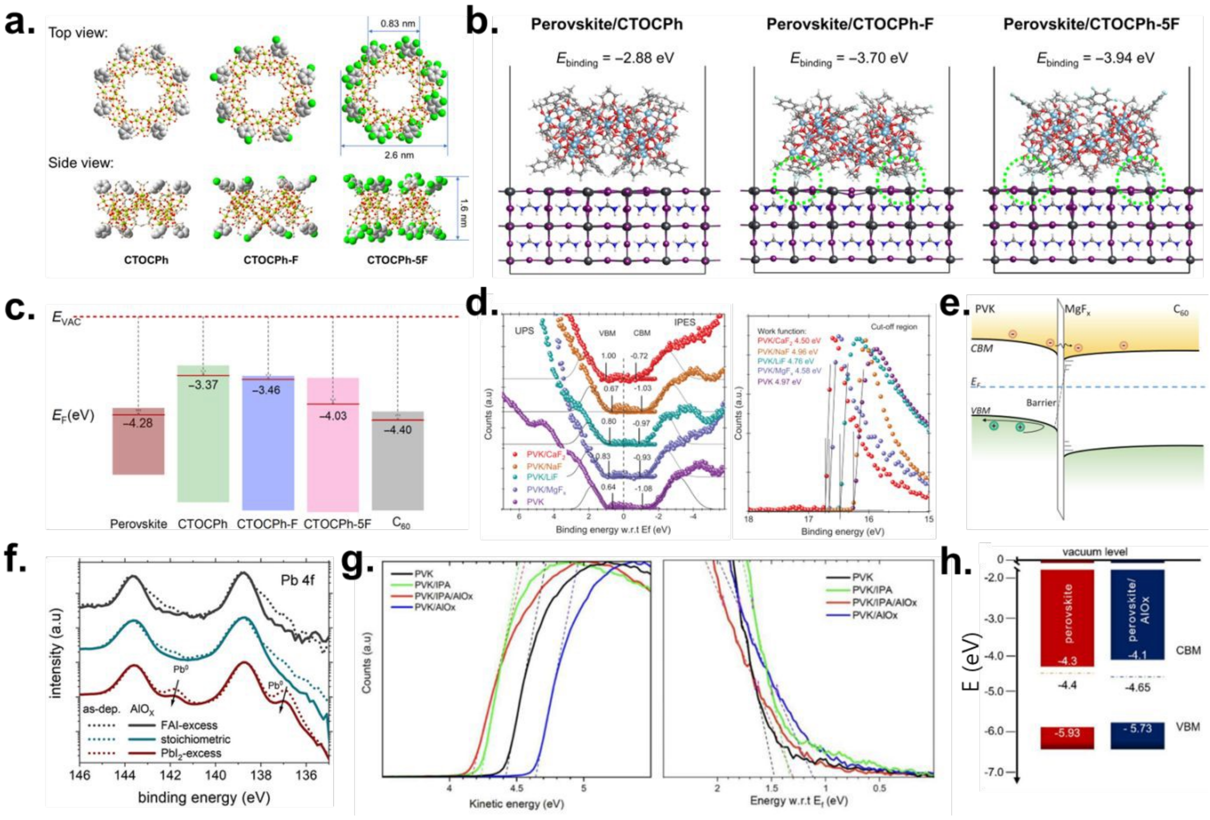

Fig. 5 (a) Top- and side-view atomic structures of the TiO_2 cluster derivatives. (b) Calculated binding energy for PbI_2-rich $FAPbI_3$ (100)/CTOCPh, CTOCPh-F and CTOCPh-5F (c) Energy-level alignment at the perovskite/cluster/C_{60} interface. Reproduced under the terms of the CC-BY Creative Commons Attribution 4.0 International license (https://creativecommons.org/licenses/by/4.0) from Ref.[27]. Copyright 2024, American Association for the Advancement of Science. (d) UPS/IPES analysis of energy-level alignment with different alkali/alkaline-earth fluorides. (e) Schematic of band diagram. Reproduced with permission from Ref.[124]. Copyright 2022, American Association for the Advancement of Science. (f) XPS Pb 4f spectra of perovskite films with different surface stoichiometries before and after AlO_X deposition. (g) UPS spectra near the secondary electron-cutoff (left) and near the WF (right). (h) Schematic of band diagram. Reproduced under the terms of the CC-BY Creative Commons Attribution 4.0 International license

View Article Online
DOI: 10.1039/D5SC10164F

(https://creativecommons.org/licenses/by/4.0) from Ref.[125]. Copyright 2024, Wiley-VCH GmbH.

3.1.3. Low dimensional perovskite (LDP) capping layers

Before discussing specific examples, it is important to distinguish between conventional organic/inorganic interlayers and LDP capping layers. Conventional interlayers are generally introduced as electronically functional modifiers that tune interfacial energetics or suppress recombination without fundamentally altering the crystal lattice of the underlying perovskite. In contrast, LDP capping layers involve structural reconstruction of the surface into reduced-dimensional perovskite phases through the incorporation of bulky organic cations. Although both strategies aim to enhance device stability and optimize interfacial charge transfer, their dominant mechanisms differ. Interlayers primarily operate through dipole-induced band bending and defect passivation via chemical coordination, whereas LDP capping layers additionally provide structural stabilization through lattice reorganization and hydrophobic surface protection. Recent advances increasingly blur this distinction, as multifunctional molecular designs now integrate physical blocking, chemical bonding, and band-structure modulation within a single engineered layer.

Surface defect sites, such as vacancies and under-coordinated Pb^{2+}, readily adsorb and activate O_2 and H_2O molecules[17, 126] The resulting hydration distorts the $(PbI_6)^{4-}$ octahedral framework, weakens the interactions between the A-site cations and the inorganic lattice, and ultimately increases susceptibility to extrinsic species such as moisture, oxygen, and other ambient gases.[127-128] LDP capping layers are most commonly formed using ammonium ligand salts—alkylammonium chains, aromatic ammonium ions, or amidinium cations paired with halides (**Fig. 6a**).[129] These ammonium species bind to the perovskite surface either by filling A-site vacancies or through hydrogen bonding. When the ammonium cation is sufficiently bulky, exceeding the geometrical tolerance factor ($t=(R_A+R_X)/\sqrt{2}(R_B+R_X)$), where $R_{A,}$ R_B, R_X are

View Article Online
DOI: 10.1039/D5SC10164F

the ionic radii of A, B and X site ions, respectively) threshold of 1, it can substitute A-site cations at the surface and drive a structural reconstruction from the 3D perovskite into low-dimensional phases. These include 2D perovskites—formed by slicing the 3D lattice into layered inorganic slabs (*n*)—as well as 1D perovskites consisting of octahedral chains encapsulated by bulky organics, and 0D structures composed of isolated Pb–halide octahedra with strong exciton confinement and large bandgaps.[130-135]

In general, LDP capping layers enhance PeSC stability through three major mechanisms: (1) higher formation energy, which thermodynamically favors crystalline retention over decomposition; (2) hydrophobic organic spacer layers, which block moisture ingress and suppress ion migration; (3) improved charge transfer and interfacial energetics, arising from reduced defect density and well-defined surface chemistry. When bulky organic cations such as phenylethyl ammonium (PEA^+) intercalate between $[PbI_6]^-$ layers, strong van der Waals interactions between the organic spacers, the phenyl rings enhance van der Waals/π–π interactions, strengthening interlayer cohesion and overall formation energy (**Fig. 6b**),[136] yielding a more robust and decomposition-resistant structure. DFT simulations (**Fig. 6c**) further show that lower-*n* 2D perovskites exhibit markedly longer decomposition lifetimes, consistent with enhanced thermodynamic stability. Additionally, the hydrophobic nature of the organic spacer serves as an effective barrier against moisture. The water contact angle of pristine perovskite films (51.8°) increased to 77.2° and 74.4° following 4-hydroxyphenethylammonium iodide (HO-PEAI) and thiopheneethylammonium iodide (2-TEAI) treatments, respectively (**Fig. 6d**).[137] This improvement reflects reduced water affinity and enhanced humidity resistance, underscoring the protective role of LDP layers in mitigating moisture-induced degradation.

View Article Online
DOI: 10.1039/D5SC10164F

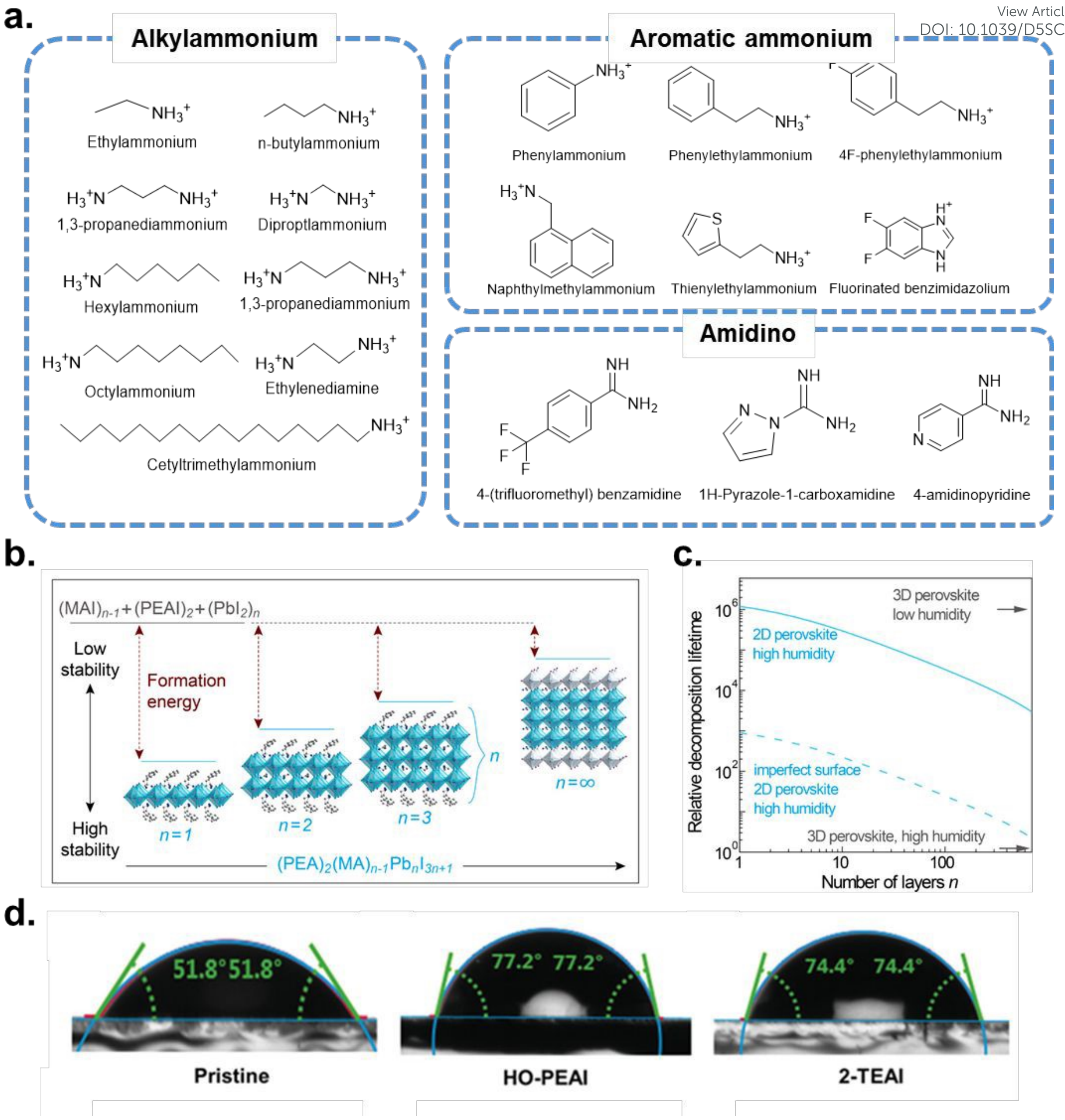

Fig. 6 (a) Chemical structures of organic ligands to build LDP capping layers. (b) Energetics of perovskite formation and stability. Unit cell structure of $(PEA)_2(MA)_{n-1}Pb_nI_{3n+1}$ perovskites with different n values, showing the evolution of dimensionality from 2D (n = 1) to 3D (n = ∞). (c) DFT simulation of the formation energy of perovskite with different n values in different atmospheres. Reproduced with permission from Ref.[136]. Copyright 2016, American Chemical Society. (d) Measurements of water contact angles after dropping water on the perovskite thin film surfaces without and with HO-PEA and 2-TEAI. Reproduced under the terms of the CC-BY Creative Commons Attribution 4.0 International license (https://creativecommons.org/licenses/by/4.0) from Ref.[137]. Copyright 2022, Wiley-VCH GmbH.

View Article Online
DOI: 10.1039/D5SC10164F

Although LDPs provide excellent moisture-resistant capping layers, their integration into inverted device structures is limited by unfavorable energy-level alignment. Due to quantum confinement, LDPs typically retain a similar valence band position while shifting the CBM upward relative to the underlying 3D perovskite **(Fig. 7a)**,[138] hindering electron extraction in inverted devices with reduced J_{SC} and FF. Thus, significant efforts have been devoted to enabling stable LDP capping layers in inverted PeSCs without compromising charge extraction.

To address both interfacial recombination and band offset mismatches between 3D and 2D perovskites, Zang et al. introduced a dipole-active molecular interlayer, 4-methoxyphenylphosphonic acid (MPA), between the 3D perovskite and the top 2D layer (**Fig. 7b**).[139] This layer simultaneously passivates surface defects and tunes the interfacial energetics to facilitate efficient electron extraction. MPA coordinates strongly with under-coordinated Pb^{2+} through Pb–O–P interactions, effectively suppressing trap states. XPS analysis confirms higher-binding-energy Pb 4f components after MPA treatment, consistent with the formation of Pb–O–P bonds (**Fig. 7c**). In addition, the dipole introduced by MPA shifts the Fermi level of the 3D perovskite from 4.55 to 4.22 eV, improving its alignment with the adjacent 2D layer (**Fig. 7d**). The resulting 3D/MPA/2D/ $PC_{61}BM$ stack exhibits significantly enhanced electron transport, yielding a PCE of 24.85% (ITO/MeO-2PACz/$Cs_{0.05}(MA_{0.10}FA_{0.90})_{0.95}Pb(I_{0.90}Br_{0.10})_3$/MPA/2D perovskite/ $PC_{61}BM$ /BCP/Ag).

Zhang et al. further developed an effective interfacial strategy by forming LDP capping layers using 1-ethyl-3-methylimidazolium iodide (EMIMI), 1-vinyl-3-methylimidazolium iodide (VMIMI), and benzylimidazolium iodide (BzMIM) (**Fig. 7e**).[140] The resulting crystals exhibit 1D structures composed of face-sharing polymeric $[PbI_3]^-$ chains surrounded by organic cations. DFT calculations (**Fig. 7f**) reveal that in $BzMIMPbI_3$, the valence band originates from the aromatic cation while the conduction band derives from hybridized orbitals of the inorganic chains. This intrinsic spatial separation suppresses electron–hole recombination and extends carrier lifetimes. Moreover, the ultrathin nature of the 1D layer allows tunneling-assisted electron extraction into C_{60}. Devices incorporating $BzMIMPbI_3$ achieved 24.09% PCE, a high V_{OC} of 1.204 V, and >84% FF, while also demonstrating exceptional thermal (92% retention after 1,400 h at 85 °C) and operational stability (95% retention after 1,008 h under MPP tracking).

Li et al. introduced fluoroalkylamine-based surface molecules (1FPD, 2FPD) (**Fig. 7g**) to improve charge transport in 2D/3D bilayer PeSCs.[141] While 1FPD offered modest passivation, 2FPD induced a well-oriented ferroelectric 2D layer with strong out-of-plane dipoles due to fluorination, leading to a favorable WF shift (4.47 eV → 4.34 eV) and improved band alignment (**Fig. 7h**). Zhao et al. used 5-(2-hydroxyethyl)-3,4-dimethylthiazolium iodide (HDI) to form a 1D capping layer that converts surface impurities (PbI_2, δ-$FAPbI_3$) into a uniform 1D $HDPbI_3$ phase.[142] This induces an n-type-like surface, optimizes band alignment, and enhances electron extraction, enabling a PCE of 25.30% with an FF of 84.21%. Wang et al. replaced the piperazinium iodide (PI) capping layer with morpholine hydriodide (MORI) and thiomorpholine hydriodide (SMORI) to construct a 2D/3D heterostructured capping layer (**Fig. 7i**).[143] SMORI, in particular, provides stronger defect passivation and forms a more favorable n–N homotype (i.e., an n-type/n-type junction with different doping levels) 2D/3D junction. This shifts the surface further n-type, aligning more effectively with the C_{60} ETL and reducing interfacial recombination. Achieving their seamless integration without efficiency losses would enable devices that combine high performance with exceptional stability.

In summary, LDP capping layers demonstrate that stability and interfacial quality can be co-optimized when surface reconstruction, defect passivation, and moisture resistance are engineered as an integrated interfacial system. The primary trade-off is that quantum confinement in LDPs often raises the CBM relative to that of the 3D absorber, which can impede electron extraction in inverted devices, thereby reducing the J_{SC} and FF. This interfacial trade-off can be deliberately re-tuned using dipole-active interlayers, ultrathin 1D phases that

View Article Online
DOI: 10.1039/D5SC10164F

permit tunneling, or junction designs that render the surface more n-type. However, even with these strategies, several practical challenges remain. Nonuniform surface conversion may leave portions of the reactive 3D phase partially exposed, undermining the intended protective function. In addition, excessively thick or poorly oriented capping layers can act as resistive barriers that hinder charge extraction. Furthermore, under prolonged heat and illumination, the interface may evolve over time. Dipole relaxation and ionic redistribution can gradually reintroduce band-offset mismatches and nonradiative recombination pathways, even when the as-fabricated device initially exhibits excellent performance.

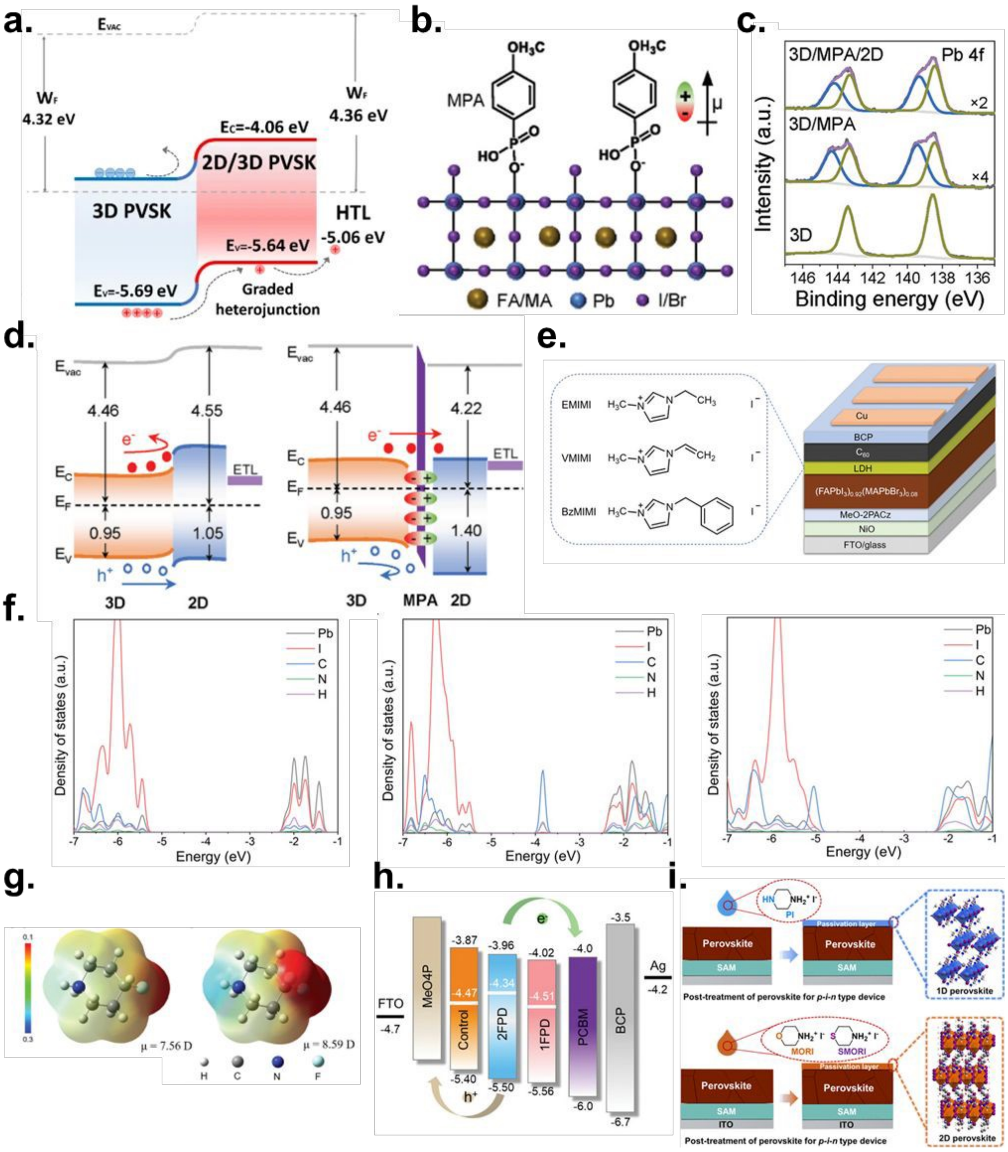

View Article Online
DOI: 10.1039/D5SC10164F

Fig. 7 (a) Energy level diagram of 3D/2D perovskite bilayer. Reproduced with permission from Ref.[138]. Copyright 2024, Springer Nature. (b) Schematic of interaction between MPA and 3D perovskite, and representative of surface dipole moment. (c) XPS Pb 4f core level spectra of 3D, 3D/MPA, 3D/MPA/2D films. (d) Energy level diagrams of 3D/2D and 3D/MPA/2D perovskite heterointerfaces. Reproduced with permission from Ref.[139]. Copyright 2023, Wiley-VCH GmbH. (e) Chemical structures of the imidazolium salts and architecture of the inverted PeSCs. (f) Projected density of states of the 1D perovskites ($EMIMPbI_3$, $VMIMPbI_3$, $BzMIMPbI_3$). Reproduced with permission from Ref.[140]. Copyright 2022, Wiley-VCH GmbH. (g) ESP maps and electric dipole moment (μ) of 1FPD and 2FPD molecule. (h) Structure and energy level alignment of the inverted PeSCs. Reproduced with permission from Ref.[141]. Copyright 2024, Wiley-VCH GmbH. (i) Schematic Illustration of the post-treatment for the perovskite film using PI, MORI, or SMORI and single-crystal structure based on PI and MORI. Reproduced with permission from Ref.[143]. Copyright 2024, American Chemical Society.

3.1.4. Heat dissipation layers

Heat generation in solar cells is unavoidable, originating from both solar irradiation and device operation. Establishing rapid heat-removal pathways is thus essential for suppressing thermally driven degradation—such as ion migration, phase segregation, and interfacial reactions. Because perovskites possess intrinsically low thermal conductivity and mechanically soft lattices, targeted thermal-management strategies will be crucial for extending device lifetime under realistic operating conditions. Given the intrinsically low thermal conductivity of perovskites, substantial efforts have focused on improving heat transport within the absorber. Two primary strategies have emerged: (1) incorporating high–thermal-conductivity materials into the perovskite bulk, and (2) enhancing thermal conduction at the perovskite surface to accelerate vertical heat flow.

A widely adopted approach is integrating high thermal conductivity materials directly into the perovskite matrix. Two-dimensional materials have received particular attention due to their exceptional thermal conductivity and chemical stability. Liu et al. incorporated molecularly functionalized boron nitride (BN-5) nanosheets into the perovskite as local heat-dissipation pathways (**Fig. 8a**).[144] BN exhibits an in-plane thermal conductivity of ~550 W m^{-1} K^{-1}, and its incorporation increased the thermal conductivity of the perovskite by 30.7%. Consistent with this, real-time IR thermography confirmed enhanced heat dissipation: BN-5 films cooled more rapidly from 85 °C to ambient (20 °C) than pristine films (**Fig. 8b**), and under 30 min of 100 mA cm^{-2} illumination, the temperature rise (ΔT) was significantly lower (21.7 °C vs. 34.6 °C) (**Fig. 8c**). Beyond thermal benefits, BN-5 interacts with under-coordinated Pb^{2+} at grain boundaries, enabling a high PCE of 25.36% (ITO/2PACz/$Cs_{0.05}FA_{0.81}MA_{0.14}PbI_{2.55}Br_{0.45}$/$PC_{61}BM$ /BCP/Cu). Device stability also improved markedly: under 1-sun illumination at 85 °C, the BN-5 device retained over 95% of its initial PCE after 2,640 h, whereas the pristine device dropped to 63% within 587 h.

Wan et al. applied a similar strategy by introducing $Ti_3C_2T_X$ MXene nanosheets (**Fig. 8d**).[145] With a thermal conductivity of up to 55.8 W m^{-1} K^{-1}, MXene increased the thermal conductivity of the perovskite to 0.413 W m^{-1} K^{-1}. Under ISOS-T-1 conditions (85 °C, 30 ± 5% RH), MXene-modified devices showed no degradation after 1,000 h, while control devices degraded severely (**Fig. 8e**). Even under continuous aging, MXene devices preserved 80% of their PCE after 500 h, whereas control devices retained only 58% after 200 h.

A complementary strategy intensifies heat extraction at the perovskite surface. By increasing the thermal conductivity at the top interface, a steeper vertical temperature gradient is created, thereby accelerating heat flux according to Fourier's law ($Q = -\kappa \nabla T$, where Q represents heat flux, κ represents thermal conductivity, and ∇T represents temperature gradient). Choi et al. implemented this concept using a hybrid interfacial scaffold composed of Al_2O_3 nanoparticles (NPs) embedded in the polymeric hole-transporting material (HTM) asy-PBTBDT (Al_2O_3@asy-PBTBDT) (**Fig. 8f**).[146] Due to their high thermal conductivity (20–30 W m^{-1} K^{-1}), Al_2O_3 NPs formed efficient heat-dissipation channels. Time-domain thermoreflectance (TDTR) measurements revealed that even 0.1 wt% Al_2O_3 increased the through-plane thermal conductivity of the HTM from 0.123 to 0.206 W m^{-1} K^{-1}. Cooling tests confirmed significantly faster temperature decay for Al_2O_3-containing HTM layers (**Fig. 8g**). Under harsh conditions (85 °C and 85% RH, no encapsulation), devices with Al_2O_3@asy-PBTBDT retained 91% of their initial PCE after 31 days—substantially outperforming pristine HTM devices and even encapsulated Spiro-OMeTAD controls. Although the added Al_2O_3 slightly reduced hole mobility and J_{SC}, devices still achieved high V_{OC} (1.16 V) and 19.9% PCE (FTO/SnO_2/ $(FA_{0.833}MA_{0.167})Pb(I_{2.5}Br_{0.5})$/$Al_2O_3$@asy-PBTBDT/Au). Notably, the strategy was broadly compatible with various HTMs.

A third heat-management mechanism was demonstrated by Park et al., who introduced an *n*-doped fullerene interlayer ($PC_{61}B$-TEG) between the perovskite and C_{60} ETL.[147] Doping with 4-(1,3-dimethyl-2,3-dihydro-1*H*-benzimidazol-2-yl)-*N*,*N*-dimethylaniline (*N*-DMBI) increased free-carrier density, enhancing both electrical and thermal conductivity through carrier-assisted heat transport—analogous to metallic systems. TDTR measurements showed a 25% increase in thermal conductivity upon doping (**Fig. 8h**). Cooling analysis confirmed faster heat dissipation: the doped film cooled to 30 °C in 80 s, compared to ~120 s for the undoped film (**Fig. 8i**). In addition, *n*-doping shifted the Fermi level upward, improving alignment between $PC_{61}B$-TEG and the perovskite CBM, leading to more efficient electron extraction, reduced interfacial recombination, and a larger QFLS. Devices achieved 24.42% PCE (ITO/MeO-4PACz/$FA_{0.85}Cs_{0.15}PbI_3$/$PC_{61}B$-TEG/C_{60}/BCP/Ag) and retained 90% of their initial efficiency over 2,400 h at 85 °C. This approach highlights the dual role of conductive interlayers in enhancing both thermal transport and interfacial energetics.

Unlike heat transfer by conduction through the device stack, a significant fraction of heat is dissipated from the device surface to the air via convection and thermal radiation. Yu et al. designed a triple-layer full-carbon electrode (F-CE) in which the top dense carbon layer is intentionally used as a high emissivity radiative-cooling layer.[148] The triple-layer F-CE exhibited near black-body-like emission, as quantified by its emissivity ($\varepsilon \approx 0.99$), exceeding Au (0.54) and ITO (0.62). As a result, the F-CE can function as an efficient thermal radiator while

View Article Online
DOI: 10.1039/D5SC10164F

maintaining electrode functionality. F-CE reduced the device surface temperature by ~10 °C compared with Au, indicating more efficient heat dissipation (**Fig. 8j**).

Recent research trends are increasingly focused on combining multiple thermal-management strategies, including enhanced heat transport within the bulk and across interfaces together with radiative cooling at the device surface. Such integrated approaches can lower the peak operating temperature while simultaneously controlling temperature gradients to facilitate efficient heat dissipation. Under real outdoor operation, however, transient irradiance, wind-dependent convective cooling, partial shading or soiling, and day–night thermal cycling can induce hot-spot formation, localized current crowding, and steep temperature gradients. These effects collectively accelerate ion migration, phase segregation, and interfacial reactions. Therefore, we emphasize that future outdoor-relevant designs should integrate enhanced heat conduction in the bulk and upper interfaces with high-emissivity top-surface concepts, thereby linking thermal management directly to improved long-term operational stability.

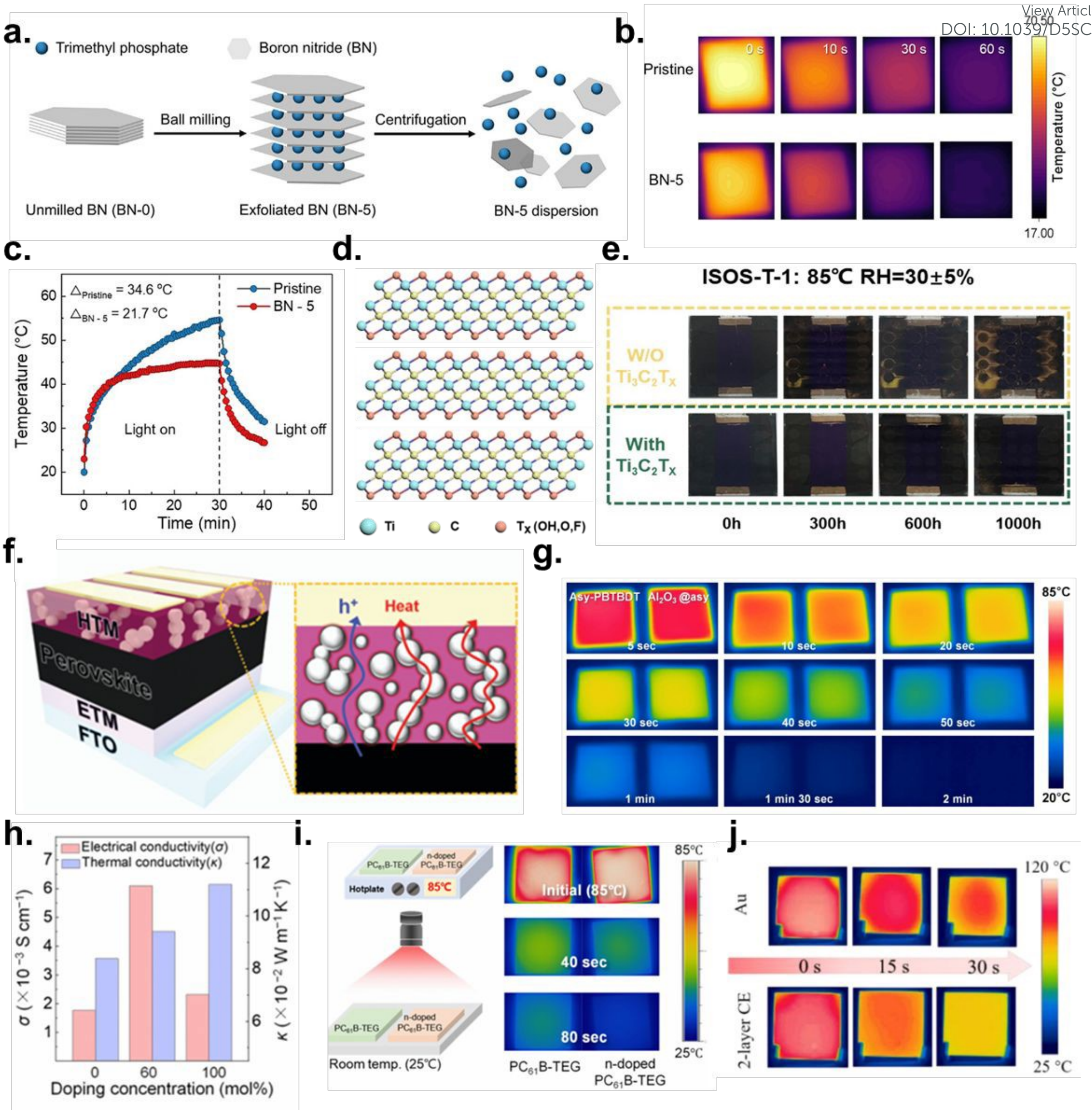

Fig. 8 (a) Schematic illustration of the preparation process for BN-5. (b) Comparison of the cooling process between pristine perovskite film and BN-5 based perovskite films, illustrated through infrared (IR) thermal images. (c) Temperature profile of PeSCs under solar irradiation and after the light is turned off. Reproduced with permission from Ref.[144]. Copyright 2025, Wiley-VCH GmbH. (d) Schematic diagram of the multilayer $Ti_3C_2T_X$. (e) Image of PeSCs aging evolution under ISOS-T-1 conditions. Reproduced under the terms of the CC-BY Creative Commons Attribution 4.0 International license (https://creativecommons.org/licenses/by/4.0) from Ref.[145]. Copyright 2025, Springer Nature. (f) Schematic illustration of the PeSC using Al_2O_3 NPs as thermally conductive materials. (g) IR thermal images of polymeric HTM (Asy-PBTBDT) and Al_2O_3@asy-PBTBDT under a plate-cooling test. All samples were prepared on the perovskite layer. Reproduced with permission

View Article Online
DOI: 10.1039/D5SC10164F

from Ref.[146]. Copyright 2020, Royal Society of Chemistry. (h) Electrical and thermal conductivity of $PC_{61}B$-TEG by varying N-DMBI doping concentration. (i) IR camera image of $PC_{61}B$-TEG and n-doped $PC_{61}B$-TEG. Reproduced with permission from Ref.[147]. Copyright 2024, Royal Society of Chemistry. (j) IR camera–measured temperature of glass substrates coated with various electrode films. Reproduced under the terms of the CC-BY Creative Commons Attribution 4.0 International license (https://creativecommons.org/licenses/by/4.0) from Ref.[148]. Copyright 2024, Springer Nature.

3.2. C_{60}-alternative ETLs

This section organizes organic ETL strategies that replace or complement C_{60}, focusing on the physicochemical mechanisms operating at the top perovskite/ETL interface. These mechanisms can be broadly grouped into four functional axes. First, molecular dipoles modulate the electron-extraction barrier by shifting the vacuum level and inducing favorable band bending, while simultaneously blocking holes. Second, defect-control functionalities passivate Pb/Sn, halide, and A-site defects through Lewis acid–base interactions, hydrogen bonding, or ionic coordination, thereby reducing nonradiative recombination and mitigating hysteresis. Third, ion-management mechanisms limit halide and A-site ion migration and prevent interfacial charge accumulation through fixed charges, electrostatic interactions, or ion-blocking barriers. Fourth, morphology and processing control ensures complete coverage, stable packing, and thermal/photostability—achieved through aggregation suppression, surface-energy tuning, and steric or hydrophobic design—which expands the thickness tolerance and improves large-area process reproducibility. Based on these mechanistic axes, we categorize organic ETLs into (i) fullerene derivatives and (ii) non-fullerene (NF) derivatives.

3.2.1. Fullerene-derivative ETLs

In fullerene derivatives, the four mechanisms manifest through four corresponding molecular-design strategies. (1) Hybrid design couples electron-accepting fragments—such as perylene diimide (PDI), naphthalene diimide (NDI), or non-fullerene acceptor (NFA) units—

to integrate transport, passivation, and morphology control within a single molecular framework, thereby widening the ETL thickness tolerance. (2) Deposition-compatible design employs thermally robust substituents and polar centers to maintain amorphous, low-roughness films after evaporation while simultaneously passivating cation/anion vacancies at the perovskite surface, reducing line-to-line process variability and contact-resistance drift. (3) Ionic fullerene design introduces fixed charges that neutralize defects, suppress ion migration, and strengthen interfacial adhesion, improving device reliability under long-term MPPT operation or combined thermal/humidity stress. (4) Terminal-group engineering combines electron-withdrawing/donating groups, Lewis-basic motifs, halogen/ionic substitution, and steric/hydrophobic elements to co-optimize LUMO alignment, molecular packing, and electron mobility.

Electron-accepting fragments (e.g., PDI, NDI, NFA derivatives) are covalently coupled or grafted onto the fullerene cage to unify three functions in one molecule: (1) the C_{60} core provides a continuous electron-transport pathway, (2) imide/NFA functionalities passivate interfacial defects, and (3) the auxiliary fragments tune morphology through π–π interactions and surface-energy control. Carbonyl, nitrile, and halogen groups selectively coordinate with Pb/Sn-centered defects, lowering surface trap density and suppressing interfacial charge buildup. Simultaneously, the auxiliary π-framework promotes face-on orientation and smooth coverage, straightening the electron-extraction pathway and enabling excellent thickness tolerance.

Sun et al. demonstrated this strategy using an NFA fragment grafted onto C_{60} (**Fig. 9a**).[149] Molecular design favored C_{60}–NFA and NFA–NFA interactions, yielding low surface roughness and pinhole suppression under solution processing (**Fig. 9b**). Electron-withdrawing terminal groups on the NFA selectively interacted with Pb/I defects, reducing trap density, while the C_{60} cage ensured efficient transport. As a result, interfacial charge accumulation and ion migration were mitigated, reducing V_{OC} and FF losses and drastically softening the thickness roll-off across several hundred nanometers—significantly improving compatibility with slot-die and blade coating. Using the device stack ITO/SAM/perovskite ($Cs_{0.05}(FA_{0.98}MA_{0.02})_{0.95}Pb(I_{0.98}Br_{0.02})_3$)/ETL/BCP/Ag, high efficiency was maintained even at large perovskite thicknesses, demonstrating remarkable process tolerance **(Fig. 9c)**. Consistent with this mechanism, C_{60}–NFA hybrids such as $BTPC_{60}$ retained ~90% of their initial efficiency after 1,500 h under ISOS-D-2 (85 °C, N_2), representing a major thermal-stability improvement over pristine C_{60}.

Fullerene derivatives can also be engineered to maintain smooth amorphous morphology after vacuum deposition, ensuring stable band bending and contact resistance during metal electrode evaporation. Thermally robust substituents preserve film uniformity, while polar groups enable complementary passivation of halide and A-site defects. This enhances compatibility with tandem top cells and encapsulation and reduces variability in large-area vacuum fabrication. Shui et al. developed a thermally evaporable fullerene derivative to address process variability and interfacial instability in tandem stacks (**Fig. 9d**).[150] Indanone substitution and bulky *tert*-butyl side chains were designed to preserve an amorphous, low-roughness morphology after evaporation. Consistently, grazing incidence X-ray diffraction (GIXRD) shows that *t*-Bu-FIDO films remain essentially amorphous before and after annealing at 150 °C, indicating suppressed thermally induced crystallization/aggregation (**Fig. 9e**). In addition, Pb 4f XPS spectra for perovskite/*t*-Bu-FIDO exhibits a clear shift toward lower binding energy, consistent with carbonyl–Pb^{2+} coordination and surface defect passivation, which correlates with reduced nonradiative recombination and mitigated hysteresis (**Fig. 9f**). Using the configuration ITO/NiOx/SAM/perovskite ($Cs_{0.04}(FA_{0.95}MA_{0.05})_{0.96}Pb(I_{0.95}Br_{0.05})_3$)/ETL/BCP/Ag, concurrent improvements in V_{OC} and FF translated directly into higher PCE. Compared with solution-processed ETLs, this approach eliminated leakage pathways and thickness nonuniformity, improving line-to-line reproducibility during vacuum processing and offering high compatibility with encapsulation and tandem integration.

In the ionic fullerene strategy, fullerene cores are functionalized with fixed-charge headgroups (e.g., quaternary ammonium, imidazolium) and counter-anions to introduce electrostatic binding and interfacial electron-shuttling. The fixed charges directly neutralize halide vacancy and A-site–derived defects, suppress ion migration, and thereby reduce nonradiative recombination and hysteresis. At the same time, ionic interactions enhance molecular packing and interfacial adhesion, improving fracture toughness and sustaining module-scale reliability under prolonged MPPT operation and combined thermal/illumination stress.

You et al. implemented this strategy by attaching cationic headgroups to C_{60} to form ionic fullerene salts **(Fig. 9g)**.[151] The positively charged termini (e.g., $–NH_3^+$) formed strong ionic bonds with surface I^- species, selectively neutralizing defect populations and suppressing charge accumulation and ion migration (**Fig. 9h**). Strengthened intermolecular and interfacial adhesion increased fracture toughness, enabling stable electron extraction with minimal degradation during extended MPPT and thermo-photonic stress. In particular, double-cantilever beam testing showed that the interfacial fracture energy (G_C) at the ETL interface increased from 0.50 ± 0.07 J m^{-2} for C_{60} to 1.43 ± 0.03 J m^{-2} for CPMAC, quantitatively confirming the enhanced interfacial mechanical stability (**Fig. 9i**). This electro–chemo–mechanical synergy also mitigated the instability of thin ETLs, stabilized top-electrode deposition, and reduced performance dispersion in large-area blade-coated mini-modules. Using the architecture FTO/SAM/$Cs_{0.04}MA_{0.14}FA_{0.82}Pb(I_{0.987}Br_{0.013})_3$/ETL/ALD-$SnO_X$/Ag, replacing C_{60} with an ionic fullerene yielded PCE ≈ 26%, illustrating that improved contact and energy alignment directly translate into higher efficiency. Stability was likewise enhanced: encapsulated p-*i*-n mini-modules operated for 2,200 h at ~55 °C under 1-sun MPP retained 91.5% of the initial

PCE, outperforming C_{60}-based counterparts that exhibited far greater degradation under identical conditions.

In the case of terminal-group engineering, using a common fullerene core (e.g., methanofullerene, fulleropyrrolidine), terminal substituents are systematically varied to co-optimize LUMO alignment, molecular packing, and electron mobility. Combinations of electron-donating/withdrawing groups, Lewis-basic motifs (pyridyl, carboxylate, phosphonate), halogen/ionic substitutions, and steric/hydrophobic elements determine dipole moment, packing density, surface energy, and defect passivation capability. Dipole-rich or sterically tailored terminal promote dense packing and uniform film coverage, suppressing pinholes and shunt pathways, while precise energy-level tuning minimizes V_{OC} loss by aligning the LUMO with the perovskite CBM. Modifying solubility and drying kinetics further improves coating reproducibility and thickness tolerance, enabling compatibility with large-area printing and with low-bandgap absorbers such as Sn–Pb alloys.

Liu et al. formalized this "terminal effect" by screening multiple terminal groups on an identical fulleropyrrolidine scaffold (**Fig. 9j**).[152] Donor–acceptor strength governed LUMO alignment with the perovskite CBM, reducing V_{OC} deficit, whereas Lewis-basic termini selectively coordinated with Pb^{2+} and I^{-} defects, suppressing nonradiative recombination. Cyclic voltammetry (CV) confirmed reversible redox behavior for all six fullerene derivatives (**Fig. 9k**), while shifts in the first reduction potential correlated with terminal-group electron-donating strength and steric profile, yielding LUMO levels well aligned to the perovskite CBM. Bulky and hydrophobic terminal groups increase the stacking density by balancing steric hindrance and hydrophobic aggregation, which helps sustain a continuous electron-transport pathway and enhances electron mobility (**Fig. 9l**). Using the device structure ITO/NiOx/perovskite ($Cs_{0.05}(FA_{0.95}MA_{0.05})_{0.95}Pb(I_{0.95}Br_{0.05})_3$)/ETL/BCP/Ag, the optimized CN-TPACl terminal design achieved ≈25% steady-state PCE (certified 25.18%). Durability was similarly enhanced: CN-TPACl-based ETLs retained ≈90% of their initial PCE after 1,000

View Article Online
DOI: 10.1039/D5SC10164F

h of unencapsulated operation under white LED in N_2, ≈89% after 200 h at 85 °C (N_2), and ≈86–88% after 10 cycles of encapsulated light/dark cycling in air, confirming robust long-term operation. These results enable a design guideline for matching terminal groups to specific perovskite compositions and processing routes.

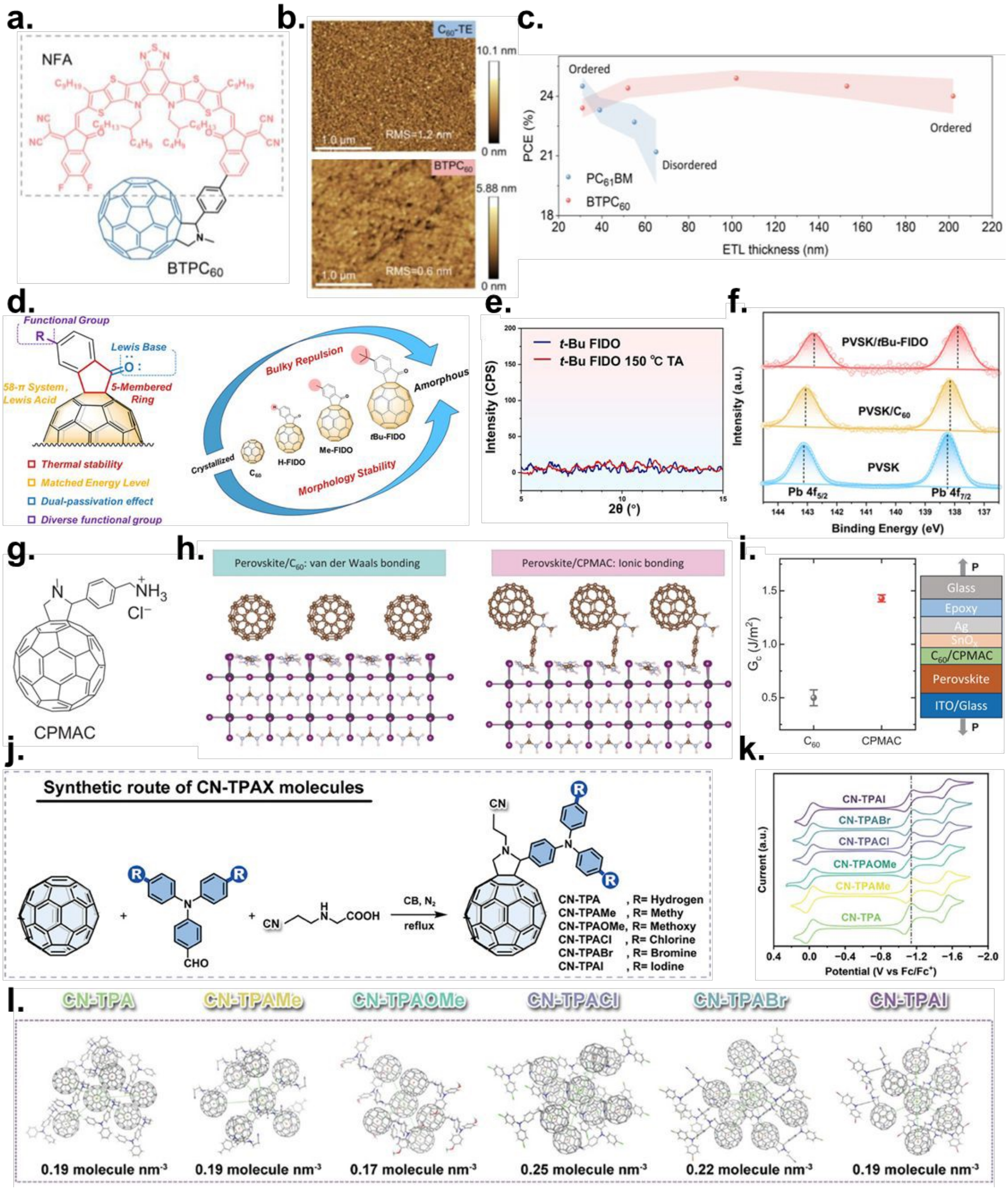

Fig. 9 (a) Chemical structure of $BTPC_{60}$. (b) AFM height images of C_{60}-TE and $BTPC_{60}$ films.

(c) PCE versus ETL thickness for $PC_{61}BM$ and $BTPC_{60}$. Reproduced with permission from Ref.[149]. Copyright 2024, Wiley-VCH GmbH. (d) Schematic of evaporable fullerene derivatives. (e) GIXRD of thermally deposited films before/after 150 °C annealing: C_{60}, H-FIDO, and tBu-FIDO. (f) XPS spectra of the Pb 4f region. Reproduced with permission from Ref.[150]. Copyright 2023, American Chemical Society. (g) Structure of CPMAC. (h) Perovskite/C_{60} (van der Waals) vs perovskite/CPMAC (ionic) interactions. (i) Comparison of G_C of devices to quantify ETL for C_{60} or CPMAC. Reproduced with permission from Ref.[151]. Copyright 2025, American Association for the Advancement of Science. (j) Synthetic route to CN-TPAX (X = H, Me, OMe, Cl, Br, I). (k) CV curves in o-DCB/ACN (5:1 v/v, 0.1 M Bu_4NClO_4, 100 mV s^{-1}; Fc/Fc^+ reference); E_{red1} used to estimate LUMO levels. (l) Representative packing snapshots highlighting cage-to-cage π–π interactions of the six FDs. Reproduced with permission from Ref.[152]. Copyright 2024, Wiley-VCH GmbH.

3.2.2. Non-fullerene ETLs

Fullerene (C_{60}, $PC_{61}BM$)–based ETLs have long served as the benchmark in inverted PeSCs because of their isotropic electron transport and favorable packing characteristics. However, band-tail–induced energetic disorder reduces the QFLS and ultimately lowers V_{OC}, while their intrinsically low polarity and limited surface functional groups restrict interfacial compatibility with polar perovskites and hinder multi-site defect passivation.[153-156] Moreover, photo- and thermal-induced aggregation causes morphological drift at the perovskite/ETL interface, enhancing contact resistance and altering band bending, opening ion-migration pathways, and thereby compromising long-term stability.

In contrast, NF-ETLs integrate multiple interfacial and transport advantages within a single molecular framework. Their π-accepting backbones and induced dipoles enable precise control over vacuum-level shifting and band bending, thereby lowering the electron-extraction barrier. Heteroatoms, terminal groups, and supramolecular binding motifs further provide multi-site defect passivation and enforce directional molecular orientation, collectively suppressing nonradiative recombination and hysteresis. In parallel, side-chain design and polymerization strategies raise the glass-transition temperature (T_g), stabilize the film morphology, and establish continuous electron-transport pathways, which together improve thickness tolerance and enhance reproducibility in slot-die and printing processes.

Through these combined features, NF-ETLs effectively overcome the structural and interfacial limitations inherent to fullerene ETLs, suppressing recombination and ion migration at the top interface, and expanding the process window for large-area and tandem device fabrication. The following section further organizes these advantages into three synergistic design pillars for optimizing NF-ETLs: (1) Interfacial dipole and supramolecular engineering, which modulate vacuum-level shifts, band bending, and extraction kinetics; (2) Polymerization-driven morphological and transport stabilization, which enhance T_g, suppress aggregation, and form continuous electron pathways; and (3) End-group engineering, which simultaneously governs defect passivation, interfacial energetics, and surface hydrophobicity.

Incorporating dipole moments and selective binding motifs into NF-ETLs provides deterministic control over vacuum-level shifts and interfacial band bending. Huang et al. exemplified this strategy by reengineering Y6 into phenanthroline-modified (Y-Phen) and crown-ether–modified (Y-CE) derivatives (**Fig. 10a**).[155] Phenanthroline–Pb^{2+} and crown-ether–formamidinium iodide (FAI) interactions promoted upright orientation, which can attribute to enhanced dipole moments (Y6 ≈1.07 D < Y-Phen ≈2.30 D < Y-CE ≈7.12 D), and strengthened π–π stacking. Stepwise WF shifts were observed (Y6 ≈ −0.05/ Y-Phen ≈−0.12/ Y-CE ≈−0.20 eV), indicating progressively deepened band bending and reduced electron-extraction barriers (**Fig. 10b**).

Polymerizing Y-series NFAs (yielding PY-NFAs) elevates T_g, immobilizes the molecular packing, prevents solution-phase pre-aggregation, and establishes continuous transport pathways with reinforced π–π ordering. Liu et al. designed robust ETL by polymerizing Y-Br monomer with an electron-rich π-bridge (thiophene, Th) and electron-deficient π-bridge (pyrazine, Pz), yielding two polymers, PY-Th and PY-Pz (**Fig. 10c**).[97] Polymerization increased T_g in the order of Y-Br, PY-Th, and PY-Pz, with Y-Br showing the lowest and PY-Pz the highest T_g (**Fig. 10d**). Molecular dynamics simulations revealed that both PY-Th and PY-Pz adopt a similar stacking mode, which is favorable for intermolecular electron transport. However, PY-Pz exhibits much higher planarity than PY-Th (dihedral angle 1.8° vs 11.0°) due to an intramolecular N···H non-covalent interaction between Pz and electron-accepting unit, suggesting an enhanced electron mobility (**Fig. 10e**). In devices (ITO/SAM/$FA_{0.95}Cs_{0.05}PbI_3$/ETL/BCP/Ag), PY-Pz delivered FF > 85% and PCE ≈ 25.8% (EQE-integrated ≈ 24.9%). These results show that polymerization enhances both morphological stability and charge transport, mitigating thickness roll-off and enabling scalable fabrication.

Furthermore, introducing Lewis- and hydrogen-bond–capable terminal groups such as –CN and carbonyl provide a unified strategy to achieve multi-site defect passivation, fine-tuned energetic alignment, and hydrophobic top-contact formation. Feng et al. developed an n-type, BTI-based polymer (PCNI2-BTI, -3.95 eV) whose LUMO level closely matches that of the perovskite (-3.91 eV), thereby minimizing the electron-extraction barrier. (**Fig. 10f**).[33] A distinctive Pb−O interaction between under-coordinated Pb^{2+} ions and carbonyl groups is found at the interface between the perovskite and PBTI2-BTI, with a bond distance of 2.63 Å (**Fig. 10g**). Additionally, Pb−N interaction between the cyano group and Pb^{2+} is also found, indicating a strong interaction for PCNI2-BTI enabled by the cyano functionality. The devices with PCNI2-BTI (ITO/SAM/$Cs_{0.05}FA_{0.9}MA_{0.05}PbI_3$/ETL/BCP/Ag) delivered a superior performance of V_{OC} = 1.179 V, FF = 86.4%, and PCE = 26.0% (certified 25.4%), with excellent batch-to-batch reproducibility (25.6 ± 0.2%, n = 80) in large-area fabrication. Stability tests under ISOS-L-3 (encapsulated, white LED, ≈65 °C) show significantly slower degradation compared with the devices containing $PC_{61}BM$ and PBTI2-BTI, confirming the superior operational durability of CN/carbonyl-terminated systems.

However, from a commercialization standpoint, replacing C_{60} requires more than achieving high PCE and stability; the alternative must also simultaneously satisfy: (i) cost competitiveness,

View Article Online
DOI: 10.1039/D5SC10164F

particularly in light of multi-step synthesis and purification; (ii) kilogram-scale manufacturability with robust batch-to-batch consistency; (iii) compatibility with large-area coating processes (e.g., slot-die or blade coating), including sufficient thickness tolerance and a broad processing window; and (iv) seamless integration with electrode deposition and encapsulation processes. Although NF and polymerized ETLs provide clear advantages in interfacial functionality—such as improved defect passivation, ion migration control, and energy-level alignment—as well as enhanced morphological stability, persistent challenges related to synthetic complexity, purification, reproducibility, and overall cost may constrain their ability to replace C_{60} on a one-to-one basis in the near term. Accordingly, in the short term, hybrid ETL strategies that reduce C_{60} consumption (e.g., ultrathin C_{60} layers combined with low-cost modifiers or interlayers) or employ more process-tolerant derivatives may represent more pragmatic pathways. Over the mid-to-long term, material families featuring simplified synthetic routes and validated scalability in large-area coating processes are likely to emerge as the most viable candidates.

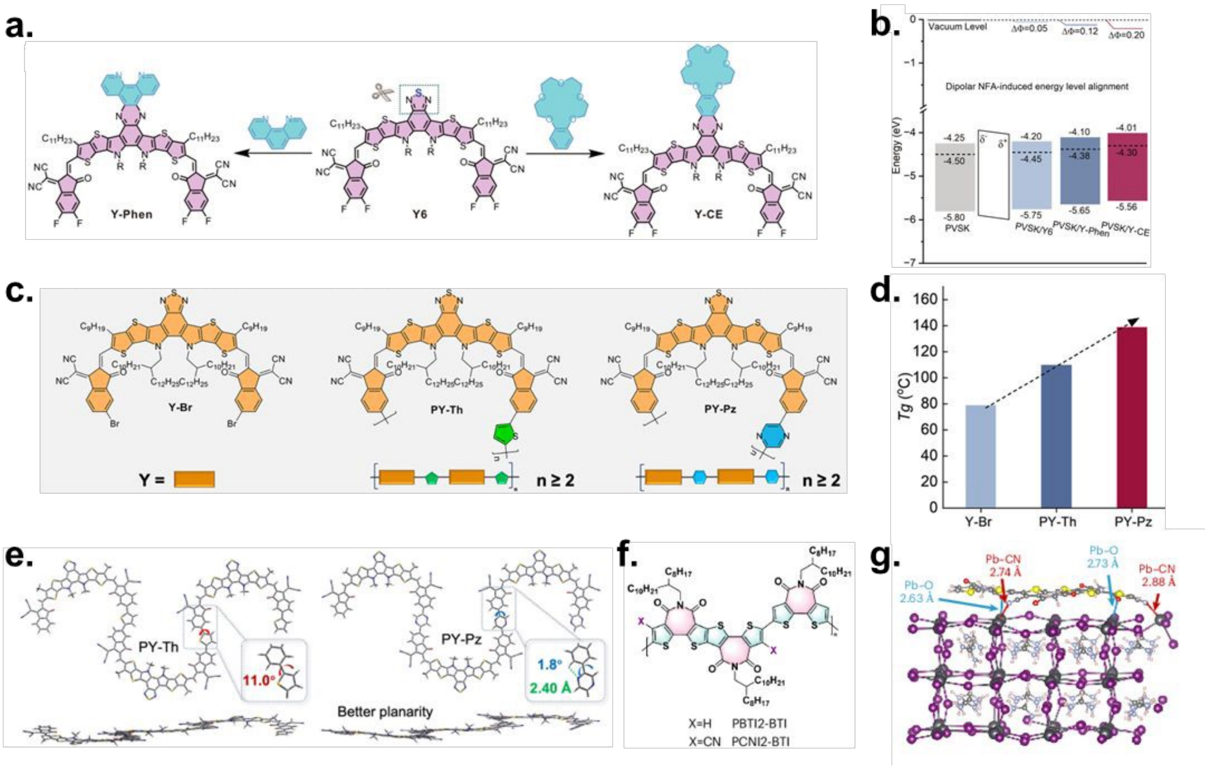

View Article Online
DOI: 10.1039/D5SC10164F

Fig. 10 (a) Molecular structures of Y6 derivatives (Y-Phen, Y-CE). (b) Energy-level/band alignment for NFA-coated perovskite films. Reproduced under the terms of the CC-BY Creative Commons Attribution 4.0 International license (https://creativecommons.org/licenses/by/4.0) from Ref.[155]. Copyright 2025, Springer Nature. (c) Chemical structures of Y-NFA and PY-NFA. (d) T_g of Y-Br, PY-Th, and PY-Pz. (e) DFT-optimized trimer (PY-Th, PY-Pz) structures highlighting planarity. Reproduced with permission from Ref.[97]. Copyright 2025, Elsevier Ltd. (f) Chemical structures of the PBTI2-BTI and PCNI2-BTI. (g) Simulation of coordination effect between PCNI2-BTI and Pb^{2+} ion. Reproduced with permission from Ref.[33]. Copyright 2025, Springer Nature.

3.3. ETL/cathode interlayer

In inverted PeSCs, the selection of the cathode metal critically influences electron extraction, interfacial stability, and overall device engineering flexibility. The most commonly used cathode metals are Ag, Cu and Al. Among these, Ag is the predominant choice in high-performance inverted PeSCs because its WF (typically –4.2 to –4.6 eV) aligns well with the LUMO levels of fullerene-based ETLs (–4.0 eV for C_{60} and –3.8 eV for $PC_{61}BM$), ensuring a small energy offset and efficient electron collection.[157-158] Ag also offers high electrical conductivity, excellent film-forming characteristics, moderate cost relative to Au, and comparatively inert chemical behavior. Cu, with a nominal WF of –4.4 to –4.7 eV, presents a cost-effective alternative and provides strong conductivity and good processability. However, its higher chemical reactivity and susceptibility to oxidation under ambient or thermal stress conditions limit its stability. Al, which has a slightly lower WF (–4.1 to –4.3 eV), can also provide favorable energy-level alignment with conventional ETLs, though its chemical robustness is lower than that of Ag. Although these metals are chosen based on their balance of energy-level alignment, chemical stability, cost, and compatibility with ETLs, all of them—particularly Ag and Cu—are vulnerable to halide-induced corrosion and interfacial degradation in perovskite environments.[157] Moreover, the tendency of metal ions to migrate across the interface can distort the local energy landscape and accelerate performance losses.

View Article Online
DOI: 10.1039/D5SC10164F

Consequently, advanced ETL/cathode interlayers (CILs) have become essential for tuning effective WF, blocking ion diffusion from both the metal and the perovskite, and stabilizing the cathode contact. Such interlayers are now indispensable for achieving durable, high-efficiency inverted PeSCs.

3.3.1. Work function tuning of cathode by ETL/cathode interlayer

The energetics at electrode interfaces play a decisive role in governing both charge extraction and the long-term operational durability of PeSCs. Among many interfacial engineering strategies, modulating the cathode WF through ultrathin CILs inserted between fullerene-based ETLs (e.g., C_{60} or $PC_{61}BM$) and the top metal electrode has emerged as one of the most effective approaches. When the cathode WF is poorly aligned with the LUMO of the ETL, electron extraction becomes contact-limited, causing space-charge accumulation at the ETL/cathode interface.[159] Furthermore, directly depositing a metal cathode can create a high density of interfacial states that pin the Fermi-level at the contact. As a result, the cathode exhibits a high effective WF even when a low-work-function metal is used; therefore, the electron-extraction barrier remains present during device operation.

Introducing a dipolar interlayer alleviates these issues by establishing interfacial dipoles that reconfigure the vacuum-level alignment and suppress charge accumulation. Semiconducting interlayers with large intrinsic dipole moments—including ionic molecules, zwitterions, and functional groups capable of coordinating with the metal surface—can orient at the interface to form well-defined electrostatic dipole layers (**Fig. 11**). These layers shift the local vacuum level and thereby redefine the apparent WF of the electrode. According to the classical dipole-layer model, the magnitude of this shift (Δ) scales with the dipole density (n), dipole moment (p), and dielectric properties of the dipolar medium:[160]

$$\Delta = n\, e\, p / (k\, k_0)$$

View Article Online
DOI: 10.1039/D5SC10164F

where k is the dielectric constant of the interlayer, k_0 is the vacuum permittivity, and e is the elementary charge. As conceptually illustrated in **Fig. 12**, the introduction of a dipolar CIL between the ETL and metal electrode induces a vacuum-level upshift that lowers the electron extraction barrier while simultaneously increasing the barrier for holes.[161] This dual modulation suppresses interfacial recombination, prevents space-charge buildup, and mitigates Fermi-level pinning that typically arises at bare metal/organic interfaces. As a result, dipole-engineered CILs establish a well-aligned cathode-ETL junction, leading to improved V_{OC}, FF, and enhanced operational stability of PeSCs.

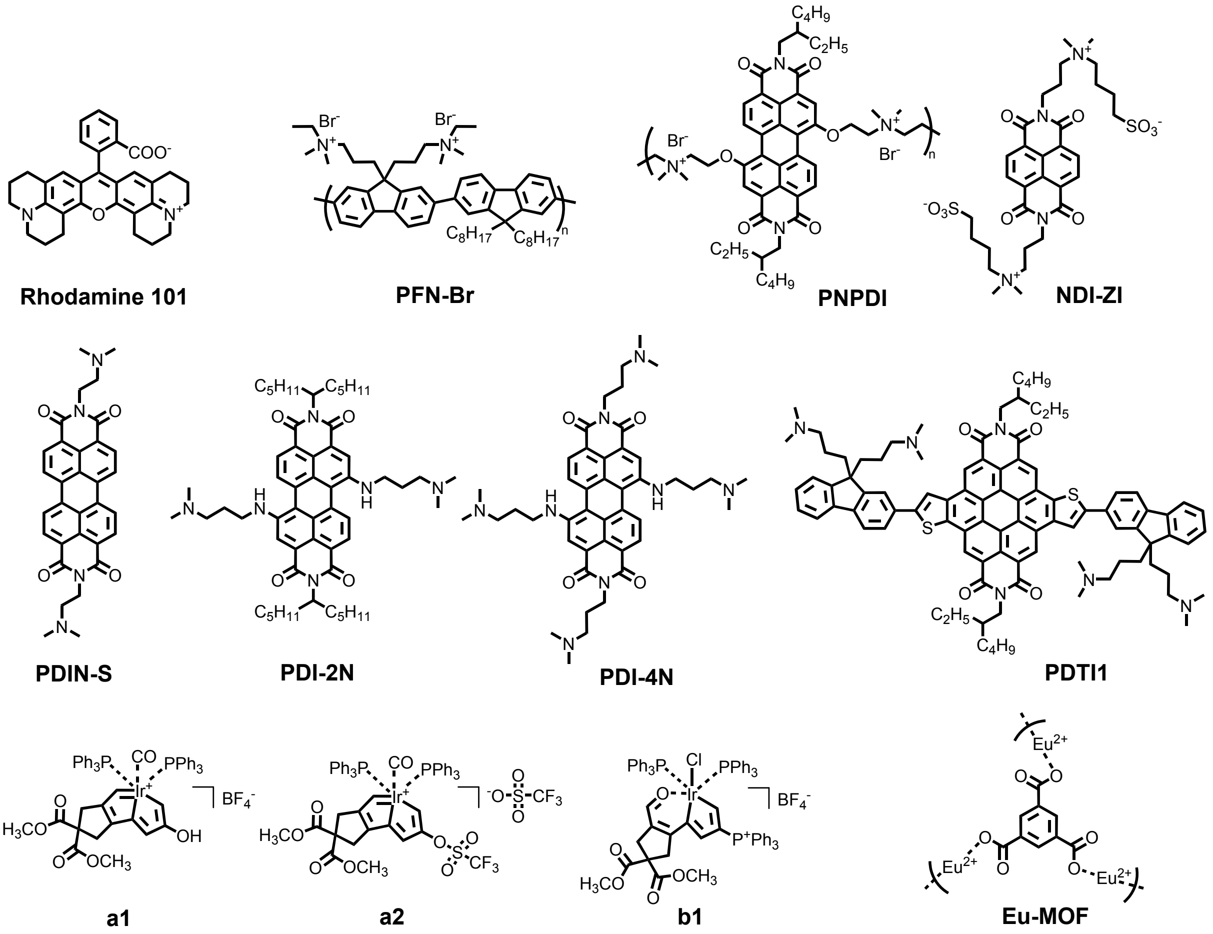

Fig. 11 Molecular structures of CIL for cathode WF tuning.

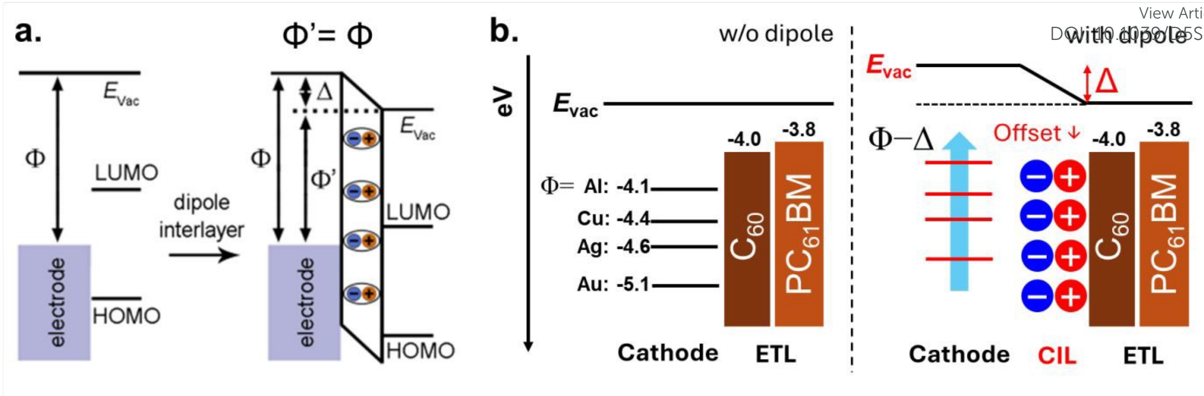

Fig. 12 The potential distribution of an electric dipole layer by introduction of CIL. (a) The interfacial dipole-induced E_{vac} shift Δ reduces the apparent WF of the electrode $\Phi' = \Phi - \Delta$. Reproduced with permission from Ref.[161]. Copyright 2020, American Chemical Society. (b) Schematic illustration of cathode materials with decreased WF and energy level alignment with ETL.

The use of LiF and BCP has long represented the benchmark for CILs in inverted PeSCs. LiF relies on the strong $\mathrm{Li^{+}}$–$\mathrm{F^{-}}$ bond dipole, whose negative pole orients toward the metal surface, thereby downshifting the vacuum level and lowering the apparent WF of cathode.[162-163] Because LiF is insulating, its thickness must remain in the tunneling regime (≤1–2 nm) to prevent electron-blocking. BCP functions through a different mechanism: its phenanthroline nitrogen atoms coordinate with Ag, forming an interfacial dipole with negative charge density near the metal and positive density toward the organic layer.[164] Although this interaction reduces the effective WF, the high LUMO energy of BCP also necessitates ultrathin films to ensure efficient electron tunneling. Motivated by the limitations of LiF and BCP, a wide range of innovative CIL materials has been developed, exploiting distinct mechanisms for WF modulation and interface stabilization. Ciro et al. introduced rhodamine 101, an ionic inner-salt dye with a large intrinsic dipole moment.[165] When inserted at the $\mathrm{PC_{61}BM}$/Ag interface, rhodamine 101 aligns its dipoles to reduce the Ag WF from –4.5 to –4.3 eV, improving energy-level matching and suppressing recombination. Devices

(ITO/NiOx/$MAPbI_3$/$PC_{71}BM$/rhodamine 101/Ag) attained efficiencies of 16.6%, while the interlayer simultaneously served as a moisture and Ag–halide corrosion barrier.

Organic semiconductors have also been widely explored as dipolar CILs. Lee et al. demonstrated PFN-Br, a conjugated polyelectrolyte with quaternary ammonium–bromide side chains, as an effective dipole-forming interlayer.[166] The polymer backbone provides electronic conductivity while the ionic substituents introduce a strong dipole that orients at the cathode interface. PFN-Br reduced the Ag WF from −4.7 to −4.2 eV, enabling better alignment with $PC_{61}BM$ and suppressing interfacial recombination. Wang et al. reported a PDI-based ionene polymer (PNPDI) functionalized with quaternary ammonium–bromide groups, designed to suppress π–π aggregation while embedding strong internal dipoles. Br^- counterions generated self-doping, enhancing conductivity and allowing electron-permissive transport (**Fig. 13a**).[167] When blended with Bphen (mixed CIL), the combined dipole strength and ordered PNPDI morphology produced a pronounced reduction in WF (**Fig. 13b**). UPS revealed that the WF of Ag reduced from -4.22 eV to -3.60 eV, correlating with increases in V_{OC}, J_{SC}, and FF. Devices (ITO/PTAA/$Cs_{0.05}(FAPbI_3)_{0.83}(MAPbBr_3)_{0.17}$/$PC_{61}BM$/PNPDI+Bphen/Ag) achieved 21.46% PCE and retained 80% of initial efficiency after 500 h at 85 °C.

Noh et al. developed a zwitterionic naphthalene diimide derivative, NDI-ZI, that introduces both dipole engineering and chemical ion capture as a thin CIL.[168] The hydrophobic NDI core stacks toward C_{60}, while zwitterionic sulfobetaine groups orient toward Ag, positioning $–SO_3^-$ groups adjacent to the metal. This configuration upshifted the Ag-side vacuum level (Ag WF from –4.6 to –4.2 eV; **Fig. 13c**) and reduced the C_{60}/Ag energy offset. Devices (ITO/MeO-2PACz/$Cs_{0.15}FA_{0.85}PbI_3$/C_{60}/NDI-ZI/Ag) exhibited suppressed shunts and leakage, achieving 23.3% PCE and superior thermal/light stability relative to control devices. Packing-induced dipole orientation has also proven decisive. Kim et al. showed that a PDI derivative with dimethylamino terminal groups (PDIN-S) exhibits morphology-dependent dipole orientation: solution processing yields edge-on packing, whereas vacuum deposition produces face-on packing with vertically aligned π–π stacking (**Fig. 13d**).[169] The latter strengthens the perpendicular dipole component, reducing Ag WF from –4.6 to –4.0 eV (**Fig. 13e**). Wu et al. synthesized PDI-2N and PDI-4N, bearing two and four dimethylamino groups, respectively.[170] PDI-4N exhibited superior solubility, conductivity (6.3×10^{-4} S cm^{-1}), and mobility (1.1×10^{-3} cm^2 V^{-1} s^{-1}) due to stronger intrinsic dipoles and enhanced self-doping. Due to the reduced WF of Ag from –4.20 to –3.60 eV (PDI-2N) and –3.18 eV (PDI-4N), devices using PDI-4N (FTO/MeO-2PACz/$Cs_x(MA_{0.17}FA_{0.83})_{(1-x)}Pb(I_{0.83}Br_{0.17})_3$/$PC_{61}BM$/PDI-4N/Ag) achieved 21.3% PCE with excellent stability (97% retention after 600 h).

Gao et al. also reported a fused-ring D–A–D PDI derivative (PDTI1) designed for strong dipole formation and high conductivity.[171] Terminal dimethylamino groups oriented negative charge toward the metal, reducing Ag WF from –4.60 to –4.03 eV (**Fig. 13f, g**). Devices (ITO/Me-4PACz/$FA_{0.7}MA_{0.3}PbI_3$/PEAI/C_{60}/PDTI1/Ag) achieved 24.6% PCE with remarkable thickness tolerance and retained 94% efficiency after 2,600 h, outperforming BCP-based devices. Wang et al. further demonstrated carbolong-derived organometallic complexes (a1, a2, b1) as CILs, where coordinated cation–anion assemblies self-orient to form strong interfacial dipoles.[172] Complex b1, containing a phosphonium cation and BF_4^-, produced the largest WF reduction (Ag: −4.26 → −3.89 eV; Au: −4.70 → −4.11 eV). Imran et al. designed a hybrid Eu-MOF@BCP interlayer, where MOF fragments incorporated into BCP introduce oriented local dipoles that modulate the interfacial electrostatic potential.[173] The Eu-MOF/BCP/Cu interface displayed a reduced WF (–4.31 eV) compared to Cu (–4.70 eV) or BCP/Cu (–4.41 eV), enabling improved electron transport and suppressed hole backflow.

Across these material classes, WF modulation consistently arises from the formation of interfacial dipoles—typically originating from intrinsic ionic character or oriented donor–acceptor motifs—that shift the vacuum level and reduce the barrier for electron extraction. These dipole-engineered interfaces provide several universal device benefits: (1) higher FF via reduced series resistance and enhanced extraction efficiency; (2) increased J_{SC} due to improved

View Article Online
DOI: 10.1039/D5SC10164F

electron transport and collection; (3) enhanced operational stability through suppressed ion migration and improved environmental resistance; and (4) reduced hysteresis through more balanced charge transport and fewer interfacial traps.

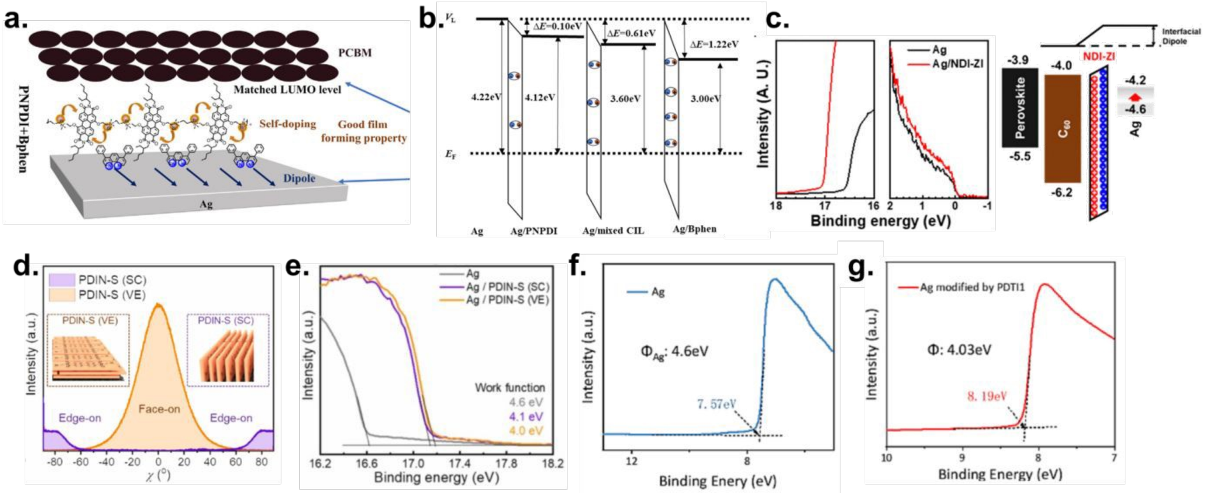

Fig. 13 Strategies and effects of CILs for cathode WF-tuning. (a) Schematic illustration of effect of PNPDI. (b) Energy level diagram of Ag with and without PNPDI or BPhen. Reproduced with permission from Ref.[167]. Copyright 2023, Elsevier Ltd. (c) UPS spectra and energy level diagram of Ag with and without NDI-ZI. Reproduced with permission from Ref.[168]. Copyright 2023, Royal Society of Chemistry. (d) Pole figures of vacuum-deposited (VE) or solution-processed (SC) PDIN-S. (e) UPS spectra of Ag with and without PDIN-S in secondary electron region. Reproduced with permission from Ref.[169]. Copyright 2024, Elsevier Ltd. (f) UPS spectra of Ag with PDTI1 in the secondary electron region at a bias voltage of −9 V. (g) UPS spectra of Ag without PDTI1 in the secondary electron region at a bias voltage of −9 V. Reproduced with permission from Ref.[171]. Copyright 2024, Elsevier Ltd.

3.3.2. Ion blocking by ETL/cathode interlayer

A major intrinsic instability in inverted PeSCs arises from the migration of ionic species within the perovskite lattice. Halide ions and organic A-site cations such as MA^+ are highly mobile under operational stresses, including heat, light, and electrical bias, and can diffuse outward from the perovskite absorber. In inverted architectures, ion migration predominantly proceeds through the ETL, most commonly C_{60}, which possesses a loosely packed morphology that facilitates ion diffusion. Under operational conditions, I^- and A-site cations migrate through

View Article Online
DOI: 10.1039/D5SC10164F

the fullerene ETL toward the metal electrode, where they react to form AgI at the buried interface (**Fig. 14a–c**).[174-175] Simultaneously, Ag or Cu species can counter-diffuse into the ETL and perovskite layers.[76, 174-180] The resulting interfacial reaction products, which are semiconducting or insulating in nature, increase series resistance, disrupt interfacial energy-level alignment, and generate trap states and shunt pathways. The accumulation of mobile ions and AgI at the interface induces electrostatic screening, suppressing electron extraction and degrading V_{OC} and FF. In addition, ion accumulation can form electrical double layers and induce internal built-in fields, leading to pronounced hysteresis and enhanced nonradiative recombination (**Fig. 14d**).[181] These coupled chemical and electrostatic effects accelerate efficiency loss and significantly shorten device lifetimes. Therefore, effectively blocking the upward migration of halide ions and organic cations toward the cathode, while simultaneously suppressing the downward diffusion of reactive metal atoms, constitutes a central design requirement for CILs in inverted PeSCs.

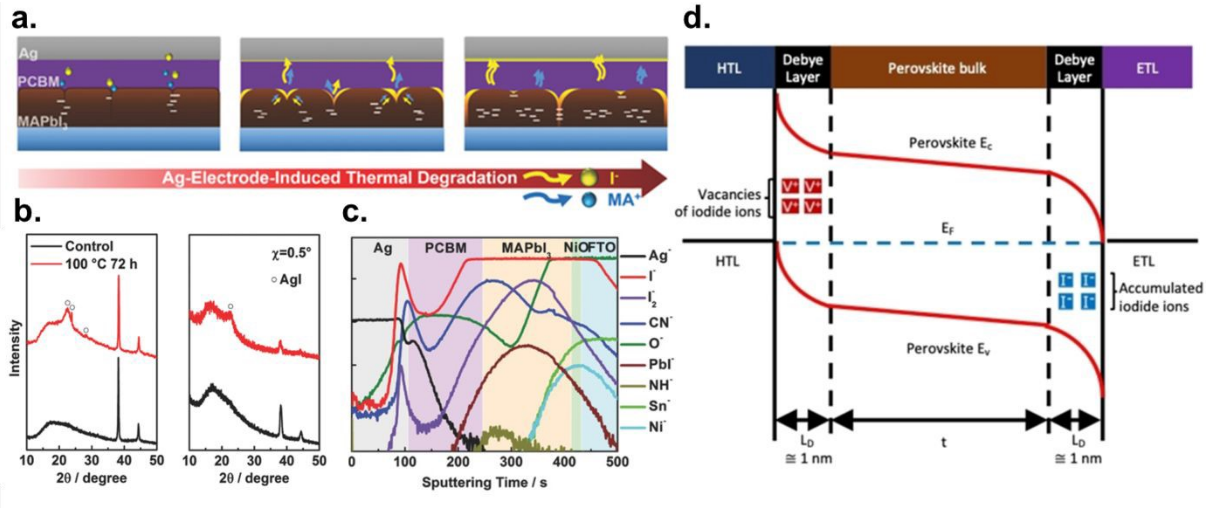

Fig. 14 Formation of AgI by ion diffusion and its impact in PeSCs. (a) Thermal degradation mechanism. (b) XRD (left) and GIXRD (right) of the peeled Ag electrodes from $MAPbI_3$-based PeSC after a thermal treatment at 100 °C for 72 h. (c) ToF-SIMS elemental depth profiles of the aged device stack after a thermal treatment at 85 °C for 24 h. Reproduced with permission from Ref.[175]. Copyright 2017, Wiley-VCH GmbH. (d) Schematic of band energy diagram in

View Article Online
DOI: 10.1039/D5SC10164F

the PeSC after ion accumulation at the interfaces. Reproduced with permission from Ref.[181] Copyright 2021, Wiley-VCH GmbH.

Several organic CIL materials are built on conjugated cores (e.g., NDI, PDI) functionalized with ionic or coordinating groups that directly interact with metals or halides, thereby suppressing the migration of mobile ionic species such as I^- and Ag^+ (**Fig. 15**). By either physically blocking diffusion pathways or chemically immobilizing ions and metal atoms, these CILs effectively interrupt the diffusion-corrosion cycle at the buried metal contact and stabilize inverted PeSC. One representative strategy relies on dense molecular packing to physically hinder ion diffusion. Ning et al. systematically investigated NDI-BN, an NDI derivative bearing four pyridine side groups that promote strong intermolecular interaction and tight film packing (**Fig. 16a**).[182] The resulting compact interlayer effectively blocked iodide diffusion from the perovskite toward the Ag electrode, as evidenced by suppressed AgI formation in XPS analysis (**Fig. 16b**).

Beyond physical blocking, chemical ion trapping provides a more active suppression mechanism. Noh et al. introduced NDI-ZI, a zwitterionic NDI derivative containing sulfobetaine side chains.[168] The fixed positive and negative charges simultaneously induce a strong interfacial dipole for work-function tuning and act as Coulombic ion capture sites for mobile I^-/ I_3^- and Ag species. While the NDI backbone ensures electron transport, the ionic side groups chemically immobilize both halides and metal ions, effectively suppressing AgI formation after thermal stress (**Fig. 16c, d**). This dual functionality illustrates how zwitterionic design enables concurrent electronic optimization and chemical stabilization. A similar zwitterionic concept was extended to PDI systems by Orwat et al., who incorporated sulfobetaine groups into PDIs with systematically varied alkyl chain lengths.[183] In these materials, perpendicular dipole alignment at the interface lowers the Ag WF, while sulfonate groups chemically bind mobile Ag^+ and halide species. Among the series, PDI-C5-S3 exhibited the optimal balance between dipole strength and ion-capturing ability (**Fig. 16e**). Wide-bandgap PeSCs employing PDI-C5-S3 (ITO/2PACz/$Cs_{0.18}FA_{0.82}Pb(I_{0.8}Br_{0.2})_3$/PEAI/$PC_{61}BM$/PDI-C5-S3/Ag) achieved 19.0% PCE under one-sun illumination and an exceptional 40.7% efficiency under indoor LED lighting, underscoring the importance of precise side-chain engineering. Wang et al. developed a tetramethylammonium-functionalized perylene derivative (TMA-PTC) as a solution-processable CIL.[184] The quaternary ammonium cations of TMA-PTC can also attract migrating I^- anions by their ionic interactions, thereby suppressing the migration of iodides to the cathode.

Another major class of CIL strategies focuses on direct chemical coordination with metal atoms, immobilizing the electrode surface and preventing metal diffusion. Yang et al. introduced a hybrid BCP:TTTS interlayer, where 1,3,5-triazine-2,4,6-trithiol trisodium salt (TTTS) provides tridentate thiol groups that form strong S–metal coordination bonds with Ag, Au, and Cu (**Fig. 16f**).[185] This chemical anchoring effectively suppresses metal in-diffusion while maintaining favorable energy-level alignment for electron extraction. Similarly, Li et al. employed benzotriazole (BTA) as an anticorrosion interlayer for Cu cathodes.[76] The triazole moiety coordinates strongly with Cu to form an insoluble [BTA–Cu] complex, which blocks both halide attack and Cu diffusion (**Fig. 16g, h**). Devices using BTA-protected Cu cathodes maintained over 92% of their initial PCE after 2,500 h in air and over 90% after 1,000 h at 85 °C. Liu et al. further demonstrated that 2-mercaptobenzothiazole (MBT) forms compact MBT–Ag coordination chains through Ag–S and Ag–N bonds, simultaneously suppressing I^- out-diffusion and Ag corrosion (**Fig. 16i, j**).[186] Another structurally elaborate systems combine chemical coordination and physical blocking. Yu et al. developed thiol-functionalized covalent organic frameworks (SH-COFs) as crystalline CILs.[187] Abundant –SH groups chemically anchor Ag atoms via Ag–S bonds, while the extended COF lattice forms a dense diffusion barrier.

View Article Online
DOI: 10.1039/D5SC10164F

In parallel, inorganic-based CILs provide intrinsically dense and chemically robust barriers. Back et al. introduced an amine-mediated TiOx (AM-TiOx) interlayer, where amine groups electrostatically trap migrating halides and MA^+ cations, suppressing ion-induced corrosion at the cathode.[188] Devices incorporating AM-TiOx maintained nearly 80% of their initial PCE for over 9,000 h in N_2. Zhu et al. demonstrated a SnO_2/W-doped ZnO bilayer, in which SnO_2 blocks ion diffusion while W doping stabilizes ZnO surface chemistry, yielding inverted devices with 23.2% PCE and enhanced thermal durability.[189] Chen et al. further showed that an ultrathin Ti interlayer exploits low diffusivity of Ti and Ti–N bonding with methylammonium, simultaneously passivating defects and blocking metal diffusion.[190]

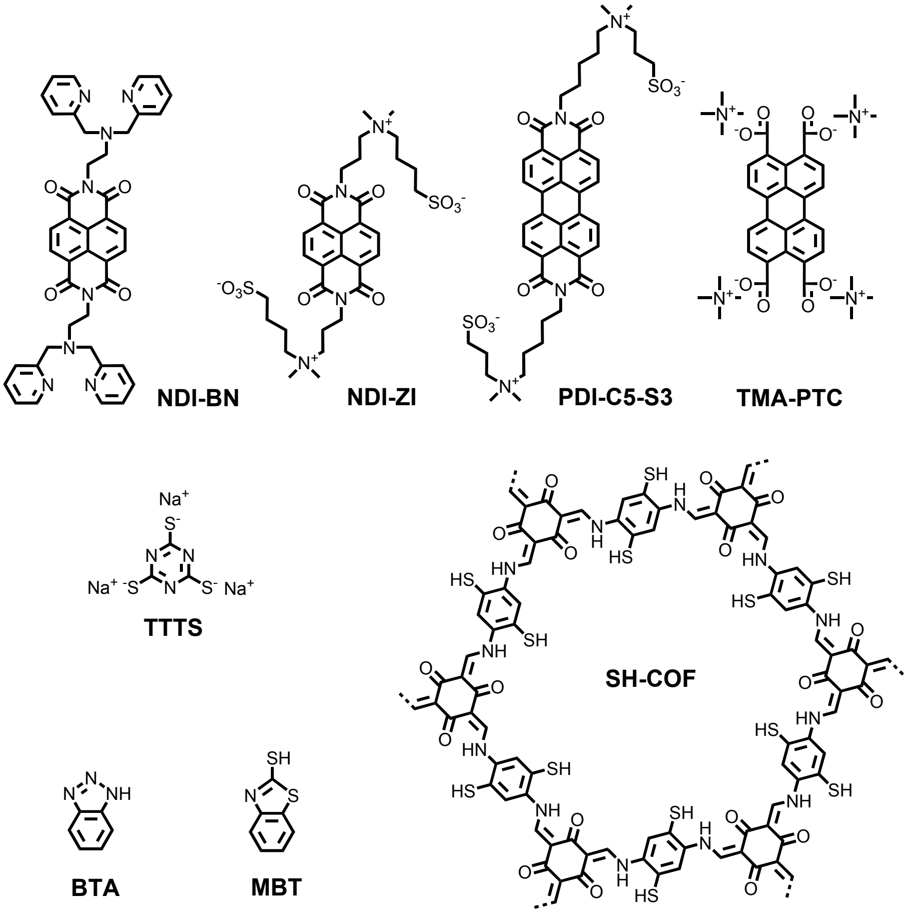

Fig. 15 Molecular structures of CIL for ion blocking.

View Article Online
DOI: 10.1039/D5SC10164F

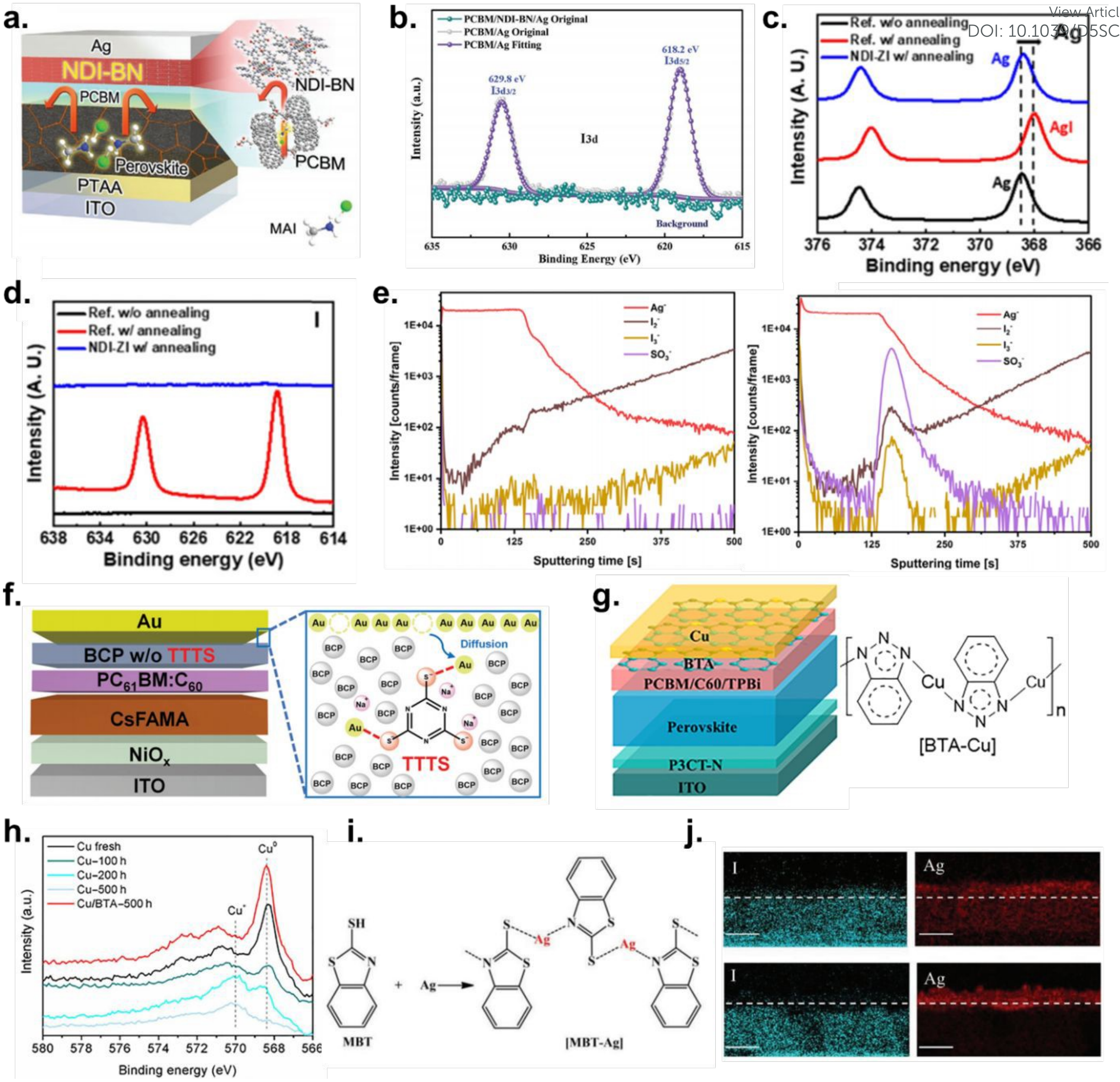

Fig. 16 (a) Device adopting NDI-BN and its molecular packing. (b) XPS spectra of Ag with and without NDI-BN after aging for 48 h. Reproduced with permission from Ref.[182]. Copyright 2020, Wiley-VCH GmbH. (c) Ag 3d and (d) I 3d XPS spectra of Ag surface with and without NDI-ZI after thermal annealing. (e) ToF-SIMS profiles of control (left) and PDI-C5-S3-adopting (right) PeSC aged at 60 °C. Reproduced with permission from Ref.[183]. Copyright 2025, Wiley-VCH GmbH. (f) Device structure and schematic illustration of BCP with TTTS. Reproduced with permission from Ref.[185]. Copyright 2022, Royal Society of Chemistry. (g) Device structure and schematic illustration of BTA-Cu. (h) Auger electron spectroscopy (AES) results of Cu electrode with and without BTA aged at 85 °C. Reproduced with permission from Ref.[76]. Copyright 2020, The American Association for the Advancement of Science. (i) Formation mechanism of MBT-Ag. (j) EDS map of I and Ag from PeSCs aged at 85 °C for 500

View Article Online
DOI: 10.1039/D5SC10164F

h without (top) and with (bottom) MBT. Reproduced with permission from Ref.[186]. Copyright 2024, Wiley-VCH GmbH.

4. Tandem-relevant interlayers

Tandem solar cells consist of multiple subcells with distinct bandgaps, enabling broadband solar absorption through spectral splitting. High-energy photons are absorbed in the wide-bandgap subcells, while lower-energy photons are transmitted to and harvested by the narrow-bandgap subcells. Owing to their high theoretical efficiency (43–46% for perovskite-based two-junction tandem architectures, according to the Shockley–Queisser limit), tandem devices are widely regarded as one of the most promising photovoltaic platforms.[191-192]

MHPs are particularly well suited for tandem integration because their optical bandgap can be tuned via compositional engineering, allowing precise spectral complementarity with various bottom cells. Accordingly, a range of perovskite-based tandem configurations—including Si-perovskite, all-perovskite, organic-perovskite, and CIGS-perovskite structures—have been extensively investigated. Among these, monolithic two-terminal (2T) Si-perovskite tandems currently deliver the highest performance, with a certified PCE of 35.0%.[1] In monolithic 2T Si-perovskite tandems, a wide-bandgap perovskite top cell is vertically stacked on a silicon bottom cell and electrically coupled in series through an interconnecting recombination layer. Under front-side illumination, incident light first enters the perovskite subcell, where short-wavelength photons are preferentially absorbed. Longer-wavelength photons are transmitted to the Si bottom cell and absorbed sequentially. Because the two subcells are series-connected, the overall tandem current is limited by the lower photocurrent of the two; therefore, precise spectral management and current matching are essential for optimal device operation.

For tandem integration, the perovskite top cell typically requires a wider optical bandgap (1.65–1.75 eV).[193-195] Such wide-bandgap absorbers are commonly realized by increasing the bromide fraction relative to iodide in mixed-halide compositions. However, under illumination, bromide and iodide ions tend to segregate, forming spatially separated Br-rich and I-rich domains. The iodide-rich regions possess a lower bandgap and act as recombination centers, reducing the QFLS and leading to a significant V_{OC} deficit in wide-bandgap devices.[196-197] To address this challenge, extensive efforts have focused on suppressing ion migration and stabilizing the mixed-halide lattice through compositional engineering, defect-passivation strategies that reduce halide-vacancy-mediated transport, and interface and dimensional engineering approaches (discussed in earlier sections). Ultimately, achieving intrinsically segregation-resistant wide-bandgap perovskites is a prerequisite for simultaneously maximizing tandem efficiency and ensuring long-term operational stability.

In this section, we discuss tandem-relevant interlayers, particularly for Si–perovskite tandem architectures. These include (i) interconnecting layers (ICLs), (ii) interlayers that enable conformal perovskite coating over textured Si bottom cells, (iii) ETLs with reduced parasitic absorption, and (iv) buffer layers that protect the perovskite stack from sputtering-induced damage during transparent electrode deposition. Consequently, these interlayers critically influence the performance and reliability of monolithic tandem devices (**Fig. 17a**).

4.1. ICLs between top and bottom subcells

Interconnecting layers (ICLs) are indispensable components in monolithic 2T tandem solar cells, positioned between the wide-bandgap top subcell and the narrow-bandgap bottom subcell to enable an efficient series electrical connection while minimizing optical and electrical losses. Functionally, an effective ICL must simultaneously satisfy three essential requirements: 1) it must provide efficient electrical interconnection by forming low-barrier contacts with adjacent carrier-selective layers and offering a highly effective recombination site for electrons and holes; 2) it must ensure optical interconnection by maintaining high transparency, particularly in the NIR region to preserve the bottom-cell photocurrent; and 3) it must serve as a mechanically and

View Article Online
DOI: 10.1039/D5SC10164F

chemically robust barrier that prevents solvent penetration and interdiffusion during the sequential processing of the top subcell. In the absence of a properly engineered ICL, direct contact between the two subcells can result in the formation of a parasitic junction, increasing recombination resistance and substantially degrading tandem performance.

Two principal ICL design strategies have been developed: tunnel-junction (TJ)-based and recombination-layer (RL)-based architectures. TJ-based ICLs rely on degenerately doped p++/n++ junctions that enable carrier tunneling and recombination with minimal voltage drop, thereby offering highly efficient electrical coupling in principle. However, realizing sufficiently strong and stable doping— particularly in multilayer device stacks fabricated by solution processing—while simultaneously ensuring solvent resistance and structural robustness remains technically challenging. In contrast, RL-based ICLs introduce an explicit recombination medium, such as sputtered TCOs, ultrathin metals (~1 nm), or conductive polymers, between the charge-selective layers. These structures often enhance recombination efficiency and improve FF, yet they require meticulous control over sputter-induced damage, shunt formation, and parasitic optical absorption.

Because the two subcells are connected in series, ICL design directly governs both performance and stability. Electrically inefficient or energetically misaligned ICLs increase the effective recombination resistance at the interconnection and may even form a parasitic diode, leading to V_{OC} losses. Ideally, the tandem V_{OC} should approach the sum of the QFLS of the individual subcells. Non-ideal ICLs introduce several loss mechanisms: i) energy-level misalignment can cause barrier-induced carrier accumulation, leading to interfacial charge build-up, enhanced non-radiative recombination, and reduced subcell QFLS; ii) insufficient recombination capacity within the ICL can create a recombination-limited bottleneck that lowers FF; and iii) structural defects such as pinholes can generate shunt or leakage pathways that degrade both FF and V_{OC}. From an optical standpoint, absorbing or excessively thick

View Article Online
DOI: 10.1039/D5SC10164F

interlayers reduce NIR transmission and limit the tandem J_{SC}, further emphasizing the need for carefully optimized thickness and material selection.

Recent studies illustrate how rational ICL engineering can address these limitations. For instance, Zheng et al. introduced a hybrid NiO_X/MeO-2PACz ICL in monolithic Si-perovskite tandems that avoids direct perovskite–TCO contact, thereby suppressing defect-driven shunt and leakage pathways at the interface.[198] Conductive atomic force microscope (c-AFM) images indicate that NiO_X/MeO-2PACz hybrid layer exhibited better uniformity and less leakage current than the NiO_X and MeO-2PACz films prepared on ITO substrate (**Fig. 17b**). By mitigating leakage-related losses and reducing interfacial non-radiative recombination, this strategy achieved a PCE of 28.47% with an FF of 81.8%, alongside improved reproducibility and operational stability. Similarly, An et al. addressed barrier-induced carrier accumulation by employing a SAM (CbzNaph)-anchored MoO_3 interconnection structure that balances carrier transport and enhances hole extraction, thereby reducing charge build-up at the series junction.[199] Tandem devices incorporating this tailored ICL delivered a PCE of 26.05%, a V_{OC} of 2.21 V, and high operational stability.

Collectively, these advances underscore that ICLs are not merely passive interlayers but decisive functional elements that govern recombination dynamics, voltage additivity, current continuity, and long-term robustness in monolithic tandems. Continued progress in ICL material selection and structural design—aimed at minimizing electrical and optical interconnection losses while enhancing chemical and processing resilience—will be pivotal for realizing high-efficiency, stable 2T tandem solar cells.

4.2. Interlayers on textured Si bottom cells

In Si-perovskite tandem solar cells, microscale pyramid texturing of the Si bottom cell is widely employed to suppress front-surface reflection and enhance light trapping. Random (111)-oriented pyramids, typically 2-4 μm in height, induce multiple internal reflections,

View Article Online
DOI: 10.1039/D5SC10164F

thereby increasing the optical path length within Si and boosting the photocurrent of the bottom sub-cell. Such textures are most commonly fabricated by anisotropic alkaline etching using KOH, NaOH, or TMAH, which exploit crystallographic etch-rate selectivity to form ordered pyramidal arrays.[200-202]

Despite their optical advantages, fully textured Si surfaces pose significant challenges for subsequent solution processing of perovskite layers. Achieving conformal coverage of micrometer-scale pyramids remains difficult because the perovskite precursor solution tends to dewet from sharp features, bridge across pyramid valleys, and leave voids or pinholes. These morphological defects can induce shunting pathways and exacerbate interfacial recombination, ultimately degrading device performance and yield **(Fig. 17c)**.[236] To address this trade-off between optical light trapping and conformal coating, several strategies have been explored. A straightforward approach involves reducing the pyramid dimensions to sub-micrometer scales ("mild texturing"), thereby decreasing surface roughness and improving precursor wetting.[203-205] In this configuration, the perovskite thickness can readily exceed the substrate topography, enabling uniform film formation. However, limiting pyramid height inevitably compromises the maximum achievable light-trapping capability. Alternatively, the original micrometer-scale pyramids can be retained while introducing hierarchical micro/nanotextures to promote improved wetting and nucleation.[206] Although this strategy preserves optical benefits, it generally requires additional etching or surface modification steps, increasing process complexity and manufacturing cost.

More recently, inorganic NP interlayers have emerged as an effective and scalable solution to this conformality challenge. For example, Liu et al. introduced an Al_2O_3 NP interlayer via spray coating to render the textured Si surface superhydrophilic.[207] This treatment enhances perovskite precursor spreading and wet-film continuity across pyramid tips and sidewalls. The NPs additionally serve as distributed heterogeneous nucleation sites, mitigating valley-dominant crystallization and promoting more homogeneous perovskite growth. Similarly,

View Article Online
DOI: 10.1039/D5SC10164F

Zhang et al. employed SiO_X nanospheres as a nano-filler interlayer to locally smooth sharp valleys and steep facets without sacrificing the global light-trapping texture.[208] This localized topographical regulation facilitates continuous HTL deposition and enables pinhole-free, conformal perovskite coverage on fully textured substrates. Collectively, these NP-enabled interface engineering strategies demonstrate that the inherent limitations of solution coating on micron-scale pyramids can be overcome by combining enhanced wetting with guided nucleation or texture-aware surface modulation. From an industrial perspective, such inorganic NP interlayers are particularly attractive because they can be implemented via low-temperature, solution-based processes (e.g., spray or colloidal deposition) compatible with large-area manufacturing.

4.3. ETLs on perovskite top cell with reduced parasitic absorption

Although fullerene derivatives such as C_{60} and its functionalized analogues are widely employed as ETLs in high-efficiency inverted PeSCs, their intrinsic optical absorption presents a critical limitation for Si-perovskite tandem applications. Fullerene-based ETLs exhibit appreciable absorption in the near-UV and blue spectral region (≈330-450 nm), with residual absorption extending into the green region (≈450-550 nm). Even at typical thicknesses of 20-30 nm, illumination through the ETL induces short-wavelength parasitic losses that can reduce the J_{SC} by approximately 1.5 mA cm^{-2}.[209] In monolithic tandem architectures, where efficient photon utilization is essential for subcell current matching, such losses directly constrain overall device performance. Consequently, substantial research efforts have focused on minimizing ETL parasitic absorption while preserving efficient electron extraction and interfacial selectivity.

One major strategy involves replacing fullerene-based ETLs with highly transparent wide-bandgap metal oxides, most notably SnO_2. Owing to its large bandgap (≈3.6-4.5 eV), SnO_2 exhibits high optical transparency across the visible spectrum, typically exceeding 80%

View Article Online
DOI: 10.1039/D5SC10164F

transmittance between 400 and 800 nm (**Fig. 17d**).[209] This significantly reduces parasitic absorption and increases the fraction of incident photons reaching the perovskite absorber. However, in inverted configurations, SnO_2 must be deposited directly onto the perovskite layer directly onto the perovskite layer, which imposes stringent solvent orthogonality requirements. Most polar solvents effective for dispersing colloidal SnO_2 can damage perovskite films, limiting solution processing to a narrow selection of perovskite-compatible solvents. To overcome this constraint, ligand engineering of SnO_2 NP s is frequently implemented to enable stable dispersions in benign solvents. Chapagain et al. implemented a ligand exchange strategy in which hydrous SnO_2 NP s were capped with acetate, yielding stable ethanol-based inks compatible with perovskite surfaces.[210] The use of short-chain acetate ligands minimized electrical losses by limiting the insulating barrier at the interface. In addition, hydrogen bonding between surface-bound acetate groups and ethanol was proposed to enhance colloidal dispersibility, enabling direct deposition onto the perovskite layer without the need for an additional interlayer. Similarly, Kim et al. reported long-term colloidal stability in a low-polarity chloroform/1-butanol cosolvent system, which they attributed to the presence of surface Cl^- species.[209] They further introduced ethylenediamine (EDA) as a bridging ligand that coordinates to perovskite surface defects while simultaneously anchoring to SnO_2 NPs, thereby promoting intimate interfacial contact and improved electronic coupling.

Another effective strategy to suppress parasitic absorption is to reduce the thickness of fullerene-based ETLs while maintaining efficient electron extraction and interfacial selectivity, as optical losses scale with both the absorber thickness and the fullerene volume fraction. Recent studies have demonstrated two complementary design approaches that enable thickness- and/or absorption-minimized ETLs without sacrificing device performance. Cui et al. introduced an ultrathin PO-T2T interlayer (~0.5 nm) to improve heterointerfacial contact and charge selectivity. [211] This modification allowed the ETL stack thickness to be reduced from 20 nm C_{60}/20 nm ALD SnO_2 to 15 nm C_{60}/17 nm ALD SnO_2 without compromising photovoltaic performance. Also the transmittance spectra of the thin films reveal that thinner C_{60} and ALD SnO_2 layers exhibit higher transmittance across the entire wavelength range (**Fig. 17e**). In parallel, Poma et al. adopted a materials-centric approach by blending an NDI-based polymer (pNDI) with C_{60} to form a composite ETL (pNDI-C_{60}).[212] This hybrid layer not only improved mechanical robustness but also reduced optical absorption relative to neat evaporated C_{60}. Because pNDI exhibits only weak absorption, primarily below ~400 nm, it effectively dilutes the C_{60} fraction and lowers the overall absorptance of the ETL. As a result, the pNDI-C_{60} layer increases transmitted optical power through the ETL stack and alleviates parasitic absorption, even without aggressive thickness reduction.

Taken together, these developments demonstrate that parasitic absorption in ETLs for Si-perovskite tandems can be systematically mitigated either by substituting highly transparent metal oxides such as SnO_2 for fullerene derivatives or by rationally engineering thinner and optically diluted fullerene-based layers. In both cases, the central design objective is to balance optical transparency with robust electron extraction and interfacial selectivity, thereby maximizing photocurrent while sustaining high FF and operational stability in tandem architectures.

4.4. Buffer layers on perovskite top cell for sputter damage mitigation

In Si-perovskite tandem photovoltaics, electrode design requirements differ substantially from those of single-junction devices. Because illumination occurs through the top subcell, the front electrode must be highly transparent while maintaining low sheet resistance to enable efficient lateral charge collection over large areas. Generally, transparent contacts typically employ sputtered transparent conductive oxides (TCOs), most commonly ITO or IZO, often combined with a metal grid or mesh to further reduce series resistance without incurring excessive optical losses.[213-214]

However, TCO sputtering can significantly degrade the underlying perovskite stack. The plasma environment generates energetic ions, neutral particles, UV radiation, and localized

View Article Online
DOI: 10.1039/D5SC10164F

heating, all of which can physically damage soft organic layers such as fullerene-based ETLs, increase defect density, and enhance non-radiative recombination.[215-216] In particular, with respect to ion-induced damage, the mechanism is unlikely to involve direct ion penetration into the perovskite. Instead, oxygen, argon, indium, and tin ions are predicted to stop within the C_{60} overlayer at depths below ~5 nm, indicating that the damage is more plausibly associated with near-surface collision cascades and recoil-induced defect formation (**Fig. 17f**).[215] Additionally, sputter-induced mechanical stress may cause interfacial delamination or deteriorate contact quality.[217] To mitigate these effects, monolithic Si-perovskite tandems typically incorporate a thin buffer layer between the perovskite-side transport layers and the sputtered TCO. Buffer layers can be classified according to their deposition method: solution processing, thermal evaporation, and chemical vapor deposition (CVD), including atomic layer deposition (ALD).

4.4.1 Solution-processed buffer layers

Solution processing is attractive due to its simplicity and low-temperature compatibility, often employing pre-synthesized NPs dispersed in low-polarity, low–boiling-point solvents. Representative NP buffers include ZnO, SnO_2, Al-doped ZnO (AZO), ITO, tungsten oxide (WO_X), and related variants such as ZnMgO blends.[218-221] Polyelectrolytes such as polyethylenimine ethoxylated (PEIE) have also been demonstrated to protect sensitive fullerene layers from sputter damage and have been successfully implemented in monolithic 2T tandems.[216, 222] Despite these advantages, solvent compatibility with the underlying perovskite stack must be carefully controlled. Moreover, NP films typically require a minimum thickness to achieve full surface coverage, making the fabrication of ultrathin (~5 nm), pinhole-free buffers challenging.

4.4.2 Thermally evaporated buffer layers

Thermal evaporation is often preferred for rough or textured surfaces because it is a solvent-free, relatively “soft” vacuum process capable of producing uniform films over large areas with low kinetic energy flux.[223] In addition to ultrathin metals (e.g., Ag or Mg:Ag), a wide range of evaporated organic or organometallic materials has been explored, including copper(II) phthalocyanine (CuPc), zinc phthalocyanine (ZnPc), BCP, 1,4,5,8,9,11-hexaazatriphenylenehexacarbonitrile (HAT-CN) and metal acetylacetonate complexes.[224-228] Robust organic semiconductors such perylene-3,4,9,10-tetracarboxylic dianhydride (PTCDA) offers chemical inertness and effective energy dissipation under plasma exposure[229-230], while materials like HAT-CN provide high visible transparency and favorable interfacial energetics.[231-232] Nevertheless, many organic buffers exhibit parasitic absorption in the visible region. Furthermore, effective protection generally requires thicknesses exceeding ~10 nm to avoid island-like growth and pinhole formation, which can increase optical losses and series resistance.

4.4.3 ALD/CVD-based buffer layers

Chemical vapor deposition approaches, particularly ALD, are well suited for forming conformal, pinhole-free ultrathin buffers on complex or high–aspect-ratio surfaces. Because precursor adsorption is diffusion-driven and non-directional, ALD enables nearly uniform thickness over textured features at relatively low temperatures. Common ALD buffer materials include SnO_2 and ZnO, V_xO_y and ultrathin insulating Al_2O_3 layers (1-2 nm), which can function as effective plasma-damage barriers when carefully thickness-optimized.[233-235] When applying ALD/CVD buffers to perovskite stacks, several constraints must be addressed. 1) Precursors must not chemically react with or degrade the underlying perovskite or organic transport layers. 2) Uniform ALD nucleation often requires surface -OH groups, potentially necessitating mild surface activation (e.g., UV-ozone treatment) or an ultrathin -OH-rich seed layer such as PEIE. 3) Deposition temperatures (typically 80-100 °C) and exposure conditions must remain sufficiently mild to prevent thermally induced perovskite degradation.

View Article Online
DOI: 10.1039/D5SC10164F

Overall, buffer layer engineering in tandem-compatible perovskite solar cells is not merely a protective strategy but a critical interface optimization problem, requiring simultaneous control of plasma resilience, optical transparency, electrical conductivity, and interfacial energetics to preserve both efficiency and long-term device stability.

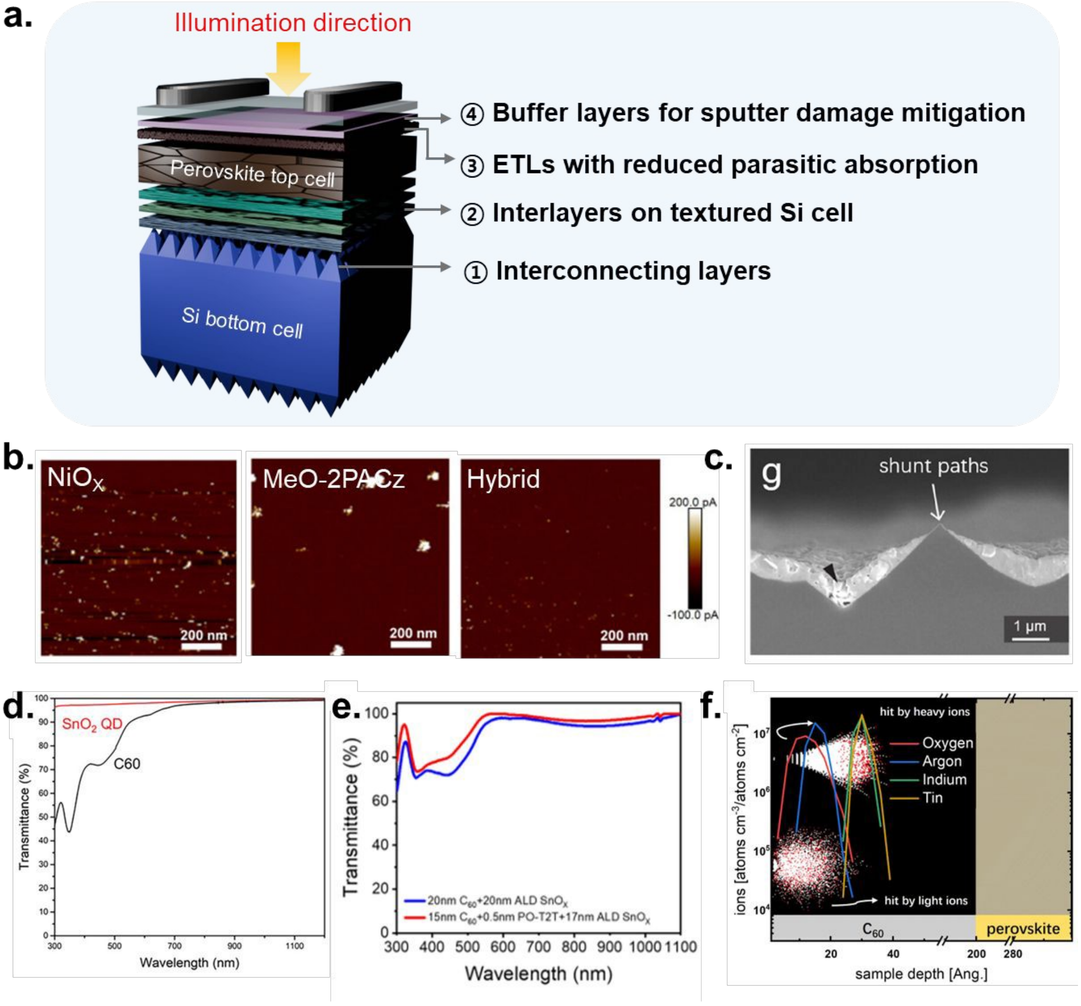

Fig. 17 (a) Interlayers in Si-perovskite tandem solar cells (b) c-AFM images of Si/ITO/NiOx, Si/ITO/MeO-2PACz, and Si/ITO/NiOx/MeO-2PACz films. Reproduced under the terms of the CC-BY Creative Commons Attribution 4.0 International license (https://creativecommons.org/licenses/by/4.0) from Ref.[198]. Copyright 2024, Elsevier. (c) Perovskite layers deposited on the micron-scale pyramid texture. Reproduced under the terms of the CC-BY Creative Commons Attribution 4.0 International license (https://creativecommons.org/licenses/by/4.0) from Ref.[236]. Copyright 2024, John Wiley & Sons. (d) Transmittance of SnO_2 QDs and C_{60} films. Reproduced under the terms of the CC-BY Creative Commons Attribution 4.0 International license (https://creativecommons.org/licenses/by/4.0) from Ref.[209]. Copyright 2024, Wiley-VCH

View Article Online
DOI: 10.1039/D5SC10164F

GmbH (e) Transmittance spectra of films with thin C_{60} and ALD SnO_2 layers. Reproduced with permission from Ref.[211]. Copyright 2025, Wiley-VCH GmbH. (f) Ion penetration depth distribution induced by sputtering plasma in the perovskite/C_{60} stack. Reproduced under the terms of the CC-BY Creative Commons Attribution 4.0 International license (https://creativecommons.org/licenses/by/4.0) from Ref.[215]. Copyright 2024, The Royal Society of Chemistry.

5. Outlook and prospects

Based on recent progress, the roles of upper-surface and interface modification strategies can be broadly categorized into four functions: (1) perovskite top-surface defect passivation and improving energy-level alignment at the perovskite/ETL and ETL/cathode interfaces; (2) acting as barrier layers to block moisture and oxygen ingress while suppressing mobile-ion diffusion; (3) enabling internal and interfacial thermal management to facilitate efficient heat dissipation; and (4) replacing thermally and mechanically unstable ETLs, such as C_{60} and $PC_{61}BM$. Collectively, these approaches underscore the critical importance of perovskite upper-surface engineering, where tailored interfacial materials can deliver distinct yet complementary functions—from contact optimization to robust barrier effects—ultimately enhancing device stability.

Despite this progress, several challenges must be addressed to further advance inverted PeSCs. First, greater attention should be paid to defect generation under operational conditions. Upper-stack stability is governed not only by pre-existing defects but also by defects newly formed under illumination, electric fields, and local heating. These stresses can reconstruct the perovskite top surface and activate metastable pathways, generating fresh nonradiative recombination centers at the perovskite/ETL interface. Future strategies should therefore move beyond static passivation toward interface designs that actively suppress defect formation during operation. In this context, combining operando spectroscopic techniques with time-

View Article Online
DOI: 10.1039/D5SC10164F

resolved electrical measurements will be critical for identifying when and where defect-related loss pathways emerge under light and bias.

Second, mechanical integrity at the perovskite/ETL/cathode interfaces remains an underappreciated bottleneck for long-term reliability. The upper stack integrates perovskites with organic and inorganic layers that possess mismatched elastic moduli and thermal-expansion coefficients, rendering the interfaces vulnerable to delamination and microcrack formation during thermal cycling. Such adhesion loss can create local contact failure and diffusion pathways (for O_2 and water), thereby accelerating chemical and electrochemical degradation. Accordingly, adhesion should be treated as a key design parameter in future upper-stack engineering. Molecularly engineered interlayers that enhance interfacial bonding while preserving ultrathin charge-transport pathways offer a promising solution.

Third, interfacial damage induced during electrode formation must be carefully considered. As emerging device architectures—including tandem, semitransparent, bifacial, and module-level configurations—expand beyond conventional metal electrodes, the deposition processes themselves can compromise the integrity of carefully engineered upper interfaces. Sputtering of transparent conductive electrodes can cause ion bombardment or plasma-induced damage to the ETL and perovskite surface. Consequently, well-designed perovskite/ETL stacks can fail if electrode deposition introduces new defects or disrupts interfacial continuity. Effective solutions should therefore integrate deposition-compatible interlayers that function as sacrificial or protective buffers without incurring optical or electrical penalties.

Finally, standardized multi-stress testing protocols are urgently needed for the reliable design of inverted PeSCs. Device degradation is often accelerated by synergistic interactions among heat, light, electrical bias, moisture, and oxygen, yet many studies continue to evaluate stability under isolated stress conditions. The establishment of unified, multi-factor evaluation protocols will help identify dominant degradation triggers and guide rational selection of

View Article Online
DOI: 10.1039/D5SC10164F

interlayers, ETLs, and electrodes. Such comprehensive reliability assessments will be pivotal for translating laboratory-scale interface innovations into commercially viable technologies.

In summary, PeSCs are transitioning from a laboratory-driven research phase toward commercialization-oriented development. As efficiencies continue to rise, the central question is no longer whether perovskites can achieve high performance, but whether they can sustain reliable operation under realistic conditions and at manufacturing scale. A deeper understanding of how materials, interfaces, and large-area processes behave under realistic operating and degradation environments is essential for translating record laboratory performance into industrially relevant photovoltaic technologies.

Data availability

No primary research results, software, or code have been included, and no new data were generated or analysed as part of this review.

Author contributions

S.P. and J.B.P. mainly contributed to the writing and edit the initial manuscript. J.M.H. and H.S.K. revised the manuscript. M.H.S. and H.Y.W. conceived the idea of the review article and supervised it.

Conflicts of interest

There are no conflicts to declare

Acknowledgements

This work was supported by the National Research Foundation of Korea (NRF) grant funded by the Korea government (RS-2024-00334832, RS-2025-24683763), Korea Institute of Energy Technology Evaluation and Planning (KETEP) grant funded by the Korea government (MOTIE) (20213091010010, Super Solar Cells - Development of double junction solar cells, breakthrough for the theoretical limit of silicon solar cell efficiency (>35%)), the Nano and Material Technology Development Program through the NRF funded by the Ministry of Science and ICT (RS-2025-25442266), InnoCORE program of the Ministry of Science and ICT (1.250021.01).

References

View Article Online
DOI: 10.1039/D5SC10164F

1. National Renewable Energy Laboratory. ‘‘Best Research-Cell Efficiency Chart’’, https://www.nrel.gov/pv/cell-efficiency.html.
2. G. Li, Z. Zhang, B. Agyei-Tuffour, L. Wu, T. W. Gries, K. Prashanthan, L. Frohloff, A. Musiienko, J. Li, R. Zhu, L. J. F. Hart, L. Wang, Z. Li, B. Hou, N. Koch, M. Saba, P. R. F. Barnes, J. Nelson, P. J. Dyson, M. K. Nazeeruddin, M. Li and A. Abate, *Nat. Photonics*, 2026, **20**, 55-62.
3. C. Tian, A. Sun, J. Chen, R. Zhuang, C. Chen, J. Zheng, S. Liu, J. Du, Q. Chen, L. Cai, S. Han, F. Tian and C.-C. Chen, *Nat. Photonics*, 2026, **20**, 287-295.
4. J. Park, L. Chetan, H. Kim, J.-S. Jee, Y.-S. Gal and S.-H. Jin, *Macromol. Res.*, 2024, **32**, 505-513.
5. H. Choi, H. Kim, J. Lim, B.-J. Chang and S. Song, *Macromol. Res.*, 2024, **32**, 825-832.
6. B. Dong, M. Wei, Y. Li, Y. Yang, W. Ma, Y. Zhang, Y. Ran, M. Cui, Z. Su, Q. Fan, Z. Bi, T. Edvinsson, Z. Ding, H. Ju, S. You, S. M. Zakeeruddin, X. Li, A. Hagfeldt, M. Grätzel and Y. Liu, *Nat. Energy*, 2025, **10**, 342-353.
7. G. Qu, S. Cai, Y. Qiao, D. Wang, S. Gong, D. Khan, Y. Wang, K. Jiang, Q. Chen, L. Zhang, Y.-G. Wang, X. Chen, A. K. Y. Jen and Z.-X. Xu, *Joule*, 2024, **8**, 2123-2134.
8. W. Jiang, G. Qu, X. Huang, X. Chen, L. Chi, T. Wang, C.-T. Wong, F. R. Lin, C. Yang, Q. Jiang, S. Wu, J. Zhang and A. K. Y. Jen, *Nature*, 2025, **646**, 95-101.
9. W. Li, E. Martínez-Ferrero and E. Palomares, *Mater. Chem. Front.*, 2024, **8**, 681-699.
10. M. Li, M. Liu, F. Qi, F. R. Lin and A. K. Y. Jen, *Chem. Rev.*, 2024, **124**, 2138-2204.
11. J. Suo, B. Yang, D. Bogachuk, G. Boschloo and A. Hagfeldt, *Adv. Energy Mater.*, 2025, **15**, 2400205.
12. K. Guo, H. Tang, L. Han, R. Qi, H. Yan, G. Gao, W. Lv, M. Li, J. Xia, B. Cai, G. Xing, R. Chen and G. Wu, *ACS Energy Lett.*, 2025, **10**, 4882-4910.
13. C. E. Puerto Galvis, D. A. González Ruiz, E. Martínez-Ferrero and E. Palomares, *Chem. Sci.*, 2024, **15**, 1534-1556.
14. R. Chen, J. Wang, Z. Liu, F. Ren, S. Liu, J. Zhou, H. Wang, X. Meng, Z. Zhang, X. Guan, W. Liang, P. A. Troshin, Y. Qi, L. Han and W. Chen, *Nat. Energy*, 2023, **8**, 839-849.
15. X. Qiao, R. Zhu, D. Yan, Z. Su, Z. Zhang, H. Wu, Y. Tan, M. Liang, W. Zuo, J. Zhang, G. Li, X. Gao, M. Saliba and M. Li, *Adv. Funct. Mater.*, 2024, **34**, 2409852.
16. H. Sun, S. Wang, S. Qi, P. Wang, R. Li, B. Shi, Q. Zhang, Q. Huang, S. Xu, Y. Zhao and X. Zhang, *Adv. Funct. Mater.*, 2023, **33**, 2213913.

17. N. Aristidou, C. Eames, I. Sanchez-Molina, X. Bu, J. Kosco, M. S. Islam and S. A. Haque, *Nat. Commun.*, 2017, **8**, 15218.
18. B. Rivkin, P. Fassl, Q. Sun, A. D. Taylor, Z. Chen and Y. Vaynzof, *ACS Omega*, 2018, **3**, 10042-10047.
19. S. Suragtkhuu, P. Myagmarsereejid, Q. T. Trinh, T. Tsagaantsooj, A. D. Slattery, A. Adenle, S. Purevdorj, E. Campbell, O. E. FitzGerald, T. J. Z. Stock, S. Jamali, T. J. Macdonald, T. Gould, N.-T. Nguyen, C. Adachi, Y. L. Zhong and M. Batmunkh, *EES Solar*, 2025, **1**, 857-867.
20. C. Chen, P. Zhu, X. Dong, Y. Dou, Y. Zhang, J. Liang, R. Mao, Y. Jiang, J. Wang, M. Wang, S. Chen and J. Zhu, *Chem. Eng. J.*, 2024, **489**, 151403.
21. Z. Liu, H. Li, Z. Chu, R. Xia, J. Wen, Y. Mo, H. Zhu, H. Luo, X. Zheng, Z. Huang, X. Luo, B. Wang, X. Zhang, G. Yang, Z. Feng, Y. Chen, W. Kong, J. Gao and H. Tan, *Adv. Mater.*, 2024, **36**, 2308370.
22. Y. Zheng, Y. Li, R. Zhuang, X. Wu, C. Tian, A. Sun, C. Chen, Y. Guo, Y. Hua, K. Meng, K. Wu and C.-C. Chen, *Energy Environ. Sci.*, 2024, **17**, 1153-1162.
23. J. Warby, F. Zu, S. Zeiske, E. Gutierrez-Partida, L. Frohloff, S. Kahmann, K. Frohna, E. Mosconi, E. Radicchi, F. Lang, S. Shah, F. Peña-Camargo, H. Hempel, T. Unold, N. Koch, A. Armin, F. De Angelis, S. D. Stranks, D. Neher and M. Stolterfoht, *Adv. Energy Mater.*, 2022, **12**, 2103567.
24. M. Stolterfoht, P. Caprioglio, C. M. Wolff, J. A. Márquez, J. Nordmann, S. Zhang, D. Rothhardt, U. Hörmann, Y. Amir, A. Redinger, L. Kegelmann, F. Zu, S. Albrecht, N. Koch, T. Kirchartz, M. Saliba, T. Unold and D. Neher, *Energy Environ. Sci.*, 2019, **12**, 2778-2788.
25. Z. Xing, S. Ma, B.-W. Chen, M. An, A. Fan, X. Hu, Y. Wang, L.-L. Deng, Q. Huang, H. Kanda, F. G. Al-Amri, G. Pozzi, Y. Zhang, J. Xia, J. Wu, X. Guo and M. K. Nazeeruddin, *Joule*, 2025, **9**, 101817.
26. J. Yin, X. Shi, L. Wang, H. Yan and S. Chen, *Angew. Chem. Int. Ed.*, 2022, **61**, e202210610.
27. F. Li, C. Zhao, Y. Li, Z. Zhang, X. Huang, Y. Zhang, J. Fang, T. Bian, Z. Zeng, J. Yin and A. K. Y. Jen, *Sci. Adv.*, 2024, **10**, eadq1150.
28. S. Liu, T. Miao, J. Wang, Y. Zhang, R. Chen, X. Lei, W. Qin, Z. Zhu, L. Lu, Z. Chen, P. Cui, L. Li, M. Li, E. Xu, Y. Shen, S. C. Cho, S. U. Lee, S.-H. Cho, Z. Liu, W. Chen and N.-G. Park, *Nat. Energy*, 2026, **11**, 109-120.

View Article Online
DOI: 10.1039/D5SC10164F

29. Y. Feng, Y. Wang, H. Yang, S. Li, J. Luo, X. Han, T. Alshahrani, B. Mai, D. Wang, Z. Ding, W. Sun, C. Sun, Q. Chen, K. Wei, Y. Feng, L. Song, X. Li, X.-Y. Wang, W.-D. Li, Q. An, Y. Jiang and M. Yuan, *Angew. Chem. Int. Ed.*, 2025, **64**, e202505876.
30. D. Gao, B. Li, X. Sun, Q. Liu, C. Zhang, L. Qian, Z. Yu, X. Li, X. Wu, B. Liu, N. Wang, F. Vanin, X. Xia, J. Gong, N. Li, X. C. Zeng, Z. a. Li and Z. Zhu, *Nat. Photonics*, 2025, **19**, 1070-1077.
31. J. Yang, G. Qu, Y. Qiao, S. Cai, J. Hu, S. Geng, Y. Li, Y. Jin, N. Shen, S. Chen, A. K. Y. Jen and Z.-X. Xu, *Nat. Commun.*, 2025, **16**, 6968.
32. J. Zhang, N. Yan, Y. Cao, Y. Li, R. Wang, D. Qi, J. Pi, N. Li, X. Feng, J. Wu, X. Liu, X. Gao, Y. Liu, S. Liu and J. Feng, *Adv. Mater.*, 2026, **38**, e11162.
33. K. Feng, G. Wang, Q. Lian, S. Gámez-Valenzuela, B. Li, R. Ding, W. Yang, K. Wang, J. Zeng, Y. Zhang, S. Y. Jeong, B. Xu, A. Ho-Baillie, H. Y. Woo, A. Facchetti and X. Guo, *Nat. Mater.*, 2025, **24**, 770-777.
34. Y. Zhang, Y. Liu, Z. Zhao, T. Kong, W. Chen, W. Liu, Y. Rong and D. Bi, *Adv. Mater.*, 2025, **37**, 2500501.
35. H. Rao, S. Ye, T. Salim, R. Mayengbam, Y. Guo, M. Feng, L. Xi, Z. Yen, R. Salim, Y. Wang, R. Cai, X. Xiao, B. Wang, H. He, T. C. Sum and Y. M. Lam, *Nat. Energy*, 2025, **10**, 991-1000.
36. Z.-Y. Suo, R. Dong, C. Chen, X. Mu, J. Hao and J. Cao, *Adv. Mater.*, 2026, **38**, e17731.
37. X. Tang, C. Yang, Y. Xu, J. Xia, B. Li, M. Li, Y. Zhou, L. Jiang, H. Liu, K. Ma, Q. Yu, B. Dong, Y. Liu, O. F. Mohammed and X. Zheng, *Nat. Photonics*, 2025, **19**, 701-708.
38. C. Zhang, L. Yang, Y. Wu, K. Wei, D. Liu, J. Hu, W. Wang, S. Pang, B. Xu and J. Zhang, *Joule*, 2025, **9,** 102217.
39. K. Huang, W. Wang, A. D. Bui, W. Ji, F. Kremer, Z. Yang, G. Bartholazzi, Y. Yu, O. L. C. Lem, B. He, Z. Su, V. Ahmad, L. Chang, D.-T. Nguyen, Y. Liu, X. Gao, J. Yang, K. R. Catchpole, H. Shen, K. J. Weber and T. Duong, *Adv. Sci.*, 2025, **12**, e14595.
40. K. Kim, S. Yang, C. Kim, J. Park, S. Jeong, Y. Kim, J. Park, Z. Sun, M. Kang, B. J. Kang, J. Oh, J. S. Yun, S.-J. Shin, C. Yang and H. Min, *Nat. Energy*, 2025, 10, 1427-1438.
41. W. Jia, R. Sun, J. Qiao, G. Shi, Q. Zhao, Z. Gong, S. Zheng, R. Xu, J. Shang, L. Song, K. Wang, W. Huang, R. Chen, Y. Fang, H. Wang and Z.-Q. Rong, *Angew. Chem. Int. Ed.*, 2025, **64**, e202513869.
42. H. Yang, Z. Guo, Z. Xu, W. Cai, S. M. H. Qaid and Z. Zang, *Adv. Mater.*, 2025, **37**, e10967.
43. Y. Chen and H. Zhou, *J. Appl. Phys.*, 2020, **128**, 060903.
44. W.-J. Yin, T. Shi and Y. Yan, *Appl. Phys. Lett.*, 2014, **104**, 063903.

45. X. Zheng, B. Chen, J. Dai, Y. Fang, Y. Bai, Y. Lin, H. Wei, Xiao C. Zeng and J. Huang, *Nat. Energy*, 2017, **2**, 17102.

46. C. Ruan, L. He, L. Zhu, B. Yuan, H. Yang, G. Qin, Y. Chen and Q. Tao, *J. Alloys Compd.*, 2024, **999**, 174990.

47. J. Wang, L. Bi, Q. Fu and A. K. Y. Jen, *Adv. Energy Mater.*, 2024, **14**, 2401414.

48. D. Meggiolaro, S. G. Motti, E. Mosconi, A. J. Barker, J. Ball, C. Andrea Riccardo Perini, F. Deschler, A. Petrozza and F. De Angelis, *Energy Environ. Sci.*, 2018, **11**, 702-713.

49. G.-W. Kim and A. Petrozza, *Adv. Energy Mater.*, 2020, **10**, 2001959.

50. H. Baishya, R. D. Adhikari, M. J. Patel, D. Yadav, T. Sarmah, M. Alam, M. Kalita and P. K. Iyer, *J. Energy Chem.*, 2024, **94**, 217-253.

51. R. Lindblad, D. Bi, B.-w. Park, J. Oscarsson, M. Gorgoi, H. Siegbahn, M. Odelius, E. M. J. Johansson and H. Rensmo, *J. Phys. Chem. Lett.*, 2014, **5**, 648-653.

52. R. Lindblad, N. K. Jena, B. Philippe, J. Oscarsson, D. Bi, A. Lindblad, S. Mandal, B. Pal, D. D. Sarma, O. Karis, H. Siegbahn, E. M. J. Johansson, M. Odelius and H. Rensmo, *J. Phys. Chem. C*, 2015, **119**, 1818-1825.

53. A. L. Abdelhady, S. N. Afraj, Y. Haruta, M. M. Uddin and M. I. Saidaminov, *ACS Nano*, 2025, **19**, 35276-35305.

54. S. Tan, I. Yavuz, M. H. Weber, T. Huang, C.-H. Chen, R. Wang, H.-C. Wang, J. H. Ko, S. Nuryyeva, J. Xue, Y. Zhao, K.-H. Wei, J.-W. Lee and Y. Yang, *Joule*, 2020, **4**, 2426-2442.

55. J.-W. Lee, S.-G. Kim, J.-M. Yang, Y. Yang and N.-G. Park, *APL Mater.*, 2019, **7**, 041111.

56. E. Bi, Z. Song, C. Li, Z. Wu and Y. Yan, 2021, 3, 575-588.

57. S. Jung, Y. Choi, Y. Kim, Y. Jang, H. Jung, H. Jeon, J. Kim, E. Son, S. Jeong, J. M. Baik, J.-Y. Kim, J. Lu and H. Park, *Nano Energy*, 2025, **145**, 111482.

58. D.-J. Xue, Y. Hou, S.-C. Liu, M. Wei, B. Chen, Z. Huang, Z. Li, B. Sun, A. H. Proppe, Y. Dong, M. I. Saidaminov, S. O. Kelley, J.-S. Hu and E. H. Sargent, *Nat. Commun.*, 2020, **11**, 1514.

59. J. Zhao, Y. Deng, H. Wei, X. Zheng, Z. Yu, Y. Shao, J. E. Shield and J. Huang, *Sci. Adv.*, 2017, **3**, eaao5616.

60. Z. Song, A. Abate, S. C. Watthage, G. K. Liyanage, A. B. Phillips, U. Steiner, M. Graetzel and M. J. Heben, *Adv. Energy Mater.*, 2016, **6**, 1600846.

61. D. Menzel, A. Al-Ashouri, A. Tejada, I. Levine, J. A. Guerra, B. Rech, S. Albrecht and L. Korte, *Adv. Energy Mater.*, 2022, **12**, 2201109.

View Article Online
DOI: 10.1039/D5SC10164F

62. F. Zu, P. Amsalem, M. Ralaiarisoa, T. Schultz, R. Schlesinger and N. Koch, *ACS Appl. Mater. Interfaces*, 2017, **9**, 41546-41552.
63. F. Ye, S. Zhang, F. Lang, M. Raoufi, J. Liang, I. Levine, H. Hempel, D. Menzel, F. Zu, S. Albrecht, L. Korte, C. Messmer, J. Schön, S. W. Glunz, T. Unold, N. Koch, D. Neher, D. Ye, Y. Wu and M. Stolterfoht, *ACS Energy Lett.*, 2025, **10**, 2942-2951.
64. F. Ye, S. Zhang, J. Warby, J. Wu, E. Gutierrez-Partida, F. Lang, S. Shah, E. Saglamkaya, B. Sun, F. Zu, S. Shoaee, H. Wang, B. Stiller, D. Neher, W.-H. Zhu, M. Stolterfoht and Y. Wu, *Nat. Commun.*, 2022, **13**, 7454.
65. Z. Ni, H. Jiao, C. Fei, H. Gu, S. Xu, Z. Yu, G. Yang, Y. Deng, Q. Jiang, Y. Liu, Y. Yan and J. Huang, *Nat. Energy*, 2022, **7**, 65-73.
66. N. Ahn, K. Kwak, M. S. Jang, H. Yoon, B. Y. Lee, J.-K. Lee, P. V. Pikhitsa, J. Byun and M. Choi, *Nat. Commun.*, 2016, **7**, 13422.
67. P. P. Khlyabich, B. Burkhart, A. E. Rudenko and B. C. Thompson, *Polymer*, 2013, **54**, 5267-5298.
68. Y. Yang, W. Chen, L. Dou, W.-H. Chang, H.-S. Duan, B. Bob, G. Li and Y. Yang, *Nat. Photonics*, 2015, **9**, 190-198.
69. W. Liu, G. Huang, C.-Y. Chen, T. Tan, H. Fuyuki, S. Hu, T. Nakamura, M. A. Truong, R. Murdey, Y. Hashikawa, Y. Murata and A. Wakamiya, *Chem. Commun.*, 2024, **60**, 2172-2175.
70. M. N. Thameel, O. M. Dawood, Z. S. Hadawi and A. Y. Ali, *Braz. J. Phys.*, 2024, **54**, 76.
71. S. Engmann, A. J. Barito, E. G. Bittle, N. C. Giebink, L. J. Richter and D. J. Gundlach, *Nat. Commun.*, 2019, **10**, 227.
72. P. Cai, X. Xu, J. Sun, J. Chen and Y. Cao, *RSC Adv.*, 2017, **7**, 20440-20450.
73. W. Xu, L. J. F. Hart, B. Moss, P. Caprioglio, T. J. Macdonald, F. Furlan, J. Panidi, R. D. J. Oliver, R. A. Pacalaj, M. Heeney, N. Gasparini, H. J. Snaith, P. R. F. Barnes and J. R. Durrant, *Adv. Energy Mater.*, 2023, **13**, 2301102.
74. R. Gottesman, P. Lopez-Varo, L. Gouda, Juan A. Jimenez-Tejada, J. Hu, S. Tirosh, A. Zaban and J. Bisquert, *Chem*, 2016, **1**, 776-789.
75. S. Guo, X. Sun, C. Ding, R. Huang, M. Tan, L. Zhang, Q. Luo, F. Li, J. Jin and C.-Q. Ma, *Energy Technol.*, 2020, **8**, 2000250.
76. X. Li, S. Fu, W. Zhang, S. Ke, W. Song and J. Fang, *Sci. Adv.*, 2020, **6**, eabd1580.
77. W. Chen, B. Han, Q. Hu, M. Gu, Y. Zhu, W. Yang, Y. Zhou, D. Luo, F.-Z. Liu, R. Cheng, R. Zhu, S.-P. Feng, A. B. Djurišić, T. P. *Sci. Bull.*, 2021, **66**, 991-1002.

View Article Online
DOI: 10.1039/D5SC10164F

78. Q. Liang, K. Liu, Y. Han, H. Xia, Z. Ren, D. Li, T. Zhu, L. Cheng, Z. Wang, C. Zhu, P. W. K. Fong, J. Huang, Q. Chen, Y. Yang and G. Li, *Nat. Commun.*, 2025, **16**, 190.
79. D. Bi, W. Tress, M. I. Dar, P. Gao, J. Luo, C. Renevier, K. Schenk, A. Abate, F. Giordano, J.-P. Correa Baena, J.-D. Decoppet, S. M. Zakeeruddin, M. K. Nazeeruddin, M. Grätzel and A. Hagfeldt, *Sci. Adv.*, 2016, **2**, e1501170.
80. T. Liu, R. A. Scheidt, X. Zheng, S. Joy, Q. Jiang, H. R. Atapattu, M. Chen, H. Pruett, K. Zhu, J. M. Luther, M. C. Beard and K. R. Graham, *Cell Rep. Phys. Sci.*, 2023, **4**, 101650.
81. A. Zanetta, I. Bulfaro, F. Faini, M. Manzi, G. Pica, M. De Bastiani, S. Bellani, M. I. Zappia, G. Bianca, L. Gabatel, J.-K. Panda, A. E. Del Rio Castillo, M. Prato, S. Lauciello, F. Bonaccorso and G. Grancini, *J. Mater. Chem. A*, 2023, **11**, 12866-12875.
82. H. Chen, C. Liu, J. Xu, A. Maxwell, W. Zhou, Y. Yang, Q. Zhou, A. S. R. Bati, H. Wan, Z. Wang, L. Zeng, J. Wang, P. Serles, Y. Liu, S. Teale, Y. Liu, M. I. Saidaminov, M. Li, N. Rolston, S. Hoogland, T. Filleter, M. G. Kanatzidis, B. Chen, Z. Ning and E. H. Sargent, *Science*, 2024, **384**, 189-193.
83. Fazri, T. A. Rizal, M. Amin and Hamdani, *IOP Conf. Ser. Mater. Sci. Eng.*, 2019, **536**, 012082.
84. T. Ma, Y. An, Z. Yang, Z. Ai, Y. Zhang, C. Wang and X. Li, *Adv. Funct. Mater.*, 2023, **33**, 2212596.
85. M. A. Haque, S. Kee, D. R. Villalva, W.-L. Ong and D. Baran, *Adv. Sci.*, 2020, **7**, 1903389.
86. A. Bhui, T. Ghosh, K. Pal, K. Singh Rana, K. Kundu, A. Soni and K. Biswas, *Chem. Mater.*, 2022, **34**, 3301-3310.
87. T. Haeger, R. Heiderhoff and T. Riedl, *Journal of Materials Chemistry C*, 2020, **8**, 14289-14311.
88. S.-N. Hong, C.-J. Yu, U.-G. Jong, S.-H. Choe and Y.-H. Kye, *RSC Adv.*, 2021, **11**, 34015-34023.
89. S. R. Yeandel, M. Molinari and S. C. Parker, *Nanoscale*, 2018, **10**, 15010-15022.
90. H.-S. Kim, S. D. Kang, Y. Tang, R. Hanus and G. Jeffrey Snyder, *Mater. Horiz.*, 2016, **3**, 234-240.
91. A. F. Akbulatov, V. M. Martynenko, L. A. Frolova, N. N. Dremova, I. Zhidkov, S. A. Tsarev, S. Y. Luchkin, E. Z. Kurmaev, S. M. Aldoshin, K. J. Stevenson and P. A. Troshin, *Sol. Energy Mater. Sol. Cells*, 2020, **213**, 110559.
92. L. Ma, D. Guo, M. Li, C. Wang, Z. Zhou, X. Zhao, F. Zhang, Z. Ao and Z. Nie, *Chem. Mater.*, 2019, **31**, 8515-8522.
93. S. Kundu and T. L. Kelly, *EcoMat*, 2020, **2**, e12025.

View Article Online
DOI: 10.1039/D5SC10164F

94. B. Brunetti, C. Cavallo, A. Ciccioli, G. Gigli and A. Latini, *Sci. Rep.*, 2016, **6**, 31896.
95. P.-K. Kung, M.-H. Li, C.-F. Lin and P. Chen, *J. Mater. Chem. C*, 2024, **12**, 11181-11191.
96. D. Zhang, D. Li, Y. Hu, A. Mei and H. Han, *Commun. Mater.*, 2022, **3**, 58.
97. K.-K. Liu, Z.-F. Yao, D. Wang, X. Huang, Q. Li, Z. Su, Z. Zeng, F. R. Lin, C. Zhao, W. Jiang, M. Liu, D. Lei, S.-W. Tsang and A. K. Y. Jen, *Joule*, 2025, **9**, 101955.
98. K. Schutt, M. Davis, M. Li, S. A. Johnson, D. Martinez, J. Titus, T. Leijtens, B. Martin, M. D. McGehee, S. R. Marder, N. Rolston and J. M. Luther, *ACS Energy Lett.*, 2025, **10**, 6307-6317.
99. M. De Bastiani, G. Armaroli, R. Jalmood, L. Ferlauto, X. Li, R. Tao, G. T. Harrison, M. K. Eswaran, R. Azmi, M. Babics, A. S. Subbiah, E. Aydin, T. G. Allen, C. Combe, T. Cramer, D. Baran, U. Schwingenschlögl, G. Lubineau, D. Cavalcoli and S. De Wolf, *ACS Energy Lett.*, 2022, **7**, 827-833.
100. H. Chen, X. Liu, X. Liu, X. Song and W. Zhu, *J. Phys. Chem. Lett.*, 2025, **16**, 10080-10086.
101. P. Chen, X. Ma, Z. Wang, N. Yang, J. Luo, K. Chen, P. Liu, W. Xie and Q. Hu, *Phys. Chem. Chem. Phys.*, 2024, **26**, 14874-14882.
102. M. Waqas, D. B. Khadka, A. H. H. Khan and Y.-C. Wang, *Nanoscale*, 2025, **17**, 15648-15675.
103. V. S. Katta, M. Waheed and J. H. Kim, *Solar RRL*, 2024, **8**, 2300908.
104. Y.-C. Wang, X. Li, L. Zhu, X. Liu, W. Zhang and J. Fang, *Adv. Energy Mater.*, 2017, **7**, 1701144.
105. V. V. Ozerova, A. V. Mumyatov, A. E. Goryachev, E. A. Khakina, A. S. Peregudov, S. M. Aldoshin and P. A. Troshin, *Inorganics*, 2023, **11**, 153.
106. L. N. Inasaridze, A. I. Shames, I. V. Martynov, B. Li, A. V. Mumyatov, D. K. Susarova, E. A. Katz and P. A. Troshin, *J. Mater. Chem. A*, 2017, **5**, 8044-8050.
107. E. M. Speller, A. J. Clarke, N. Aristidou, M. F. Wyatt, L. Francàs, G. Fish, H. Cha, H. K. H. Lee, J. Luke, A. Wadsworth, A. D. Evans, I. McCulloch, J.-S. Kim, S. A. Haque, J. R. Durrant, S. D. Dimitrov, W. C. Tsoi and Z. Li, *ACS Energy Lett.*, 2019, **4**, 846-852.
108. U. Dettinger, H.-J. Egelhaaf, C. J. Brabec, F. Latteyer, H. Peisert and T. Chassé, *Chem. Mater.*, 2015, **27**, 2299-2308.
109. Y. Zhai, Y. Chang, A. Tang and K. Lu, *J. Mater. Chem. A*, 2025, **13**, 9589-9618.
110. H. K. H. Lee, A. M. Telford, J. A. Röhr, M. F. Wyatt, B. Rice, J. Wu, A. de Castro Maciel, S. M. Tuladhar, E. Speller, J. McGettrick, J. R. Searle, S. Pont, T. Watson, T. Kirchartz, J. R. Durrant, W. C. Tsoi, J. Nelson and Z. Li, *Energy Environ. Sci.*, 2018, **11**, 417-428.

111. X. Hou, A. J. Clarke, M. Azzouzi, J. Yan, F. Eisner, X. Shi, M. F. Wyatt, T. J. S. Dennis, Z. Li and J. Nelson, *J. Mater. Chem. C*, 2022, **10**, 7875-7885.

112. S. Wang, A. Wang, X. Deng, L. Xie, A. Xiao, C. Li, Y. Xiang, T. Li, L. Ding and F. Hao, *J. Mater. Chem. A*, 2020, **8**, 12201-12225.

113. Z. Yang, J. Dou, S. Kou, J. Dang, Y. Ji, G. Yang, W.-Q. Wu, D.-B. Kuang and M. Wang, *Adv. Funct. Mater.*, 2020, **30**, 1910710.

114. C. Li, X. Wang, E. Bi, F. Jiang, S. M. Park, Y. Li, L. Chen, Z. Wang, L. Zeng, H. Chen, Y. Liu, C. R. Grice, A. Abudulimu, J. Chung, Y. Xian, T. Zhu, H. Lai, B. Chen, R. J. Ellingson, F. Fu, D. S. Ginger, Z. Song, E. H. Sargent and Y. Yan, *Science*, 2023, **379**, 690-694.

115. F. Zou, C. Duan, Z. Lin, Z. Zhang, S. Xu, C. Chen, J. Chen, J. Li, S. Zou, L. Ding, H. Luo and K. Yan, *Chem. Eng. J.*, 2024, **491**, 152118.

116. Y. Ma, J. Gong, P. Zeng and M. Liu, *Nano-Micro Lett.*, 2023, **15**, 173.

117. G. Huang, C. Wang, H. Zhang, S. Xu, Q. Xu and Y. Cui, *J. Mater. Chem. A*, 2018, **6**, 2449-2455.

118. H. Mo, D. Li, A. Sergeev, W. K. Yiu, J. Wang, G. Zhang, Z. Yuan, Y. Li, Y. He, T. Zhu, M. Yu Lam, F. J. Angus, W.-D. Li, J. Tang, K. S. Wong, G. Cooke, P. Docampo, J. Popović, G. Li and A. B. Djurišić, *Adv. Funct. Mater.*, 2026, **36**, e17140.

119. C. Wang, X. Yu, L. Fan, W. Ge, B. Fan, Q. Huang, R. Peng and B. Jin, *Carbon*, 2023, **215**, 118398.

120. A. Maxwell, H. Chen, L. Grater, C. Li, S. Teale, J. Wang, L. Zeng, Z. Wang, S. M. Park, M. Vafaie, S. Sidhik, I. W. Metcalf, Y. Liu, A. D. Mohite, B. Chen and E. H. Sargent, *ACS Energy Letters*, 2024, **9**, 520-527.

121. Z. Li, B. Li, X. Wu, S. A. Sheppard, S. Zhang, D. Gao, N. J. Long and Z. Zhu, *Science*, 2022, **376**, 416-420.

122. X. Li, W. Zhang, X. Guo, C. Lu, J. Wei and J. Fang, *Science*, 2022, **375**, 434-437.

123. X. Deng, F. Li, Q. Wang, D. Liu, F. Lin, D. Shen, D. Lei, Y.-K. Peng, Z. Zhu and A. K. Y. Jen, *Matter*, 2021, **4**, 3301-3312.

124. J. Liu, M. De Bastiani, E. Aydin, G. T. Harrison, Y. Gao, R. R. Pradhan, M. K. Eswaran, M. Mandal, W. Yan, A. Seitkhan, M. Babics, A. S. Subbiah, E. Ugur, F. Xu, L. Xu, M. Wang, A. u. Rehman, A. Razzaq, J. Kang, R. Azmi, A. A. Said, F. H. Isikgor, T. G. Allen, D. Andrienko, U. Schwingenschlögl, F. Laquai and S. De Wolf, *Science*, 2022, **377**, 302-306.

125. K. Artuk, D. Turkay, M. D. Mensi, J. A. Steele, D. A. Jacobs, M. Othman, X. Yu Chin, S.-J. Moon, A. N. Tiwari, A. Hessler-Wyser, Q. Jeangros, C. Ballif and C. M. Wolff, *Adv. Mater.*, 2024, **36**, 2311745.
126. Y. Ouyang, L. Shi, Q. Li and J. Wang, *Small Methods*, 2019, **3**, 1900154.
127. J. Hidalgo, W. Kaiser, Y. An, R. Li, Z. Oh, A.-F. Castro-Méndez, D. K. LaFollette, S. Kim, B. Lai, J. Breternitz, S. Schorr, C. A. R. Perini, E. Mosconi, F. De Angelis and J.-P. Correa-Baena, *J. Am. Chem. Soc.*, 2023, **145**, 24549-24557.
128. U.-G. Jong, C.-J. Yu, G.-C. Ri, A. P. McMahon, Nicholas M. Harrison, P. R. F. Barnes and A. Walsh, *J. Mater. Chem. A*, 2018, **6**, 1067-1074.
129. Y. Zhang, J. Xi, Y. Deng, W. Liu, Z. Li, C. Liu and W. Guo, *Adv. Energy Mater.*, 2024, **14**, 2403326.
130. P. Liu, X. Li, T. Cai, W. Xing, N. Yang, H. Arandiyan, Z. Shao, S. Wang and S. Liu, *Nano-Micro Lett.*, 2024, **17**, 35.
131. U. Gunes, F. V. Yaylali, Z. Gozukara Karabag, X.-X. Gao, O. A. Syzgantseva, A. Karabag, G. B. Yildirim, K. Tsoi, N. Shibayama, H. Kanda, A. I. Rafieh, L. Zhong, A. Züttel, P. J. Dyson, S. Yerci, M. K. Nazeeruddin and G. Gunbas, *Cell Rep. Phys. Sci.*, 2023, **4**, 101380.
132. H. Lin, C. Zhou, Y. Tian, T. Siegrist and B. Ma, *ACS Energy Lett.*, 2018, **3**, 54-62.
133. Y. Chen, X. Wang, Y. Wang, X. Liu, Y. Miao and Y. Zhao, *Sci. Bull.*, 2023, **68**, 706-712.
134. Y. Han, S. Yue and B.-B. Cui, *Adv. Sci.*, 2021, **8**, 2004805.
135. S. Sun, M. Lu, X. Gao, Z. Shi, X. Bai, W. W. Yu and Y. Zhang, *Adv. Sci.*, 2021, **8**, 2102689.
136. L. N. Quan, M. Yuan, R. Comin, O. Voznyy, E. M. Beauregard, S. Hoogland, A. Buin, A. R. Kirmani, K. Zhao, A. Amassian, D. H. Kim and E. H. Sargent, *J. Am. Chem. Soc.*, 2016, **138**, 2649-2655.
137. B. Li, J. Deng, J. A. Smith, P. Caprioglio, K. Ji, D. Luo, J. D. McGettrick, K. D. G. I. Jayawardena, R. C. Kilbride, A. Ren, S. Hinder, J. Bi, T. Webb, I. Marko, X. Liu, Y. Xiang, J. Reding, H. Li, S. Du, D. G. Lidzey, S. D. Stranks, T. Watson, S. Sweeney, H. J. Snaith, S. R. P. Silva and W. Zhang, *Adv. Energy Mater.*, 2022, **12**, 2202868.
138. Q. Li, H. Liu and T. Zhou, *Sci. China Chem.*, 2024, **67**, 3083-3090.
139. X. Zang, S. Xiong, S. Jiang, D. Li, H. Wu, H. Ren, A. Cao, B. Li, Z. Ma, J. Chen, L. Ding, J. Tang, Z. Sun, J. Chu and Q. Bao, *Adv. Mater.*, 2024, **36**, 2309991.
140. Y. Zhang, C. Li, E. Bi, T. Wang, P. Zhang, X. Yang and H. Chen, *Adv. Energy Mater.*, 2022, **12**, 2202191.
141. Z. Li, A. Sun, Y. Zheng, R. Zhuang, X. Wu, C. Tian, C. Tang, Y. Liu, B. Ouyang, J. Du, Z. Li, J. Cai, X. Wu, J. Chen, Y. Hua and C.-C. Chen, *Small Methods*, 2024, **8**, 2400425.

142. Y. Zhao, Y.-C. Ye, X.-M. Chen, J.-G. Wang, L.-J. Zhang, H.-W. Du, C. Zhang, J. Yang, X.-Y. Zhang, M.-L. Xu, Q.-F. Ye, X. Gao, H. Xie, J.-X. Tang and W.-D. Dou, *ACS Sustain. Chem. Eng.*, 2025, **13**, 13148-13156.
143. T. Wang, L. Bi, L. Yang, Z. Zeng, X. Ji, Z. Hu, S.-W. Tsang, H.-L. Yip, Q. Fu, A. K. Y. Jen and Y. Liu, *J. Am. Chem. Soc.*, 2024, **146**, 7555-7564.
144. X. Liu, Q. Li, Y. Zheng, D. Liu, H. Wang, D. Li, M. Song, R. Yang, J. Lin, Y. Shi, P. Wang, Y. Wu, H. G. Yang, S. Yang and Y. Hou, *Adv. Funct. Mater.*, 2026, **36**, e17301.
145. Z. Wan, R. Wei, Y. Wang, H. Zeng, H. Yin, M. Azam, J. Luo and C. Jia, *Nano-Micro Lett.*, 2025, **18**, 18.
146. K. Choi, J. Lee, H. Choi, G.-W. Kim, H. I. Kim and T. Park, *Energy Environ. Sci.*, 2020, **13**, 5059-5067.
147. S. Park, S. Y. Jeong, J. Kim, H. Lee, H. S. Kim, Y. W. Noh, Y. I. Kim, S. Cho, J. S. Kang, H. Y. Woo and M. H. Song, *Energy Environ. Sci.*, 2024, **17**, 8304-8312.
148. B. Yu, J. Shi, Y. Li, S. Tan, Y. Cui, F. Meng, H. Wu, Y. Luo, D. Li and Q. Meng, *Nat. Commun.*, 2025, **16**, 3328.
149. X. Sun, C. Zhang, D. Gao, X. Yu, B. Li, X. Wu, S. Zhang, Y. He, Z. Yu, L. Qian, J. Gong, S. Li, N. Li, Z. Zhu and Z. a. Li, *Angew. Chem. Int. Ed.*, 2025, **64**, e202412819.
150. Q.-J. Shui, S. Shan, Y.-C. Zhai, S. Aoyagi, S. Izawa, M. Huda, C.-Y. Yu, L. Zuo, H. Chen, H.-S. Lin and Y. Matsuo, *J. Am. Chem. Soc.*, 2023, **145**, 27307-27315.
151. S. You, H. Zhu, Z. Shen, X. Wang, B. Shao, Q. Wang, J. Lu, Y. Yuan, B. D. Dou, E. M. Sanehira, T. Russell, A. Lorenz, Y. Dong, L. Chen, M. Casareto, N. Rolston, M. C. Beard, J. J. Berry, M. Freitag, Y. Yan, O. M. Bakr and K. Zhu, *Science*, 2025, **388**, 964-968.
152. F. Liu, B.-W. Chen, A. Fan, Z.-C. Chen, Y. Pan, Z. Tang, L.-L. Deng, Z. Xing and S.-H. Li, *Adv. Funct. Mater.*, 2025, **35**, 2419582.
153. Y. Shao, Y. Yuan and J. Huang, *Nat. Energy*, 2016, **1**, 15001.
154. J. Lian, B. Lu, F. Niu, P. Zeng and X. Zhan, *Small Methods*, 2018, **2**, 1800082.
155. X. Huang, D. Xia, Q. Xie, D. Wang, Q. Li, C. Zhao, J. Yin, F. Cao, Z. Su, Z. Zeng, W. Jiang, W. Kaminsky, K. Liu, F. R. Lin, Q. Feng, B. Wu, S.-W. Tsang, D. Lei, W. Li and A. K. Y. Jen, *Nat. Commun.*, 2025, **16**, 1626.
156. Z. Xing, S.-H. Li and S. Yang, *Small Struct.*, 2022, **3**, 2200012.
157. C.-H. Lin, L. Hu, X. Guan, J. Kim, C.-Y. Huang, J.-K. Huang, S. Singh and T. Wu, *Adv. Mater.*, 2022, **34**, 2108616.
158. Y. Li, X. He, R. Zhu, X. Chen, T. Wang, X. Pu, H. Chen, Q. Cao and X. Li, *Adv. Funct. Mater.*, 2025, **35**, 2413245.

159. S. A. L. Weber, I. M. Hermes, S.-H. Turren-Cruz, C. Gort, V. W. Bergmann, L. Gilson, A. Hagfeldt, M. Graetzel, W. Tress and R. Berger, *Energy Environ. Sci.*, 2018, **11**, 2404-2413.

160. H. Ishii, K. Sugiyama, E. Ito and K. Seki, *Adv. Mater.*, 1999, **11**, 605-625.

161. Q. Chen, C. Wang, Y. Li and L. Chen, *J. Am. Chem. Soc.*, 2020, **142**, 18281-18292.

162. J. Seo, S. Park, Y. Chan Kim, N. J. Jeon, J. H. Noh, S. C. Yoon and S. I. Seok, *Energy Environ. Sci.*, 2014, **7**, 2642-2646.

163. S.-G. Choi, S.-K. Jung, J.-H. Lee, J.-H. Kim, W. Zheng and J.-W. Lee, *ACS Energy Lett.*, 2024, **9**, 5360-5363.

164. C. Chen, S. Zhang, S. Wu, W. Zhang, H. Zhu, Z. Xiong, Y. Zhang and W. Chen, *RSC Adv.*, 2017, **7**, 35819-35826.

165. J. Ciro, S. Mesa, J. I. Uribe, M. A. Mejía-Escobar, D. Ramirez, J. F. Montoya, R. Betancur, H.-S. Yoo, N.-G. Park and F. Jaramillo, *Nanoscale*, 2017, **9**, 9440-9446.

166. J.-H. Lee, J. Kim, G. Kim, D. Shin, S. Y. Jeong, J. Lee, S. Hong, J. W. Choi, C.-L. Lee, H. Kim, Y. Yi and K. Lee, *Energy Environ. Sci.*, 2018, **11**, 1742-1751.

167. D. Wang, C. Kang, T. Ye, D. He, S. Jin, X. Zhang, X. Sun and Y. Zhang, *J. Energy Chem.*, 2023, **82**, 334-342.

168. Y. W. Noh, J. M. Ha, J. G. Son, J. Han, H. Lee, D. W. Kim, M. H. Jee, W. G. Shin, S. Cho, J. Y. Kim, M. H. Song and H. Y. Woo, *Mater. Horiz.*, 2024, **11**, 2926-2936.

169. H. S. Kim, Y. Cho, H. Lee, S. Kim, E. D. Jung, Y. W. Noh, S. Park, S. Cho, B. R. Lee, C. Yang and M. H. Song, *Nano Energy*, 2024, **125**, 109584.

170. T. Wu, P. Xu, D. Wang, X. Jiang, F. Guo, S. Gao, Z. Ge and Y. Zhang, *Chem. Eng. J.*, 2023, **454**, 140451.

171. L. Gao, H. Wang, Q. Guo, Z. Wang, F. Yuan and E. Zhou, *Chem. Eng. J.*, 2024, **480**, 148277.

172. J. Wang, J. Li, Y. Zhou, C. Yu, Y. Hua, Y. Yu, R. Li, X. Lin, R. Chen, H. Wu, H. Xia and H.-L. Wang, *J. Am. Chem. Soc.*, 2021, **143**, 7759-7768.

173. T. Imran, H. S. Aziz, T. Iftikhar, M. Ahmad, H. Xie, Z. Su, P. Yan, Z. Liu, G. Liang, W. Chen and S. Chen, *Energy Environ. Sci.*, 2024, **17**, 7234-7246.

174. Y. Kato, L. K. Ono, M. V. Lee, S. Wang, S. R. Raga and Y. Qi, *Adv. Mater. Interfaces*, 2015, **2**, 1500195.

175. J. Li, Q. Dong, N. Li and L. Wang, *Adv. Energy Mater.*, 2017, **7**, 1602922.

176. C. C. Boyd, R. Cheacharoen, T. Leijtens and M. D. McGehee, *Chem. Rev.*, 2019, **119**, 3418-3451.

177. S. Svanström, T. J. Jacobsson, G. Boschloo, E. M. J. Johansson, H. Rensmo and U. B. Cappel, *ACS Appl. Mater. Interfaces*, 2020, **12**, 7212-7221.
178. C. Gong, H. Li, H. Wang, C. Zhang, Q. Zhuang, A. Wang, Z. Xu, W. Cai, R. Li, X. Li and Z. Zang, *Nat. Commun.*, 2024, **15**, 4922.
179. F. Cheng, S. Zhan, Y. Cai, F. Cao, X. Dai, R. Xu, J. Yin, J. Li, N. Zheng and B. Wu, *J. Am. Chem. Soc.*, 2023, **145**, 20081-20087.
180. S. Cao, J. Han, X. Zhao, Y. Yu and P. Gao, *Adv. Energ. Sust. Res.*, 2025, **000**, e202500380.
181. M. Kim, H. Jun, H. Lee, H. Nahdi, D. Tondelier, Y. Bonnassieux, J.-É. Bourée and B. Geffroy, *Eur. J. Inorg. Chem.*, 2021, **2021**, 4781-4789.
182. J. Ning, Y. Zhu, Z. Hu, Y. Shi, M. U. Ali, J. He, Y. He, F. Yan, S. Yang, J. Miao and H. Meng, *Adv. Funct. Mater.*, 2020, **30**, 2000837.
183. B. Orwat, Z.-E. Shi, C.-H. Ma, K. Jankowska, J. Nawrocik, A. Singh, Y.-H. Zheng, W.-C. Tu, Z. Ling, P. Dąbczyński, M. Rogala, P. Krukowski, P. J. Kowalczyk, P. Data, B. Łuszczyńska, I. Kownacki and C.-P. Chen, *Small*, 2025, **21**, 2411623.
184. C. Wang, P. Liu, H. Ju, Q. Yuan, D. Han, Y. Wang, D.-Y. Zhou and L. Feng, *ACS Appl. Mater. Interfaces*, 2018, **10**, 15933-15942.
185. J. Yang, Q. Cao, T. Wang, B. Yang, X. Pu, Y. Zhang, H. Chen, I. Tojiboyev, Y. Li, L. Etgar, X. Li and A. Hagfeldt, *Energy Environ. Sci.*, 2022, **15**, 2154-2163.
186. A. Liu, X. Li, W. Zhang, H. Yang, X. Guo, C. Lu, H. Yuan, W. Ou-Yang and J. Fang, *Adv. Funct. Mater.*, 2024, **34**, 2307310.
187. B. Yu, K. Wang, Y. Sun and H. Yu, *J. Mater. Chem. A*, 2024, **12**, 27577-27587.
188. H. Back, G. Kim, J. Kim, J. Kong, T. K. Kim, H. Kang, H. Kim, J. Lee, S. Lee and K. Lee, *Energy Environ. Sci.*, 2016, **9**, 1258-1263.
189. A. Zhu, H. Gu, W. Li, J. Guo, S. Li, G. Wang, J. Xia, C. Liang, S. Chen and G. Xing, *Small*, 2025, **21**, e11978.
190. T. Chen, T. Shi, X. Li, J. Zheng, W. Fan, B. Ni, Y. Wang, J. Dai and Z. Xiao, Solar RRL, 2018, 2, 1800167.
191. M. H. Futscher and B. Ehrler, *ACS Energy Lett.*, 2016, **1**, 863-868.
192. J. Lim, N.-G. Park, S. Il Seok and M. Saliba, *Energy Environ. Sci.*, 2024, **17**, 4390-4425.
193. J. Liu, Y. He, L. Ding, H. Zhang, Q. Li, L. Jia, J. Yu, T. W. Lau, M. Li, Y. Qin, X. Gu, F. Zhang, Q. Li, Y. Yang, S. Zhao, X. Wu, J. Liu, T. Liu, Y. Gao, Y. Wang, X. Dong, H. Chen, P. Li, T. Zhou, M. Yang, X. Ru, F. Peng, S. Yin, M. Qu, D. Zhao, Z. Zhao, M. Li, P. Guo, H. Yan, C. Xiao, P. Xiao, J. Yin, X. Zhang, Z. Li, B. He and X. Xu, *Nature*, 2024, **635**, 596-603.

194. X. Luo, H. Luo, H. Li, R. Xia, X. Zheng, Z. Huang, Z. Liu, H. Gao, X. Zhang, S. Li, Z. Feng, Y. Chen and H. Tan, *Adv. Mater.*, 2023, **35**, 2207883.

195. S. Mariotti, E. Köhnen, F. Scheler, K. Sveinbjörnsson, L. Zimmermann, M. Piot, F. Yang, B. Li, J. Warby, A. Musiienko, D. Menzel, F. Lang, S. Keßler, I. Levine, D. Mantione, A. Al-Ashouri, M. S. Härtel, K. Xu, A. Cruz, J. Kurpiers, P. Wagner, H. Köbler, J. Li, A. Magomedov, D. Mecerreyes, E. Unger, A. Abate, M. Stolterfoht, B. Stannowski, R. Schlatmann, L. Korte and S. Albrecht, *Science*, 2023, **381**, 63-69.

196. E. T. Hoke, D. J. Slotcavage, E. R. Dohner, A. R. Bowring, H. I. Karunadasa and M. D. McGehee, *Chem. Sci.*, 2015, **6**, 613-617.

197. T. Huang, S. Tan, S. Nuryyeva, I. Yavuz, F. Babbe, Y. Zhao, M. Abdelsamie, M. H. Weber, R. Wang, K. N. Houk, C. M. Sutter-Fella and Y. Yang, *Sci. Adv.*, 2021, **7**, eabj1799.

198. J. Zheng, D. Ning, Y. Li, Y. Wang, Q. Ma, L. Liu, P. Yang, W. He, H. Yang, W. Duan, H. Zhu, S. Chen, A. Lambertz, K. Ding and Y. Mai, *Cell Rep. Phys. Sci.*, 2024, **5**, 102114.

199. Y. An, N. Zhang, Q. Liu, W. Jiang, G. Du, D. Chen, M. Liu, X. Huang, T. Lei, Q. Qiu, F. R. Lin, X. C. Zeng, A. K. Y. Jen and H.-L. Yip, *Nat. Commun.*, 2025, **16**, 2759.

200. Y. Son, J. Lim, A. K. Le, B.-S. Kim, S. Song and H. Kim, *Mater. Chem. Front.*, 2026, **10**, 21-51.

201. P. Papet, O. Nichiporuk, A. Kaminski, Y. Rozier, J. Kraiem, J. F. Lelievre, A. Chaumartin, A. Fave and M. Lemiti, *Sol. Energy Mater. Sol. Cells*, 2006, **90**, 2319-2328.

202. W. Liang, T. Kho, J. Tong, P. Narangari, S. Armand, M. Ernst, D. Walter, S. Surve, M. Stocks, A. Blakers and K. C. Fong, *Sol. Energy Mater. Sol. Cells*, 2021, **222**, 110909.

203. B. Chen, Z. J. Yu, S. Manzoor, S. Wang, W. Weigand, Z. Yu, G. Yang, Z. Ni, X. Dai, Z. C. Holman and J. Huang, *Joule*, 2020, **4**, 850-864.

204. Y. Hou, E. Aydin, M. De Bastiani, C. Xiao, F. H. Isikgor, D.-J. Xue, B. Chen, H. Chen, B. Bahrami, A. H. Chowdhury, A. Johnston, S.-W. Baek, Z. Huang, M. Wei, Y. Dong, J. Troughton, R. Jalmood, A. J. Mirabelli, T. G. Allen, E. Van Kerschaver, M. I. Saidaminov, D. Baran, Q. Qiao, K. Zhu, S. De Wolf and E. H. Sargent, *Science*, 2020, **367**, 1135-1140.

205. J. Liu, E. Aydin, J. Yin, M. De Bastiani, F. H. Isikgor, A. U. Rehman, E. Yengel, E. Ugur, G. T. Harrison, M. Wang, Y. Gao, J. I. Khan, M. Babics, T. G. Allen, A. S. Subbiah, K. Zhu, X. Zheng, W. Yan, F. Xu, M. F. Salvador, O. M. Bakr, T. D. Anthopoulos, M. Lanza, O. F. Mohammed, F. Laquai and S. De Wolf, *Joule*, 2021, **5**, 3169-3186.

206. Z. Ying, X. Guo, H. Du, X. Li, M. Zhang, Y. Zeng, X. Yang and J. Ye, *ACS Energy Lett.*, 2024, **9**, 4018-4023.

207. N. Liu, G. Zhang, M. Wei, L. Yang, H. Gu, L. Zeng, X. Zhang, Y. Geng, Y. Zhu, C. Shen, Y. Wu, T. Li, W. Wang, X. Li, K. Qiu, P. Wei, G. Yang, J. Huang and B. Chen, *Nat. Commun.*, 2025, **16**, 9435.

208. D. Zhang, T. Wu, B. Li, D. Ding, R. Li, J. Wei, H. Zhang, C. Kan, Y. Yao, P. Hang, Z. Yu, Z. Ni, K. Qiu, D. Yang and X. Yu, *Nat. Commun.*, 2025, **16**, 7331.

209. S. Y. Kim, M. Y. Woo, M. J. Jeong, S. W. Jeon, J. W. Ahn, J. H. Park, C. Y. Kim, D. H. Kim, O. J. Oh, G. Yu, S. Lee, C. Kim, D. H. Kim and J. H. *Adv. Energy Mater.*, 2024, **14**, 2402433.

210. S. Chapagain, P. S. Chandrasekhar, D. McGott, R. C. Bramante, M. F. A. M. van Hest, M. O. Reese, T. Druffel and C. A. Grapperhaus, *ACS Appl. Energy Mater.*, 2021, **4**, 10477-10483.

211. H. Cui, G. Li, S. Zhou, C. Wang, X. Yang, S. Liao, G. Chen, S. Du, F. Ye, K. Dong, S. Wang, G. Li, H.-h. Fu, G. Yang, W. Ke and G. Fang, *Adv. Funct. Mater.*, 2025, e22926.

212. M. R. S. Poma, Y. Zhang, M. Li, K. Mao, R. A. DeCrescent, S. Barlow, N. Rolston, S. R. Marder and M. D. McGehee, *EES Solar*, 2026, DOI: 10.1039/D5EL00194C.

213. A. J. Bett, K. M. Winkler, M. Bivour, L. Cojocaru, Ö. Ş. Kabakli, P. S. C. Schulze, G. Siefer, L. Tutsch, M. Hermle, S. W. Glunz and J. C. Goldschmidt, *ACS Appl. Mater. Interfaces*, 2019, **11**, 45796-45804.

214. A. u. Rehman, E. P. Van Kerschaver, E. Aydin, W. Raja, T. G. Allen and S. De Wolf, *Prog. Photovoltaics Res. Appl.*, 2023, **31**, 429-442.

215. Q. Yang, W. Duan, A. Eberst, B. Klingebiel, Y. Wang, A. Kulkarni, A. Lambertz, K. Bittkau, Y. Zhang, S. Vitusevich, U. Rau, T. Kirchartz and K. Ding, *J. Mater. Chem. A*, 2024, **12**, 14816-14827.

216. M. Härtel, B. Li, S. Mariotti, P. Wagner, F. Ruske, S. Albrecht and B. Szyszka, *Sol. Energy Mater. Sol. Cells*, 2023, **252**, 112180.

217. H. Bristow, X. Li, M. Babics, S. Kosar, A. R. Pininti, S. Zhang, B. Vishal, S. Sarwade, A. Razzaq, A. A. Said, G. Lubineau and S. De Wolf, *Solar RRL*, 2024, **8**, 2400289.

218. K. A. Bush, C. D. Bailie, Y. Chen, A. R. Bowring, W. Wang, W. Ma, T. Leijtens, F. Moghadam and M. D. McGehee, *Adv. Mater.*, 2016, **28**, 3937-3943.

219. E. Magliano, F. Di Giacomo, H. R. Sathy, S. M. Pourmotlagh, G. Giliberti, D. Becerril Rodriguez, G. Ammirati, P. Mariani, F. Zarotti, F. Matteocci, M. Luce, I. Usatii, E. Bobeico, M. Della Noce, A. Cricenti, F. Cappelluti, L. V. Mercaldo, P. Delli Veneri and A. Di Carlo, *ACS Appl. Mater. Interfaces*, 2025, **17**, 17599-17610.

220. H. H. Park, J. Kim, G. Kim, H. Jung, S. Kim, C. S. Moon, S. J. Lee, S. S. Shin, X. Hao, J. S. Yun, M. A. Green, A. W. Y. Ho-Baillie, N. J. Jeon, T.-Y. Yang and J. Seo, *Small Methods*, 2020, **4**, 2000074.
221. D. Song, L. Y. Hsu, C.-M. Tseng and E. W.-G. Diau, *Mater. Adv.*, 2021, **2**, 754-759.
222. F. Yousuf, M.-X. Jiang, C.-F. Lin, M.-H. Li, C.-W. Chu, T.-F. Guo and P. Chen, *EES Solar*, 2025, **1**, 796-809.
223. E. Aydin, C. Altinkaya, Y. Smirnov, M. A. Yaqin, K. P. S. Zanoni, A. Paliwal, Y. Firdaus, T. G. Allen, T. D. Anthopoulos, H. J. Bolink, M. Morales-Masis and S. De Wolf, *Matter*, 2021, **4**, 3549-3584.
224. Y. Yao, S. Li, H. Xu, Z. Gao, J. Ren, Y. Cui, L. Cai, F. Zhu and Y. Hao, *Mater. Today Energy*, 2021, **21**, 100833.
225. C. Weiran, L. Jian, C. Hongzheng and X. Jiangeng, *J. Photonics Energy*, 2014, **4**, 040990.
226. G. Huseynova, J.-H. Lee, Y. H. Kim and J. Lee, *Adv. Opt. Mater.*, 2021, **9**, 2002040.
227. J. Gassmann, J. Brötz and A. Klein, *Appl. Surf. Sci.*, 2012, **258**, 3913-3919.
228. S. H. Reddy, F. Di Giacomo, F. Matteocci, L. A. Castriotta and A. Di Carlo, *ACS Appl. Mater. Interfaces*, 2022, **14**, 51438-51448.
229. K. O. Sylvester-Hvid, *J. Phys. Chem. B*, 2006, **110**, 2618-2627.
230. C. Gu, J. L. Zhang, S. Sun, X. Lian, Z. Ma, H. Mao, L. Guo, Y. Wang and W. Chen, *ACS Appl. Mater. Interfaces*, 2020, **12**, 22327-22334.
231. T. P. I. Saragi, T. Reichert, A. Scheffler, M. Kussler and J. Salbeck, *Synth. Met.*, 2012, **162**, 1572-1576.
232. J.-H. Lee, S. Lee, J.-B. Kim, J. Jang and J.-J. Kim, *J. Mater. Chem.*, 2012, **22**, 15262-15266.
233. B. Yu, F. Tang, Y. Yang, J. Huang, S. Wu, F. Lu, W. Duan, A. Lambertz, K. Ding and Y. Mai, *Adv. Mater.*, 2023, **35**, 2202447.
234. K. O. Brinkmann, T. Gahlmann and T. Riedl, *Solar RRL*, 2020, **4**, 1900332.
235. M. Kedia, C. Das, M. Kot, Y. Yalcinkaya, W. Zuo, K. Tabah Tanko, P. Matvija, M. Ezquer, I. Cornago, W. Hempel, F. Kauffmann, P. Plate, M. Lira-Cantu, S. A. L. Weber and M. Saliba, *Energy Environ. Sci.*, 2025, **18**, 5250-5263.
236. X. Li, Z. Ying, X. Wang, Y. Zeng, X. Yang and J. Ye, *Information Functional Materials*, 2024, **1**, 160-180.

View Article Online
DOI: 10.1039/D5SC10164F

Data availability

No primary research results, software or code have been included and no new data were generated or analysed as part of this review.